

DYNAMICAL AND PHYSICAL CONDITIONS OF STELLAR FORMATION:
A STUDY OF H₂O MASERS ASSOCIATED WITH GALACTIC H_{II} REGIONS

by

A. Colbert Reisz

S.B., Massachusetts Institute of Technology (1970)

S.M., Massachusetts Institute of Technology (1970)

SUBMITTED IN PARTIAL FULFILLMENT OF THE REQUIREMENTS
FOR THE DEGREE OF
DOCTOR OF PHILOSOPHY

at the

MASSACHUSETTS INSTITUTE OF TECHNOLOGY

January 1976

Signature of Author Department of Earth and Planetary Sciences

Certified by _____ Thesis Supervisor

Accepted by _____
Chairman, Departmental Committee on Graduate Students



DYNAMICAL AND PHYSICAL CONDITIONS OF STELLAR FORMATION:
A STUDY OF H₂O MASERS ASSOCIATED WITH GALACTIC H_{II} REGIONS

by

A. Colbert Reisz

Submitted to the Department of Earth and Planetary
Sciences in January 1976, in partial fulfillment of the require-
ments for the degree of Doctor of Philosophy.

Abstract

The importance of initial conditions to considerations of solar system and stellar formation processes is discussed. Astronomical knowledge relating to regions of current stellar formation in our Galaxy is reviewed. The potential of radio observations of astrophysical H₂O masers as a means of probing the regions of current stellar formation at high resolution is discussed. Radio observations of H₂O masers (single antenna and interferometric) are presented. A mathematical model of an H₂O maser is developed and examined numerically. Comparisons between numerical models and the radio observations are made to obtain estimates of linear dimensions, radial and transverse velocities, temperature, and density. Some implications for understanding stellar formation processes are discussed.

Thesis Supervisor: Irwin I. Shapiro
Professor of Geophysics and Physics

Table of Contents

	<u>Page</u>
Abstract	2
Chapter 1: Thesis Introduction	
1.1 Introduction	6
1.2 Thesis Synopsis	7
Chapter 2: Physical Conditions in the Early Solar System	
2.1 The Sun, Planets, and Meteorites	8
2.2 Models of Early Solar System Events	9
Chapter 3: Regions Associated with Current Stellar Formation	
3.1 The Young Stars	15
3.2 H _{II} Regions (Emission Nebulae)	19
Chapter 4: High Resolution Radio Observations of H ₂ O Masers as a Means of Probing Regions of Stellar Formation	
4.1 Introduction	45
4.2 Very Long Baseline Radio Interferometry	46
4.3 Molecular Maser Radio Sources	47
4.4 The H ₂ O 6 ₁₆ → 5 ₂₃ Maser Transition	54
Chapter 5: Radio Observations of H ₂ O Masers	
5.1 VLBI Observations and Analysis	59
5.1.1 Accurate Relative Positions of H ₂ O Emission Features	61
5.1.2 Spectra of Individual H ₂ O Emission Features	67
5.2 Single Antenna Observations Using a Cryogenic Receiver	75
Chapter 6: Modeling an Astrophysical Maser	
6.1 The Equations of Radiative Transfer	92

	<u>Page</u>
6.2 Numerical Examination of the Spectral Emission from Model H ₂ O Masers	100
6.3 Comparisons with Observed Spectra	104
Chapter 7: Interpretations in Terms of Stellar Formation	
7.1 Physical Conditions Associated with H ₂ O Masers	113
7.2 Implications of Physical Conditions for Stellar Formation Processes	121
7.3 Dynamics Associated with Stellar Formation	124
7.4 Future Investigation	127
References	129
Appendix A: Numerical Minimization Technique	134
Appendix B: Computation of the Specific Intensity $I_\nu(z)$	138
Appendix C: Estimation of the H ₂ O Rotational Partition Functions $f_{6_{16}}$ and $f_{5_{23}}$	142
Appendix D: Estimation of the Average H ₂ O-H ₂ Intercollision time, τ	144
Acknowledgements	146
Biographical Note	148

CHAPTER 1

THESIS INTRODUCTION

1.1 Introduction

Chronologically and logically there are two directions that can be followed toward a goal of understanding the formation and evolution of the early solar system. The first approach, and the one to which by far the most effort has been devoted, is to take our knowledge of present ($t \sim 5 \times 10^9$ yr) conditions in our solar system and attempt to extrapolate backwards in time. Reconstructions of previous dynamical, thermal, chemical, radiative, and nuclear processes are, however, complicated and conclusions are often limited. The second approach, and the one this thesis adopts, is to observe regions of present-day stellar, and presumably planetary, formation to attempt to determine actual dynamical and physical conditions associated with initial stages of formation. Of necessity, this approach involves a general study of stellar formation in which the formation of a G2 star like our sun is a special case. This second approach additionally should provide information on the origin of the stellar mass distribution, the formation of multiple star systems, and the regenerative processes involved in galactic spiral arm structure.

Bridging these two chronological approaches are the efforts to model specific events in solar system or stellar formation. These efforts most often involve assumption of a simplified set of physical conditions at a particular time,

and the subsequent following of a sequence of events which can eventually (and sometimes only wistfully) be interfaced with the information base of current knowledge.

1.2 Thesis Synopsis

In the next chapter, we summarize briefly the most certain and relevant (to considerations of stellar formation) results derived by others from studies involving present conditions in the solar system, and then we consider the conclusions drawn from such modeling studies.

In Chapter 3 we review the presently known properties of the regions associated with current stellar production in our Galaxy. Chapter 4 describes the potential of radio observations of astrophysical water-vapor (H_2O) masers to provide a means of probing at high resolution the physical conditions and dynamics in the regions of interest. Radio observations of H_2O masers, both single antenna and interferometric, are presented in Chapter 5. In addition, a statistical method exploiting the inherent accuracy of interferometric observations for determinations of relative positions of radio sources (and thus of their relative velocities) is developed and demonstrated. In Chapter 6 a simplified mathematical model of an astrophysical H_2O maser is described, examined numerically, and compared with the radio spectra presented in Chapter 5.

Discussions of some implications of this study for stellar formation processes, and of future work, are contained in Chapter 7.

CHAPTER 2

PHYSICAL CONDITIONS IN THE EARLY SOLAR SYSTEM

2.1 The Sun, Planets, and Meteorites

After almost two decades of frenetic investigation of our solar system, a rather clear picture of its present condition has developed, along with some hypotheses as to the final stages of planetary accretion. The present solar system contains a G2 star and nearly co-planar planets -- the terrestrial and the gas (and ice) giants. The composition of the gas giants is approximately solar; their density is about fourfold less than that of the terrestrial planets.

Except for the isolated chemical and thermal evolution of the individual planets, and the gradual dynamical evolution of solar system bodies toward resonant spin and orbital states, the solar system has been quiescent for several billion years, and will remain so for an equivalent time. The angular momentum in the present planetary orbits, and the present radial distribution of the elements, are therefore representative of the early, post-accretional solar system. The final stage in the accretion of the terrestrial planets is evidenced in the impact cratering of the remnant primitive surfaces, dated from lunar studies at about 4×10^9 years ago.

A basically unmodified sample of early solar system material has been determined to be the carbonaceous chondrite class of meteorites, whose spectral reflectivities have been associated with certain, apparently undifferentiated, asteroids

[(221)Eos, (176)Iduna] (e.g. Gaffey, 1974; Chapman, 1975).

Other classes of asteroids appear to be differentiated products of the heating of carbonaceous chondritic material*. The carbonaceous chondritic material formed $\sim 4.7 \times 10^9$ years ago at ~ 2.3 A.U.

The current presence of H_2O in chondritic material indicates that since the time of formation it has not experienced sustained temperatures above $\sim 400^\circ K$. As in the case of the Earth, the best known terrestrial planet, the carbonaceous chondrites contain the elements in approximately their solar abundances (see Table 2.1), except for missing volatiles.

We turn next to the modeling studies.

2.2 Models of Early Solar System Events

R. B. Larson has conducted probably the most intensive study of the gravitational collapse of gas clouds leading to the formation of protostars (Larson, 1969a, b; Larson, 1972). The most notable previous effort in this field is that of Gaustad (1963).

In Larson's models, spherically symmetric (and therefore

* To date, the only plausible theory advanced for the selective heating of asteroids involves Ohmic heating under T-Tauri solar wind conditions (Sonett, Colburn, and Schwartz, 1968). A critical examination of this hypothesis awaits coupling of measurements of the electrical and thermal conductivities of carbonaceous chondrites as functions of temperature (e.g., Brecher, Briggs, and Simmons, 1975), models of the solar wind magnetic field-asteroid interaction (e.g., Reisz, Paul, and Madden, 1972), and thermal evolution models (e.g., Toksöz and Solomon, 1973).

Table 2.1

The Solar Abundances of the Major Elements

<u>Element</u>	<u>Abundance* (Si \equiv 10^6)</u>
H(†)	2.8×10^{10}
He	1.8×10^9
O(†)	1.7×10^7
C(†)	1.0×10^7
N	2.4×10^6
Ne	2.1×10^6
Mg	1.1×10^6
Si(†)	1.0×10^6
Fe	8.3×10^5
S	5.0×10^5
Ar	1.2×10^5
Al	8.5×10^4
Ca	7.2×10^4
Na	6.0×10^4
Ni	4.8×10^4
Cr	1.3×10^4
P	9.6×10^3
Mn	9.3×10^3
Cl	5.7×10^3
K	4.2×10^3
Ti	2.8×10^3
F	2.5×10^3

* From Lambert (1967), Suess and Urey (1956), and Aller (1961). Accuracy is seldom better than 10% for the quoted abundances. The elements of primary importance to this investigation are noted with a dagger (†).

also non-rotating and non-magnetic), initially cold gas clouds that satisfy the Jeans criterion evolve through complicated stages of radiation and collapse until, after $\sim 10^6$ years, the "star" resembles a Hayashi pre-main sequence model (Hayashi, 1966). For a one-solar-mass protostar, the dependences of temperature and density on radius that Larson's models suggest are shown in Figure 2.1. Although his models are not applicable to planetary formation, Larson concludes from the rapidity of the stellar formation process that planetary formation must occur simultaneously. This view, popular among some theorists, adds complexity to investigations.

An approach that has proved fruitful in understanding planetary formation has been the examination of the chemical equilibrium condensation sequence in a solar composition gas (Gaustad, 1963; Lord, 1965; Larimer, 1967; Larimer and Anders, 1970; Lewis, 1972). Lewis' models (e.g. Lewis, 1974) show that the planetary densities and semi-major axes plot along an adiabat (or isobar) in a protoplanetary nebula (Figure 2.2). The remaining uncondensed volatile nebula associated with the terrestrial planets would presumably have been dissipated somehow as the sun began hydrogen fusion.

Safronov (1969) and Goldreich and Ward (1973) have attempted to follow the sequence of events beginning with condensation and proceeding toward final planetary accretion. Starting with a rotating gas cloud, these investigators suggest the following sequence of events: During chemical con-

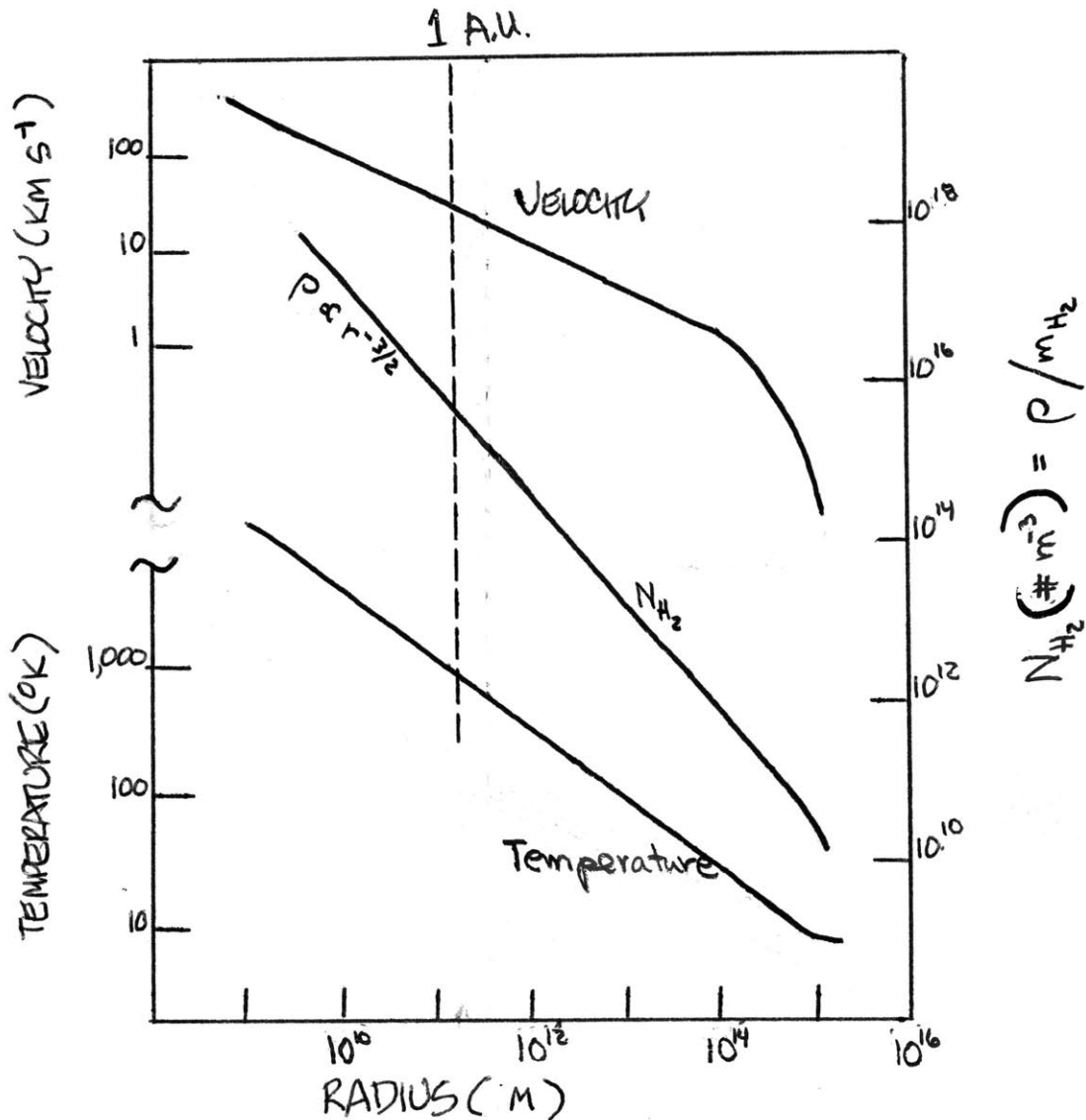
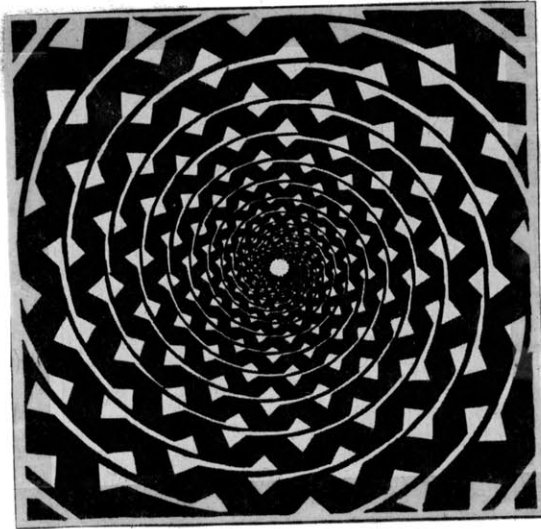


Figure 2.1 Molecular density, temperature, and infall velocity in the envelope of a one-solar-mass protostar, following $\sim 10^5$ years of gravitational collapse starting from an initial temperature of 10°K , radius of $1.6 \times 10^{15} \text{ m} \sim 10^4 \text{ A.U.}$, and density of $1.1 \times 10^{-16} \text{ kg m}^{-3} = m_{H_2} \times 3.3 \times 10^{10} \text{ H}_2 \text{ m}^{-3}$.

Reproduced from Larson (1969a).



The abstract above and the following thesis are dedicated to the ancient Egyptian concept of Nu* $\left(\begin{array}{l} \text{vessels water god} \\ \text{␣␣␣} \\ \text{heaven} \\ \text{␣} \end{array} \right) \left(\begin{array}{l} \text{␣␣␣} \\ \text{␣␣␣} \\ \text{␣␣␣} \end{array} \right) \left(\begin{array}{l} \text{␣} \\ \text{␣} \end{array} \right) .$

A member of the oldest company of the Egyptian gods, Nu was the deity associated with the primeval water, or heavenly Nile (i.e. Milky Way). From the hieroglyphic inscriptions relating the Creation, we learn that the seeds of all life were believed contained in the primordial Nu, whence Ra $\left(\begin{array}{l} \text{sun} \\ \text{⊙} \end{array} \right) \left(\begin{array}{l} \text{god} \\ \text{␣} \end{array} \right)$ and the earth were brought into existence.

*Budge, E. A. W., 1904, The Gods of the Egyptians (1969 Edition, Dover, New York); see also Dreyer, J. L. E., 1906, A History of Astronomy from Thales to Kepler (Dover edition, 1953, New York).

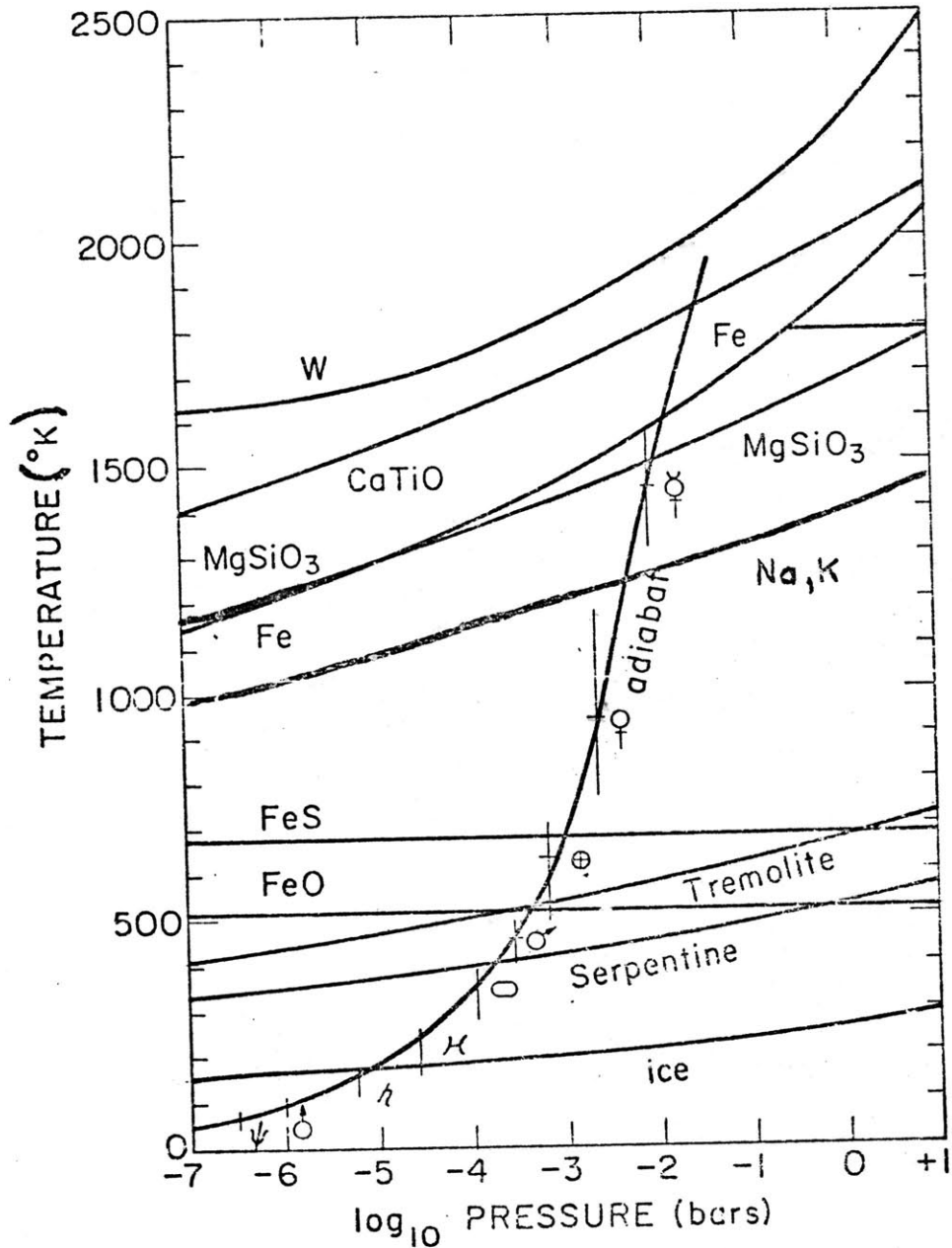


Figure 2.2 Chemical condensation temperature vs. pressure in a solar composition protoplanetary nebula. Planetary formation temperatures (as deduced from present densities) and semimajor axes are plotted along an adiabat in a protoplanetary nebula (Lewis, 1974). Isobaric, rather than adiabatic, P-T profiles yield equivalent results for planetary densities (Lewis, 1974). Reproduced from Barshay and Lewis (1975).

densation, particles with typical linear dimension $\sim 10^{-2}$ m form and settle into a rotating disk, due to gas drag. Goldreich and Ward then theorize a continuation in which gravitational instabilities in the particle disk form $\sim 10^3$ -m-sized planetesimals in two accretional steps. The final step of this scenario (the accretion of planetesimals) remains to be investigated.

It is evident that knowledge of stellar and planetary formation processes would be enhanced if the actual physical and dynamical conditions existing at some early point in the formation process could be determined. Because the formation of the young, metal-enriched Population I stars is presently occurring along the arms of spiral galaxies, it is there that we shall now turn our attention.

CHAPTER 3

REGIONS ASSOCIATED WITH CURRENT STELLAR FORMATION

3.1 The Young Stars

The most readily apparent characteristics of stellar emission are color (surface temperature or spectral class) and brightness (absolute magnitude)*. When the absolute magnitudes and colors are plotted for gravitationally bound clusters of stars in our Galaxy, a Hertzsprung-Russell (H-R) diagram results, as shown in Figure 3.1 (Sandage, 1958).

*The defining relationship for relative stellar magnitudes is

$m_1 - m_2 = -2.5 \log \frac{B_1}{B_2}$, where m designates apparent magnitude and B the observed stellar brightness (received power per unit area). The brightness that would be observed at 10 parsecs defines the absolute magnitude M : $M = m + 5 - 5 \log r$, where $r = [\text{parallax (arc sec)}]^{-1}$ is the stellar distance in parsecs. At the distance of the earth, the sun's observed brightness is $B_{\odot} \sim 1400 \text{ Wm}^{-2}$ (the "solar constant"). Thus the solar luminosity, $L_{\odot} (=4\pi r^2 B_{\odot})$, is $\sim 3.9 \times 10^{26} \text{ W}$. Were the sun at the standard distance of 10 parsecs, it would yield the brightness $\sim 3.5 \times 10^{-10} \text{ Wm}^{-2}$. The stellar magnitude scale is calibrated such that this brightness would be produced by a star of absolute magnitude 4.8.

STELLAR CLASS

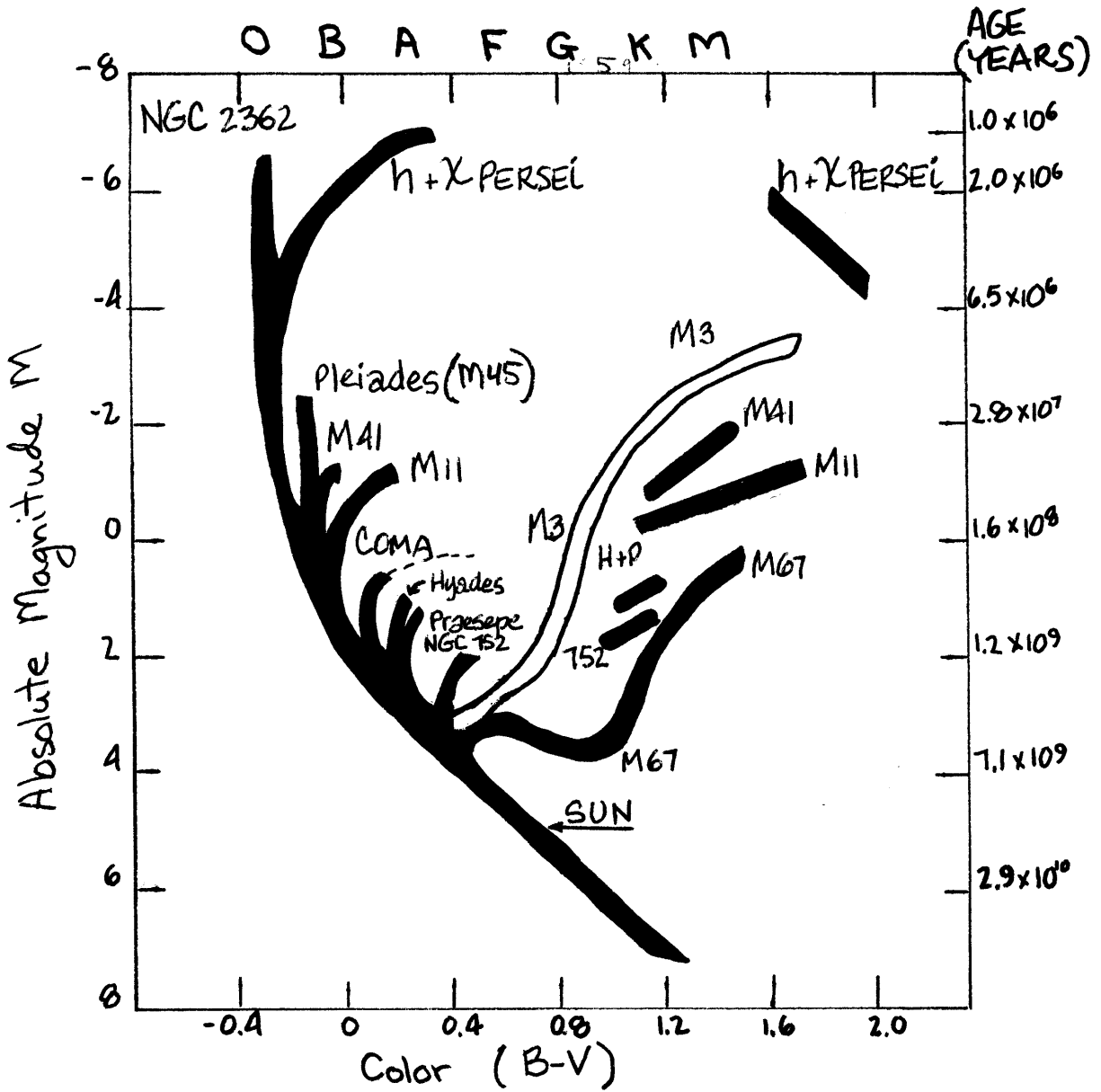


Figure 3.1 Hertzsprung-Russell (color-luminosity) diagrams for various galactic clusters and the globular cluster M 3. After Sandage (1958).

In this figure, it is evident that the differentiating factor among such clusters is the point at which the high mass and luminosity blue stars begin to turn from the main sequence. Estimates of stellar lifetime on the main sequence are based on many factors, including luminosity, energy production in the fusion conversion of hydrogen to helium, and the empirical mass-luminosity relationship*. Such considerations lead to the calibration of Figure 3.1 in years. We note that the globular cluster M3, and the oldest galactic clusters (e.g., M67) would be assigned an age of $\sim 5 \times 10^9$ years. An H-R diagram for an elliptical galaxy would appear similar to that for a globular cluster, thus implying a similar age. A younger galactic cluster, the Pleiades (see Figure 3.2), would have formed about 10^8 years ago, the approximate length of the Galactic rotational period (250×10^6 yrs); the youngest clusters shown in Figure 3.1 have an age of only $\sim 10^6$ years and have been in existence a small fraction of one Galactic rotation period.

* The luminosity of a star on the main sequence is related empirically to its mass by

$$\frac{L_{\star}}{L_{\odot}} = a \left(\frac{M_{\star}}{M_{\odot}} \right)^p$$

where M designates stellar mass and $M_{\odot} \sim 2.0 \times 10^{30}$ kg. Thus

$$\log \left(\frac{L_{\star}}{L_{\odot}} \right) = \log[a] + p \log \left[\frac{M_{\star}}{M_{\odot}} \right].$$

The constants a and p above are determined from observations of main sequence binaries for which the semimajor axes and periods of each can be measured (Kepler's third law then allows M_{\star} to be determined).



Figure 3.2 The Pleiades, a galactic cluster of ~ 300 solar masses, radius ~ 3.5 pc., and age $\sim 10^8$ years. Lick Observatory photograph (Crossley reflector).

Consideration of the dynamical relaxation of clusters (Chandrasekhar, 1942; Wielen, 1971) indicates a relaxation time scale of $\sim 10^7$ years for a cluster such as the Pleiades (~ 300 solar masses, radius ~ 3.5 parsec), and predicts correctly the observed radial velocity dispersion of 0.4 km s^{-1} (Titus, 1938) among its stars. Thus, as we progress to clusters younger than the Pleiades, we expect to encounter stars that have not yet relaxed dynamically, and therefore that have retained some effects of the dynamics of their formation.

As we consider clusters younger than the Pleiades we also begin to reach O-class stars bright enough in the ultraviolet to ionize the gaseous remnants of their formation. The younger a region, the more intense its ultraviolet radiation, and the more intact the remnant nebula.

3.2 H_{II} Regions (Emission Nebulae)

These regions of interstellar ionization (primarily hydrogen) are designated H_{II} regions, as opposed to the neutral hydrogen H_I regions. Also in the class of intragalactic emission nebulae, but of different origin from the H_{II} emission nebulae we are considering here, are the relatively infrequent planetary nebulae (Ring, Bubble, Dumbbell Nebulae) and the supernovae remnants (Veil, Crab Nebulae).

The photographic appearance of galactic spiral arm structure is dominated by the presence of the bright H_{II} regions

(see Figure 3.3). The spiral arms contain the young Population I stars, and the H_I and H_{II} regions; in the nuclei, hydrogen is much depleted and the stars are old Population II (characteristic of globular clusters and elliptical galaxies). Increasingly large and bright H_{II} regions characterize the progression of spiral galaxies from Sa* to Sc. In the progression from Sc to Sa, the arms become increasingly more tightly wound, and the mass of neutral hydrogen decreases (from ~7% of the total mass to ~1% (Roberts, 1974)).

Our view of the Sb Milky Way (Figure 3.4) is similarly dominated by the H_{II} emission nebulae and associated dark H_I clouds along the Sagittarius, Carina-Cygnus (Orion), and Perseus spiral arms. The constellations Cygnus, Lyra, and Cassiopeia are indicated for scale reference purposes in Figure 3.4. The North American Nebula (a typical H_{II} region of low emission measure) is conspicuous in Figure 3.4 near α -Cygni (Deneb). The Andromeda Galaxy (M31), a member of our Local Group, is also visible in Figure 3.4. It has been only since 1924 that the scale of the universe has been sufficiently well established to distinguish the intragalactic distances (kiloparsecs) to Galactic emission nebulae from intergalactic distances (megaparsecs). The famous Curtis-Shapley disagreement (Curtis, 1919; Shapley, 1919) on the "island universe" controversy,

*The classification system for galaxies was developed by Edwin Hubble (1926).

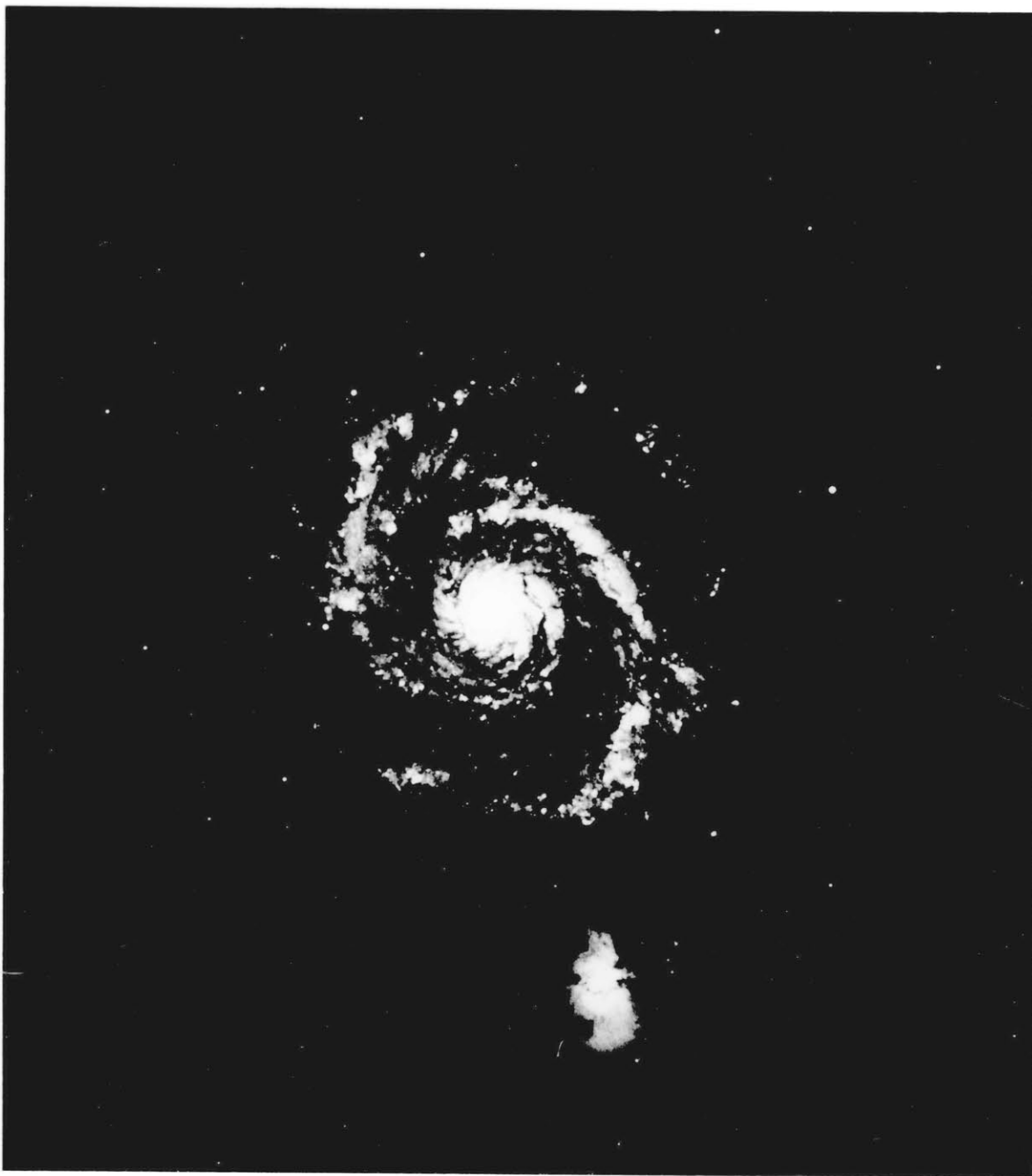


Figure 3.3 The Sc spiral galaxy M51 (NGC 5194) and its satellite NGC 5195. Hale Observatories photograph (200").

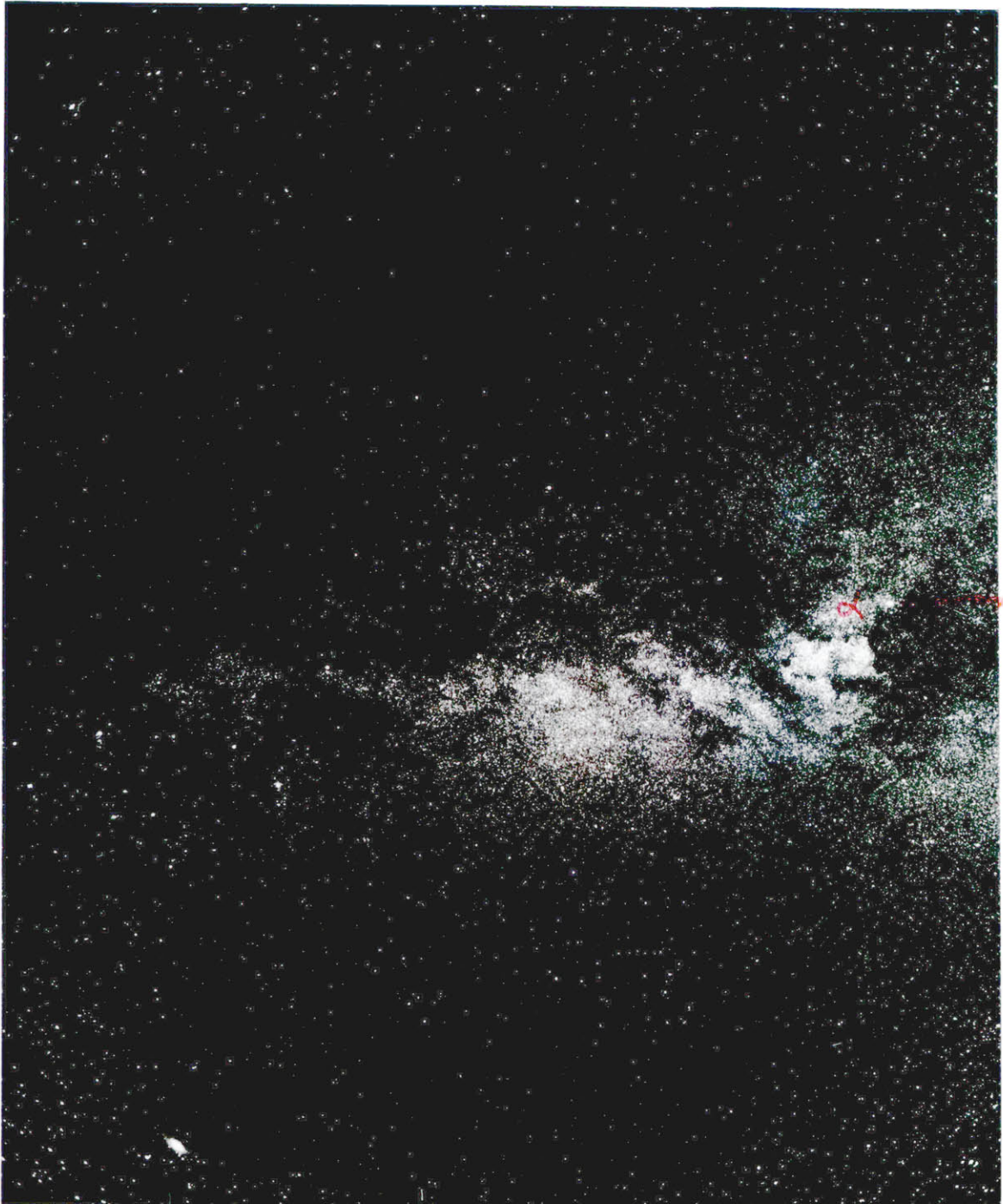


Figure 3.4 The plane of our galaxy, the Sb Milky Way, from Cassiopeia to Cygnus, α -Cygni is Deneb, M 31 is Andromeda. Hale Observatories photograph.

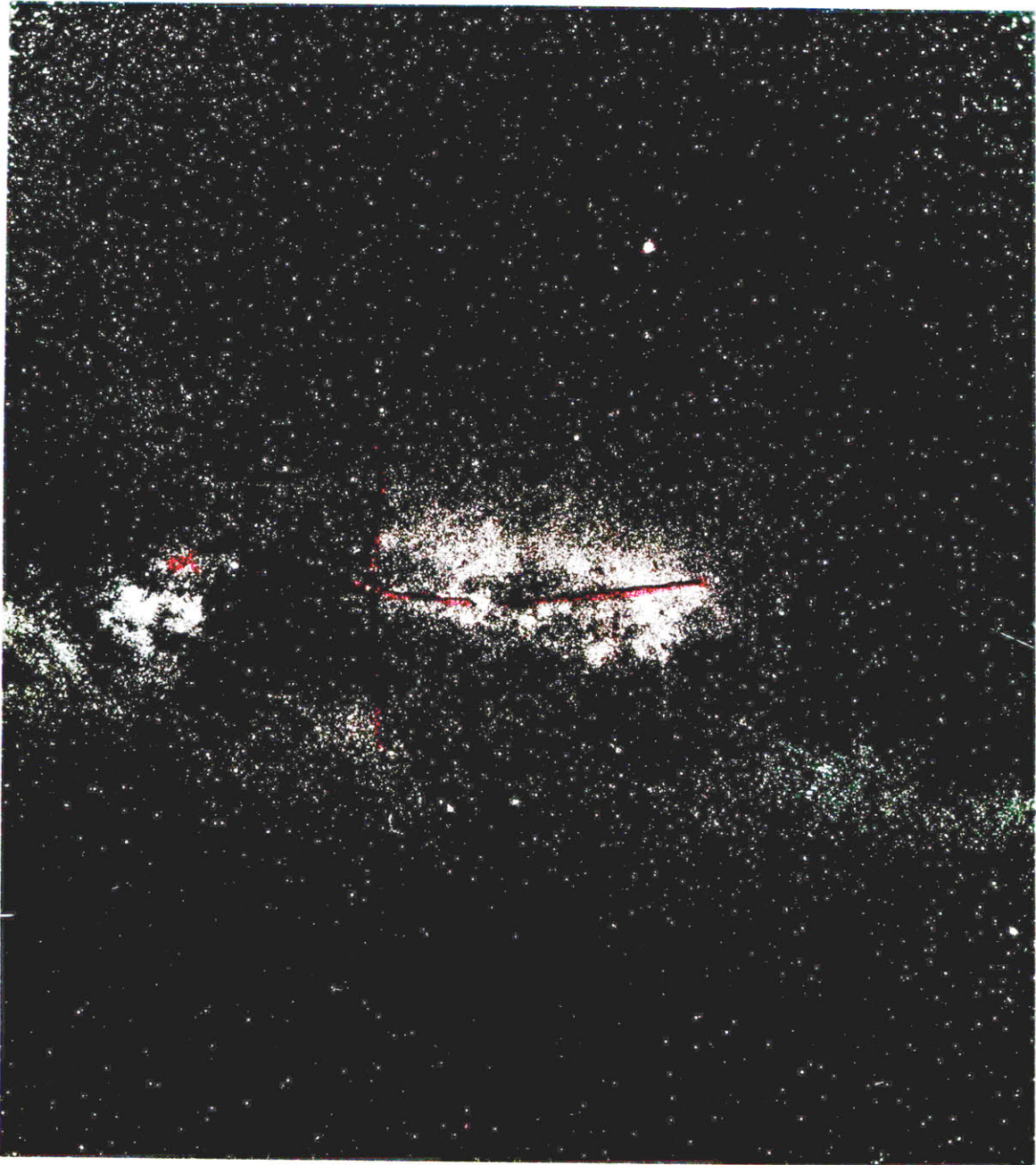


Figure 3.4 The plane of the Galaxy, the Sb Milky Way, from
(cont.) Cassiopeia to Cygnus, α -Cygni is Deneb,
 α -Lyrae is Vega. Hale
Observatories photograph.

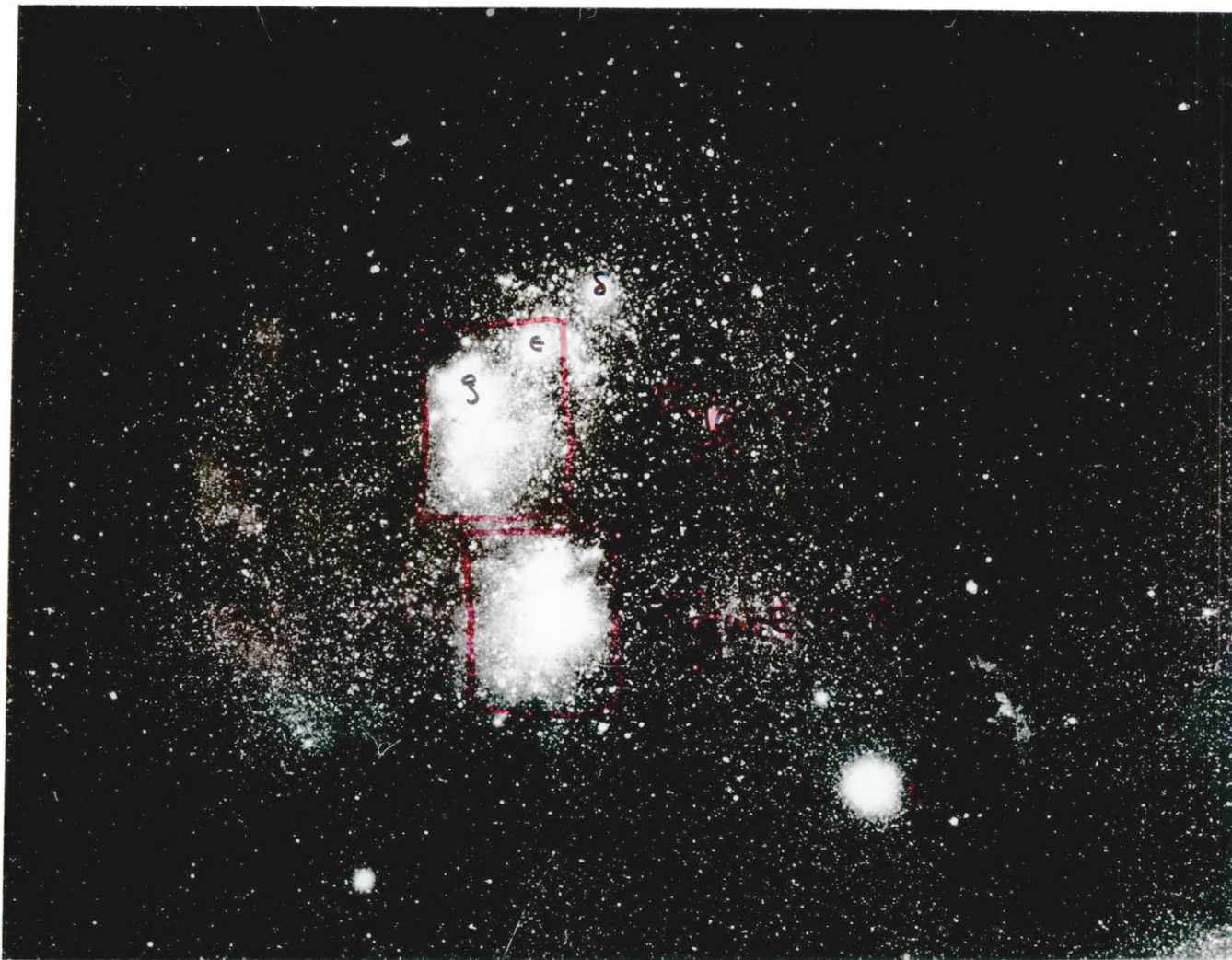
culminating in a debate before the National Academy of Sciences on 26 April 1920, was finally resolved by Hubble's discovery of Cepheid variable stars in M31.

Continuing the progression of scale from Figure 3.4, we show the emission nebulosity associated with the "belt" and "sword" of the constellation Orion in Figure 3.5, where regions displayed in subsequent figures are indicated. The star β -Orionis is Rigel, a (young) B7 star of ~ 30 solar masses and absolute magnitude $M = -7$. In Figure 3.5, and in the subsequent Figures 3.6 and 3.7, the direct juxtaposition of low density H_{II} regions with dense H_I clouds is evident. The well known Horsehead Nebula (an obscuring H_I region) is visible in Figures 3.6 and 3.7. The stars indicated in these figures correspond to those on the star chart, Figure 3.6b, prepared from the Smithsonian Astrophysical Observatory (SAO) Star Catalogue (1966). On the chart, a star's apparent brightness is proportional to the size of the marker.

We now proceed to examine characteristics of the Galactic H_{II} emission nebulae. The brightest optical emission lines emanating from the Galactic H_{II} regions are from H_α and forbidden transitions of O_{II} , O_{III} , and N_{II} (Bowen, 1928; Herzberg, 1937). The two most intense lines originate from O_{III} transitions at green wavelengths of 5006.84 \AA and 4958.91 \AA . The relative intensities of the various nebular lines are indicative of the spectral class, and thus of the main sequence age, of the ionizing young stars. Their emitted ultraviolet ionizes the atomic

Figure 3.5 Nebulosity in the "belt" (ζ, ϵ, δ) and "sword" of the constellation Orion. β -Orionis is Rigel. Yerkes Observatory photograph.

10 pc
|-----|



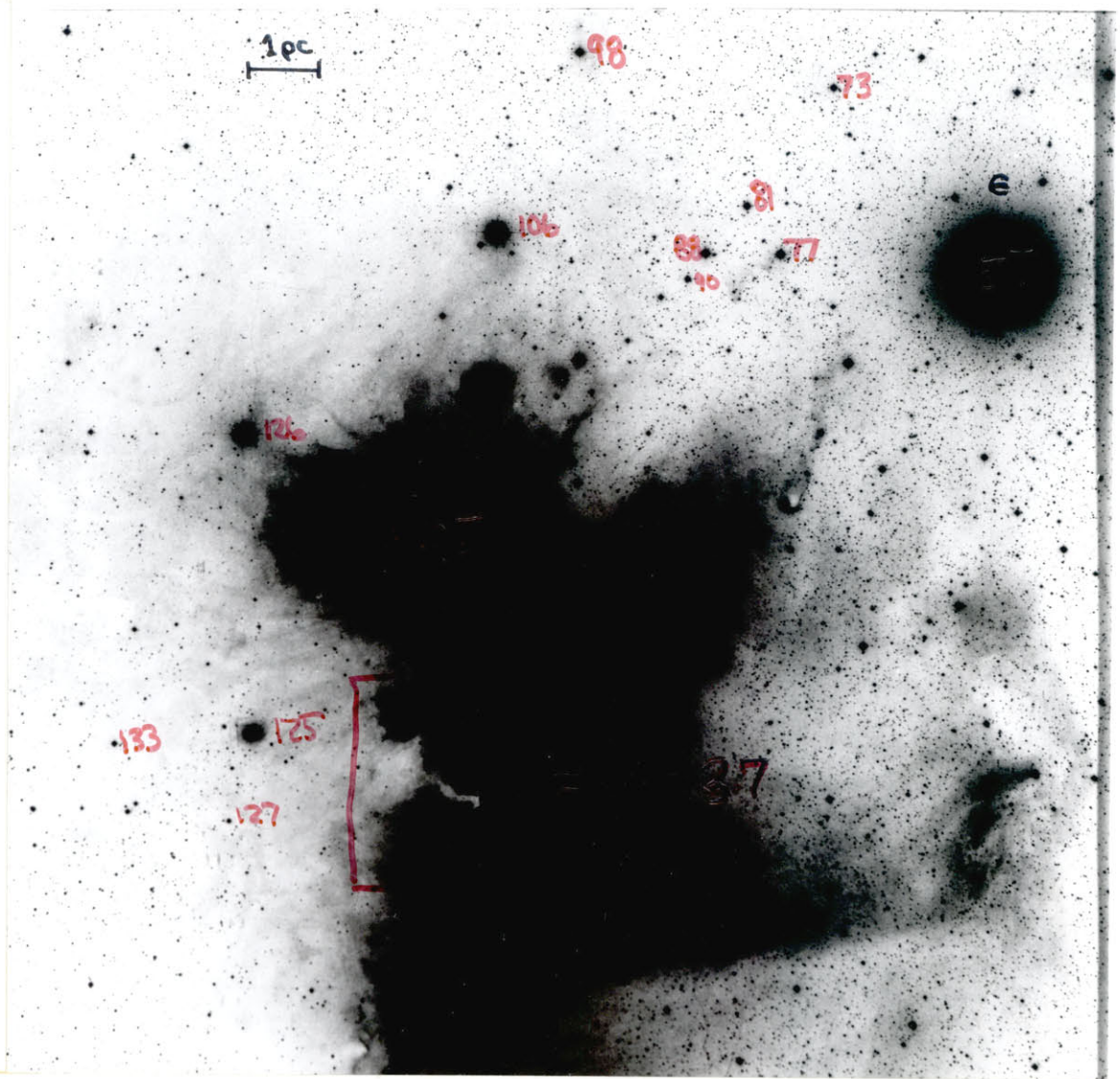


Figure 3.6 Nebulosity in the "belt" of the constellation Orion, near ζ -Orionis. Negative exposure reproduced from the Palomar Sky Survey.

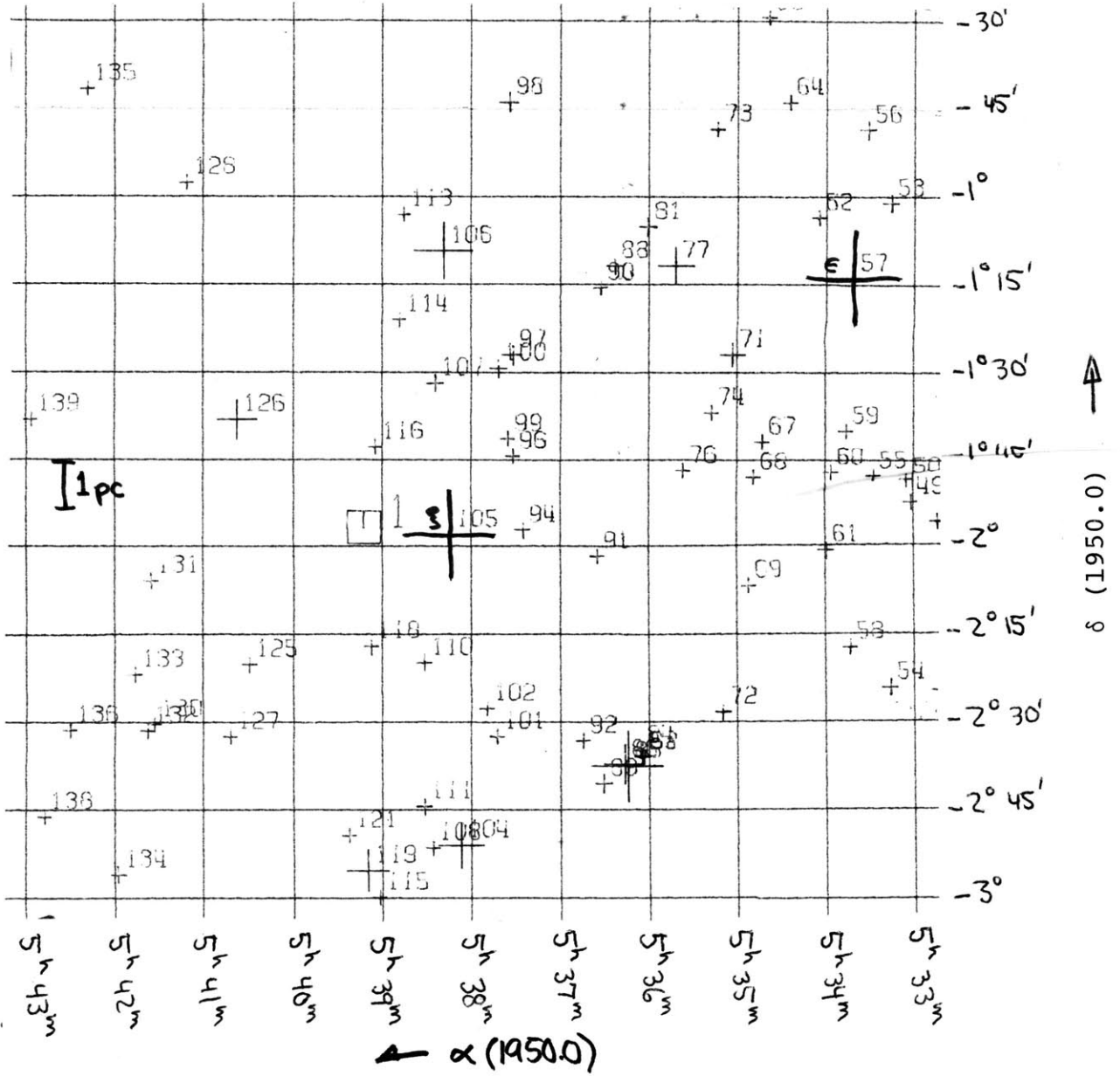


Figure 3.6b Star chart corresponding to Figure 3.6 (Orion B). Star #105 is ζ-Orionis.



Figure 3.7 The Horsehead Nebula (an obscuring H_I cloud) near ζ -Orionis. Yerkes Observatory photograph.

constituents ($H_I \rightarrow H_{II}$ at ~ 13.6 ev; $O_I \rightarrow O_{II}$ at ~ 35 ev; $O_{II} \rightarrow O_{III}$ at ~ 55 ev) and the excitation which leads to the optical emission of the species is provided by thermalized, several-electron-volt electrons. The optical emission thus acts to cool the H_{II} region. When there is insufficient ultraviolet for complete ionization, the appearance of a nebula is described as "radiation-bounded"; when there is insufficient gas, the appearance of the completely ionized nebula is described as "gas-bounded". Reference to Figure 3.3 shows that bright H_{II} regions often have long ($\sim 10^{2,3}$ parsec) gas-bounded tails extending outward and backward (in a rotational sense) from the spiral arms.

Younger than the Pleiades, emission nebulae such as NGC 6820 (optically obscured) are about $10^{5,6}$ years old (Kahn and Menon, 1961; Lasker, 1966). The central regions of such nebulae have been cleared due to the intense ultraviolet radiation of the young stars, as evident from the electron densities displayed in Figure 3.8a. A well known example of this age class of H_{II} regions is the Rosette Nebula (NGC 2237) in Monoceros.

The youngest H_{II} regions are $\sim 10^{4,5}$ years old (Vandervoort, 1963; Lasker, 1966), and the nebulae are still relatively intact, as evidenced by the electron density distribution of M16 shown in Figure 3.8b. Illustrative members of this youngest class of H_{II} regions are shown in Figures 3.9a (Orion Nebula, M42), 3.10a (Omega Nebula, M17), and 3.11a (IC 1795). Figures 3.9b, 3.10b, and 3.11b show the coordinate locations of the bright stars for the corres-

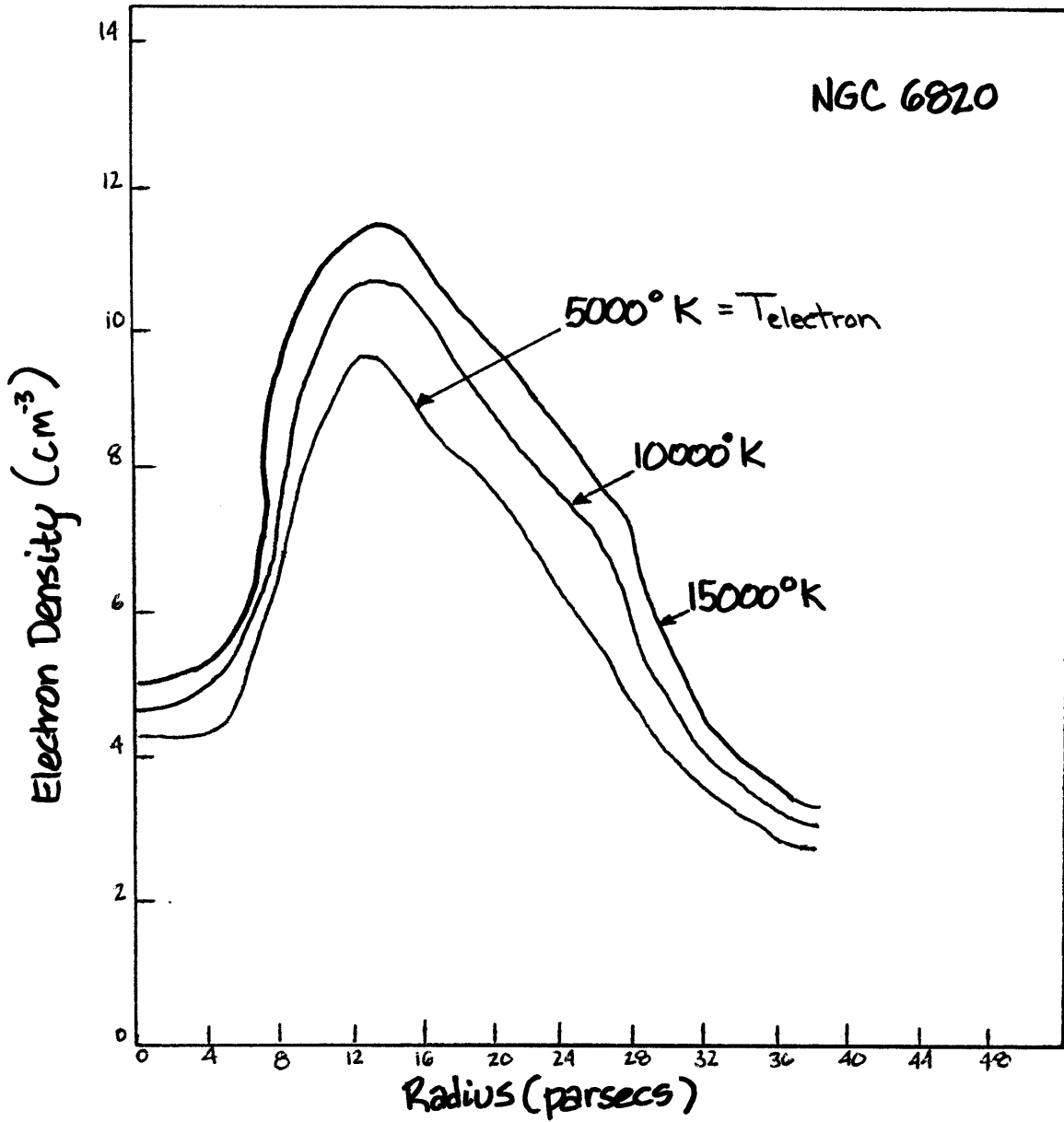


Figure 3.8 a The electron density near the center of the Galactic H_{II} region NGC 6820 (~2 x 10⁵ years old) as determined from radio continuum observations (Terzian, 1965).

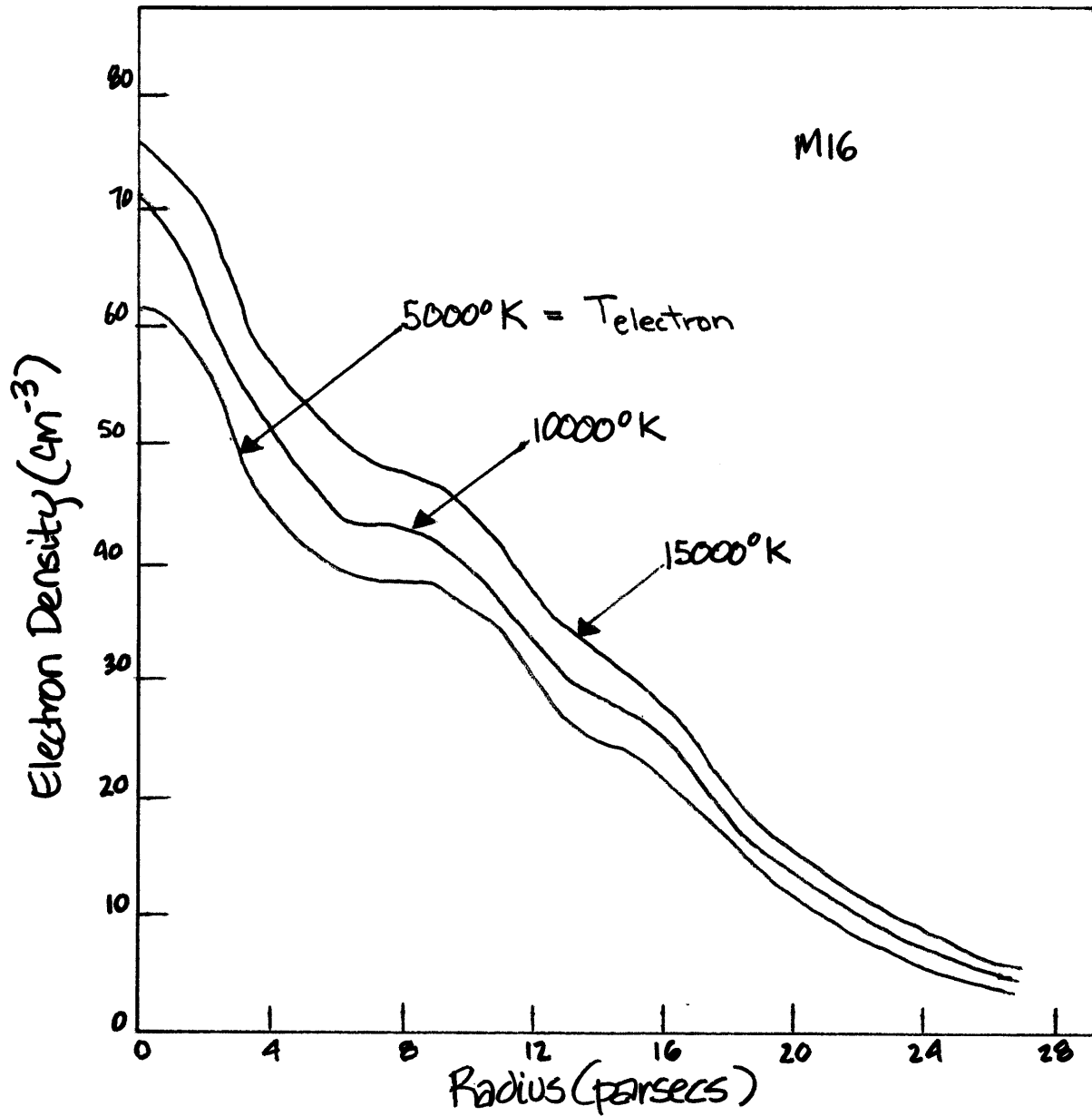


Figure 3.8 b The electron density near the center of the Galactic H_{II} region M 16 ($\sim 5 \times 10^4$ years old) as determined from radio continuum observations (Terzian, 1965).

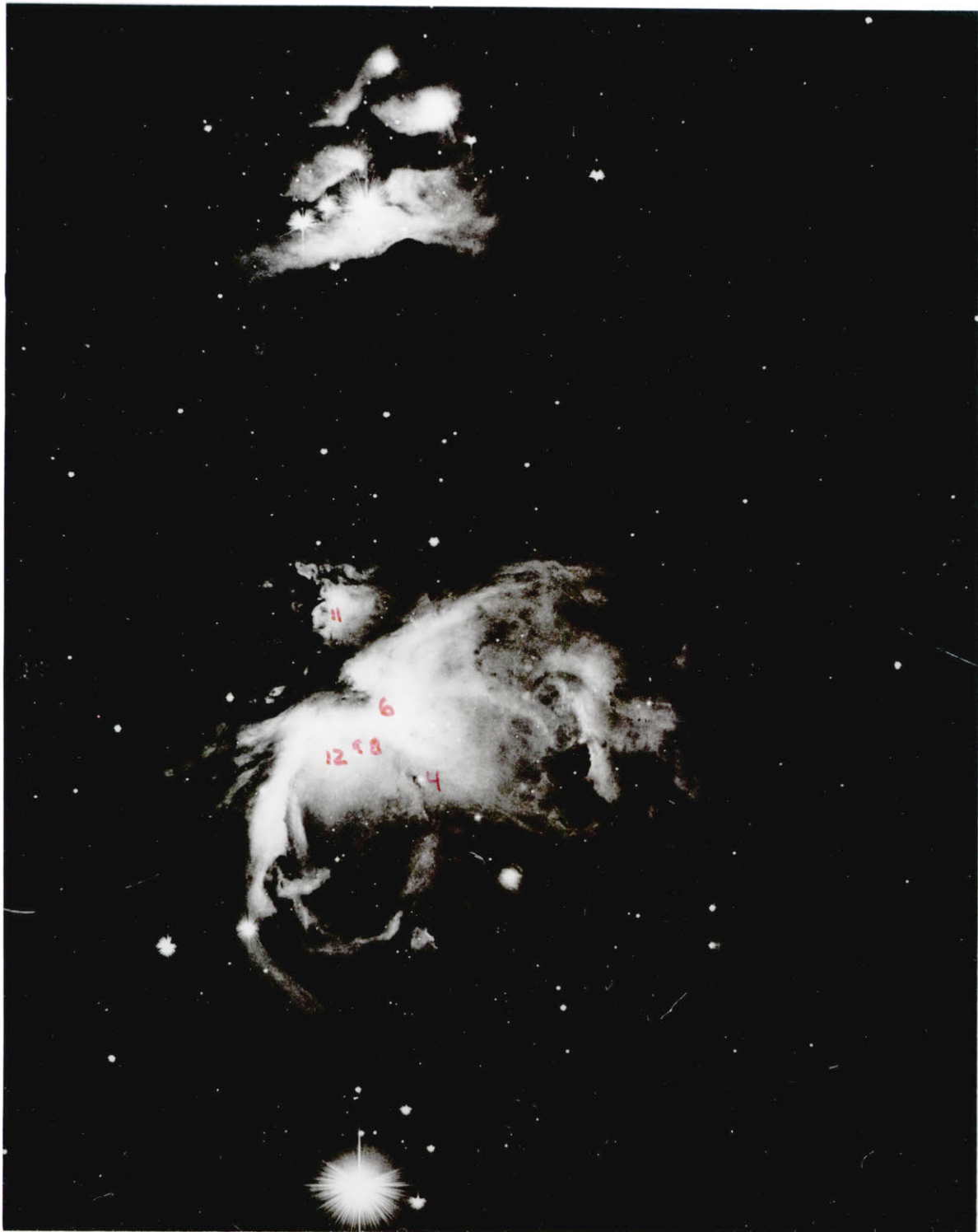


Figure 3.9a The Orion Nebula (M 42, NGC 1976) in the "sword" of the constellation.
Lick Observatory photograph.

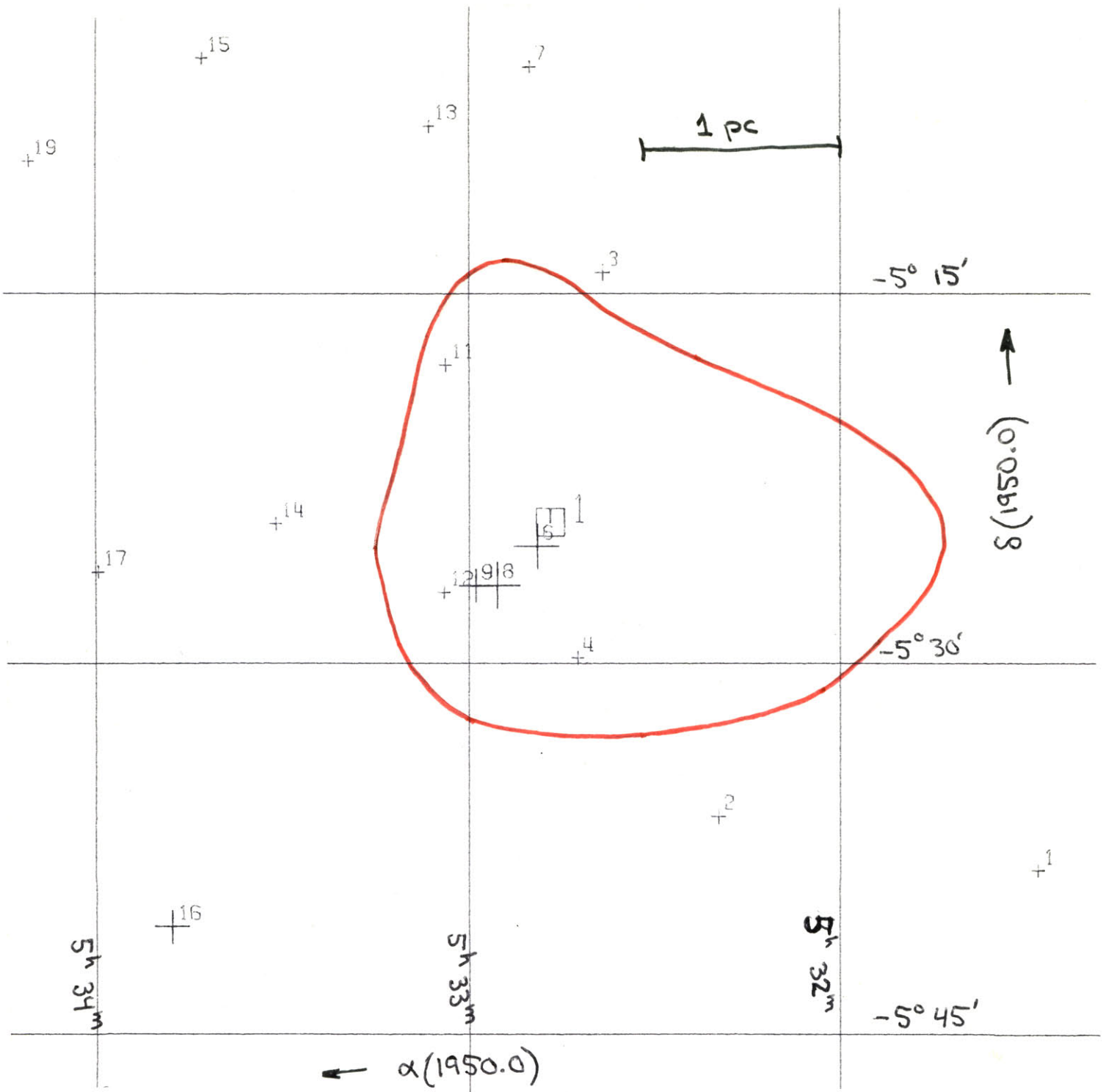


Figure 3.9b Star chart corresponding to Figure 3.9a (Orion Nebula, M 42). Star #6 is the O 6 class Trapezium star thought to be exciting the H_{II} region. The contour shown on this star chart, and those shown in Figures 3.10b and 3.11b, correspond to the outermost contour of the corresponding radio continuum contour maps (Figures 3.9c, 3.10c, and 3.11c).

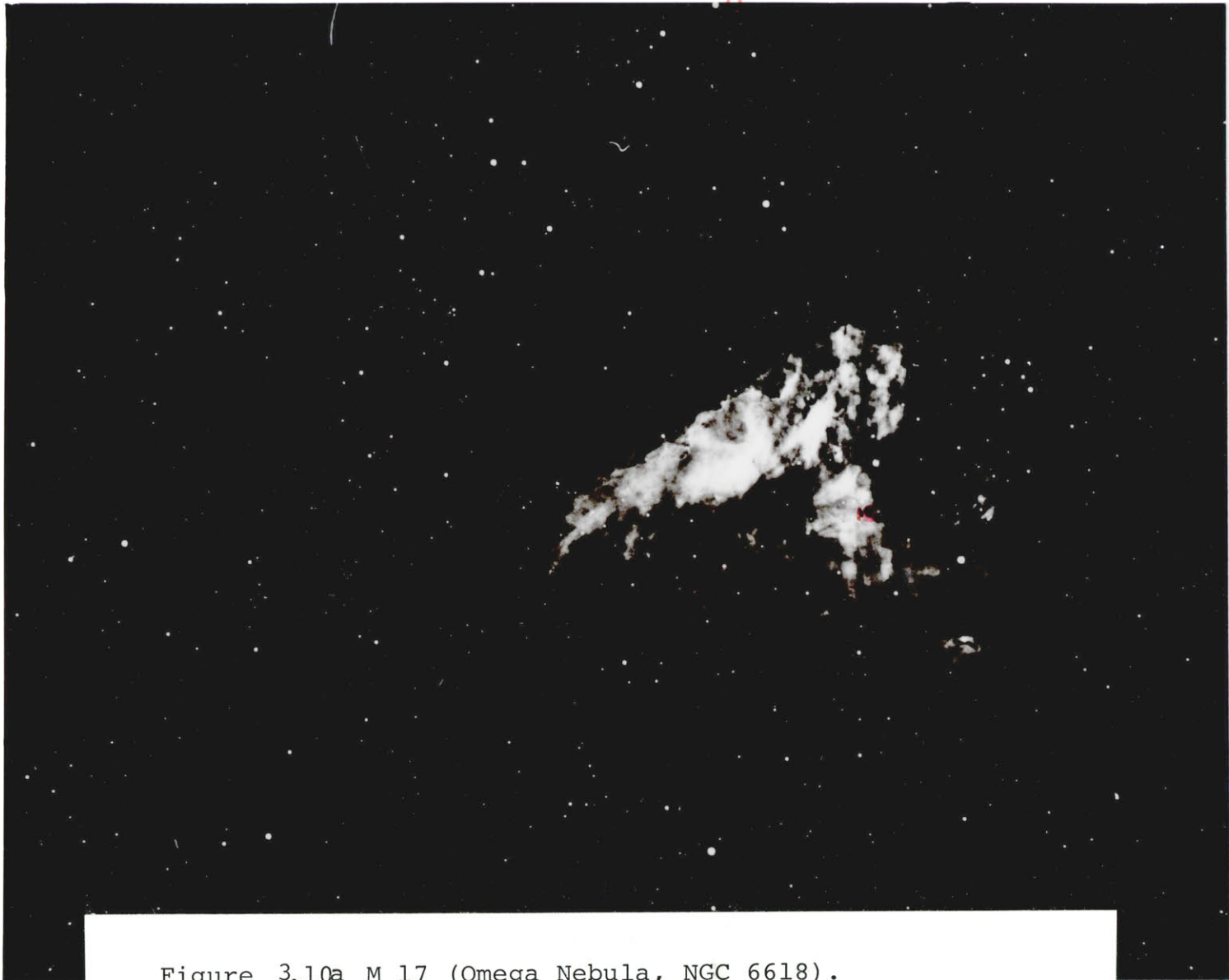


Figure 3.10a M 17 (Omega Nebula, NGC 6618).
Lick Observatory photograph.

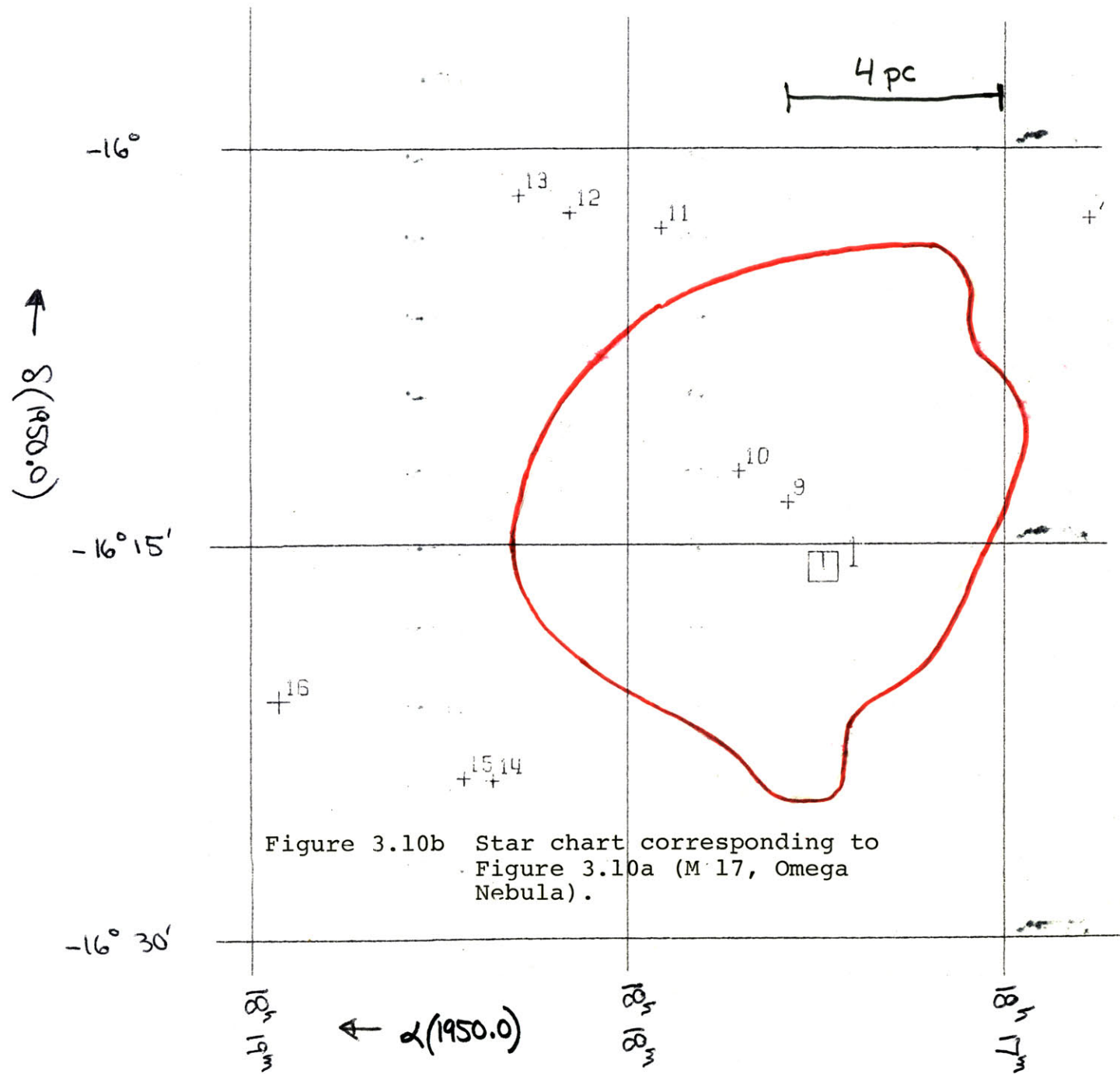


Figure 3.10b Star chart corresponding to Figure 3.10a (M 17, Omega Nebula).

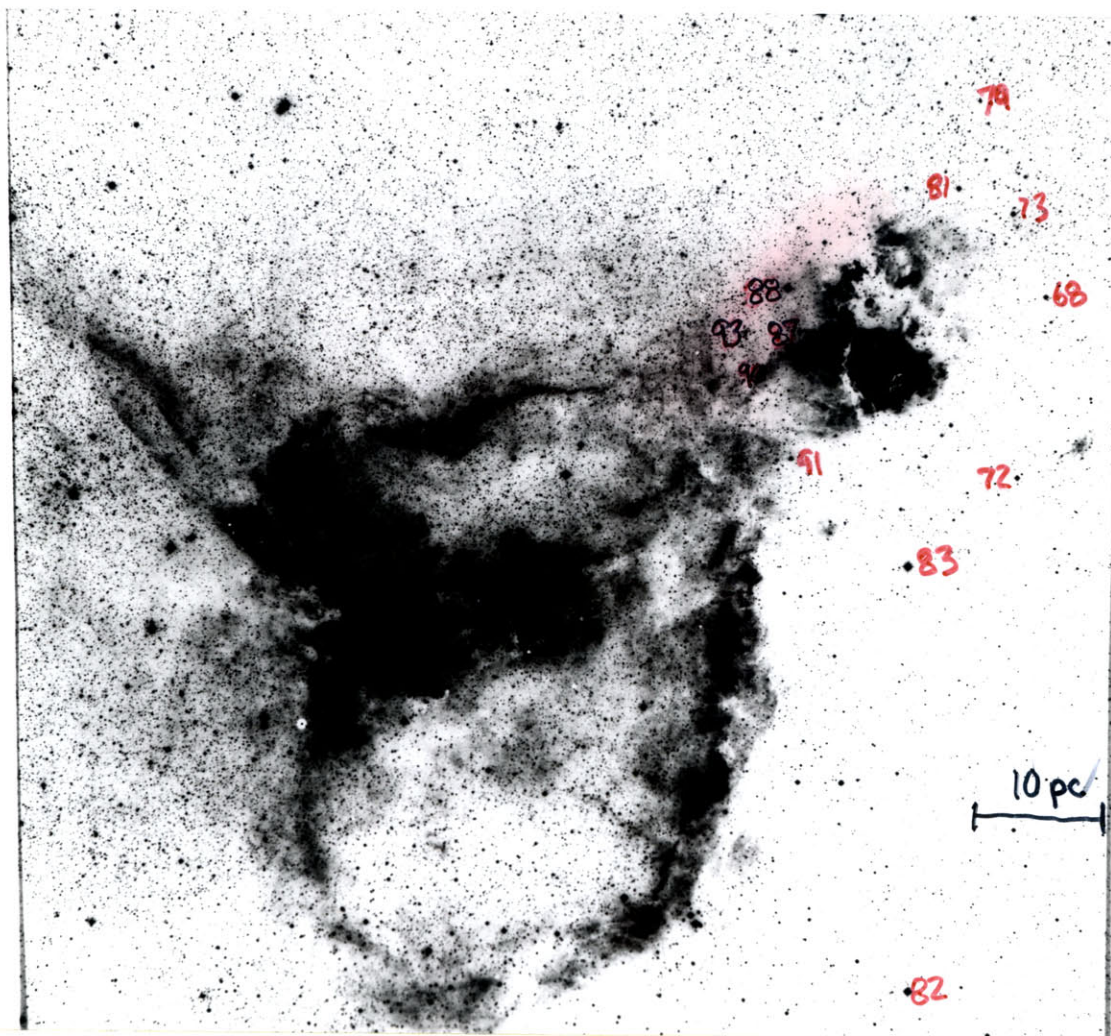


Figure 3.11a IC 1795, a negative exposure reproduced from the Palomar Sky Survey.

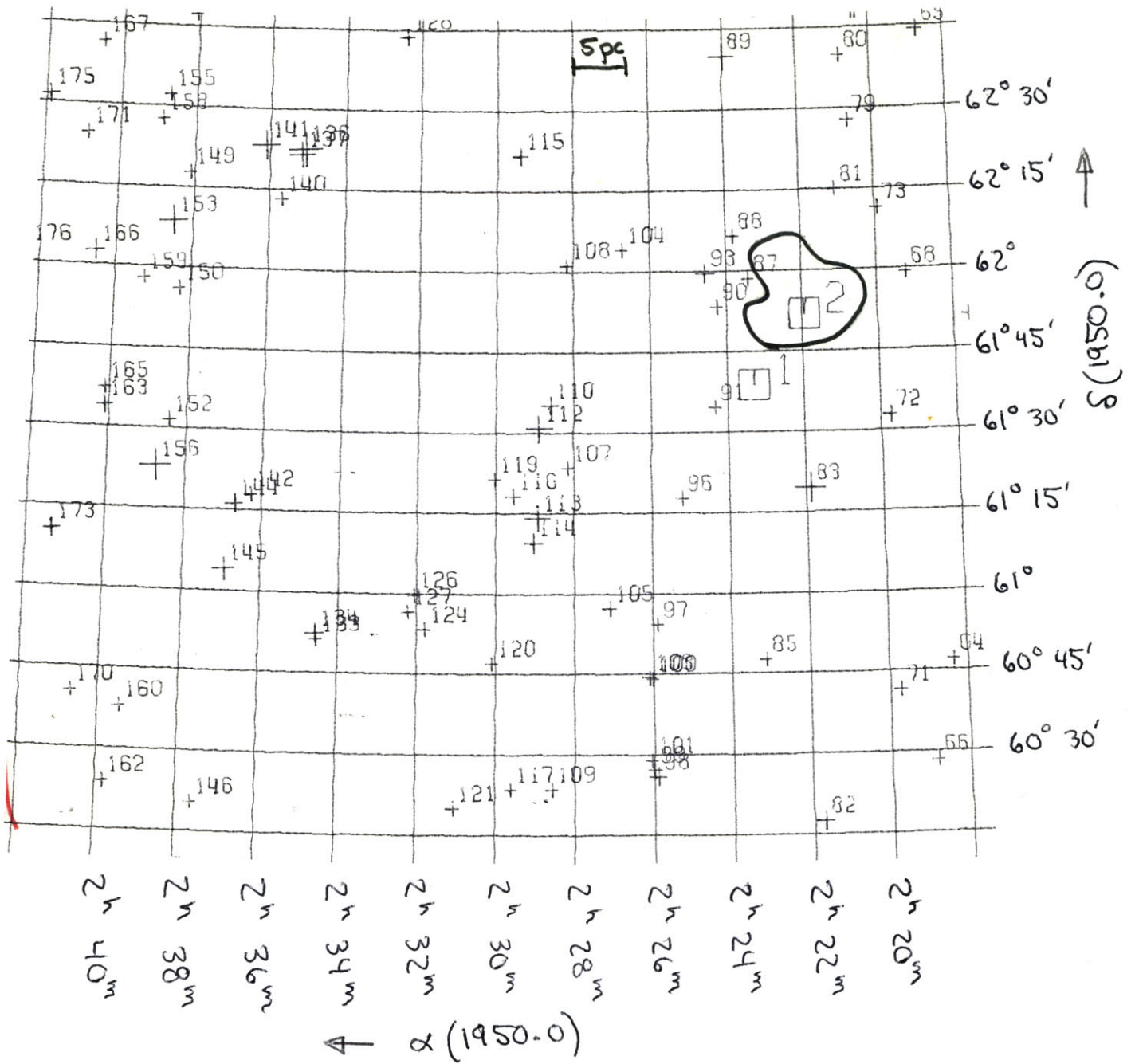
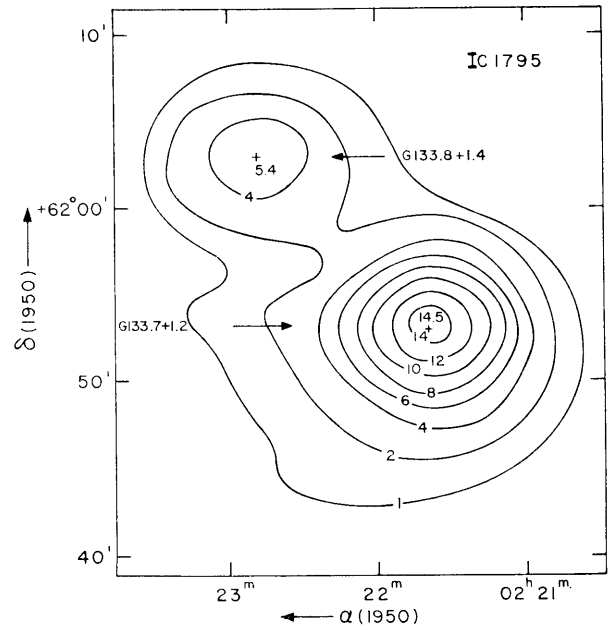
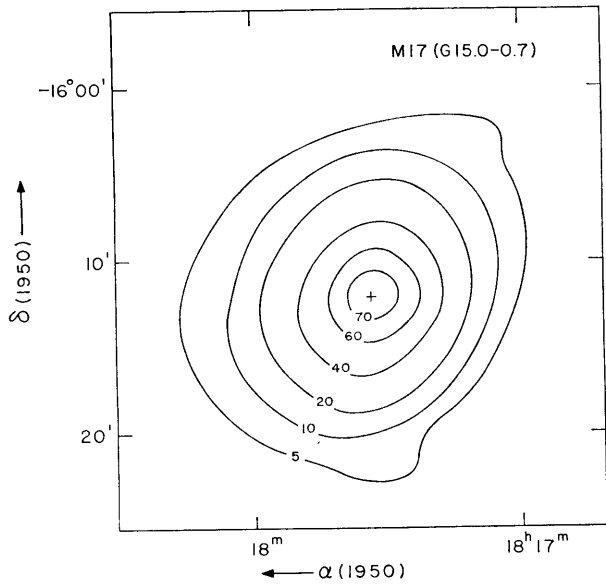
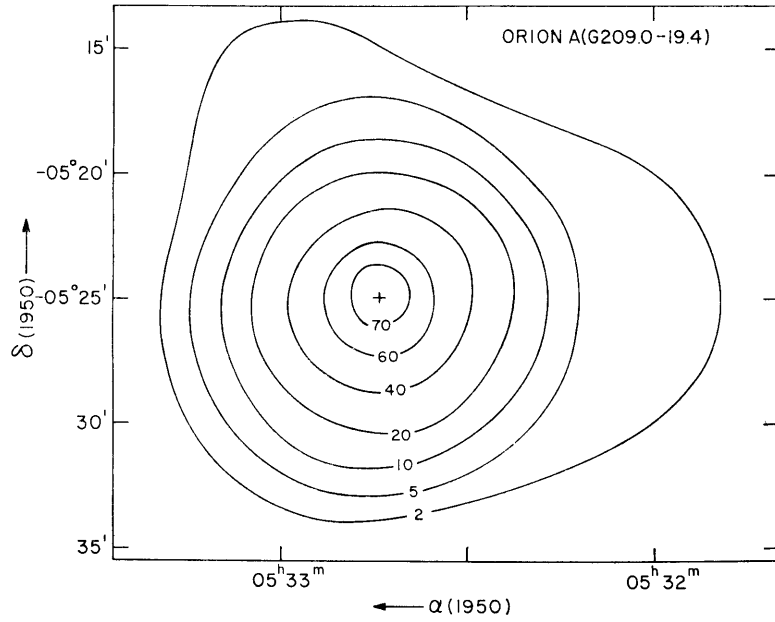


Figure 3.11 b Star chart corresponding to Figure 3.11a (IC 1795). The regions of H₂O maser emission marked by squares and numbers are 1] W3(OH) and 2] W3C.

ponding regions of sky from the SAO Star Catalogue (1966). Associated with these young optical emission nebulae are found radio continuum sources; the locations of these sources are shown for photographs 3.9 a, 3.10a, and 3.11a in Figures 3.9c, 3.10c, and 3.11c, respectively. The locations of the radio continuum sources are at the heads of the extended gas-bounded tails, in close proximity to the H_{II} - H_I interfaces.

The radio-infrared spectrum of a typical continuum region is shown in Figure 3.12. The radio frequency portion of the spectrum in Figure 3.12 is indicative of thermal radiation from ionized hydrogen (e.g. Terzian, 1965). Observations of H_{II} regions at the hydrogen recombination-line frequencies yield estimates of electron temperature and density, an rms value of internal turbulence, and a value for the radial velocity. Examples of such observations (Höglund and Mezger, 1965; Mezger and Höglund, 1967) are shown in Figure 3.13. The young H_{II} nebulae have electron temperatures of $\sim 10^4$ °K, and estimates of mass deduced from their angular extent and density range from $\sim 10^3$ to $\sim 10^5$ stellar masses. Internal turbulence in these nebulae has an rms value of ~ 20 km s⁻¹. This value compares with a Galactic rotation velocity for the sun of ~ 300 km s⁻¹, and an rms dispersion of ~ 15 km s⁻¹ among local group Population I stars. Use of the hydrogen recombination-line radial velocities with a model of Galactic rotation (IAU 1963) yields kinematic distances (Becker and Fenkart 1963; Mezger and Höglund, 1967). Figure 3.14 shows the resultant Galactic distribution of the radio H_{II} regions in



Figures 3.9 c, 3.10 c, 3.11 c Radio continuum maps at 5 GHz of the H_{II} regions associated with a) the Orion Nebula (M 42), b) M 17 (Omega Nebula), c) IC 1795. Contours are in units of antenna temperature (°K). Reproduced from Mezger and Henderson (1967).

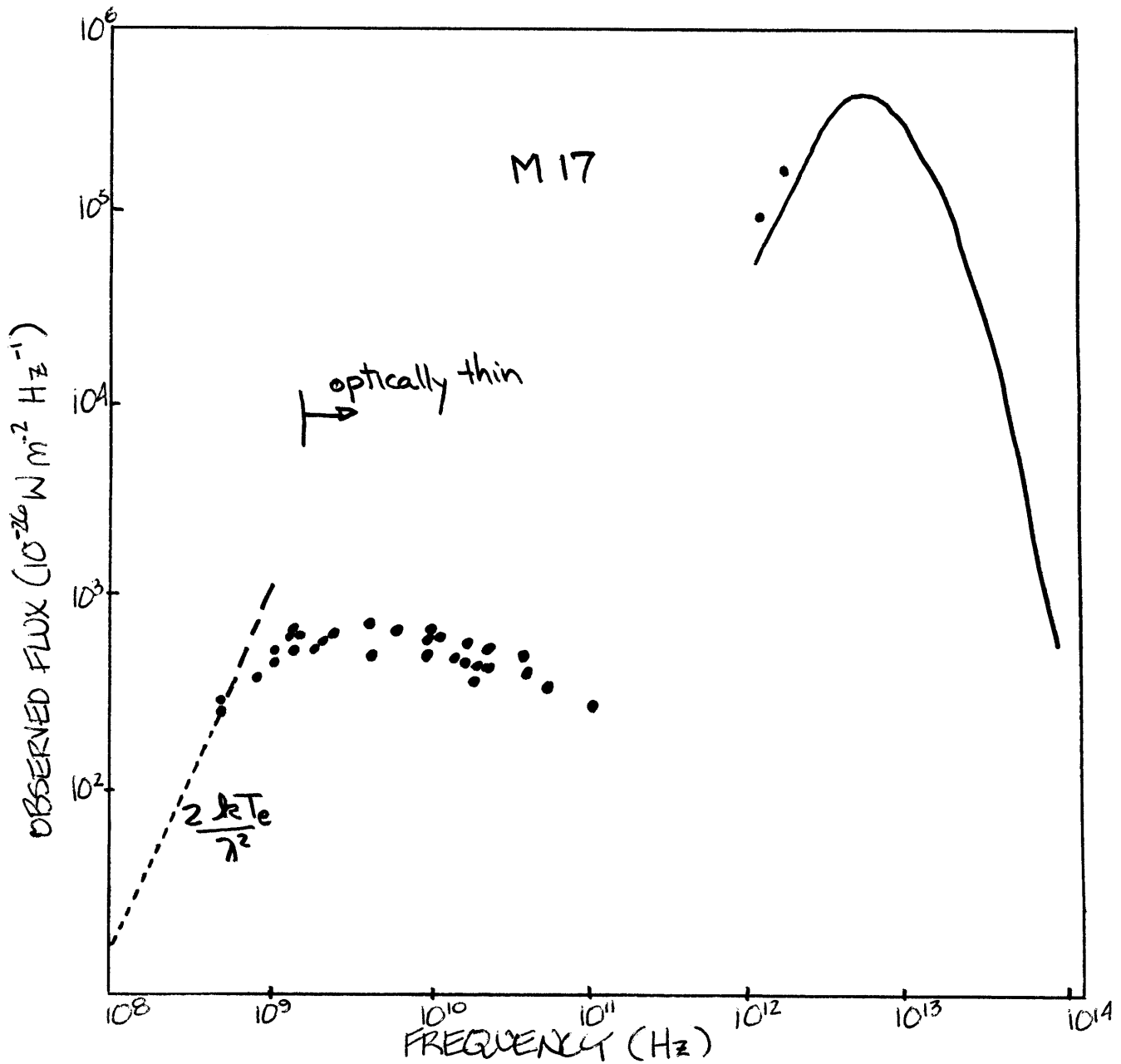


Figure 3.12 Radio-infrared spectrum of M 17 (Omega Nebula).
Reproduced from Johnston and Hobbs (1973).
Points denote observations; dashes indicate theory.
A theoretical derivation of the continuum radio flux
expected from a diffuse nebula is contained in
Terzian (1965).

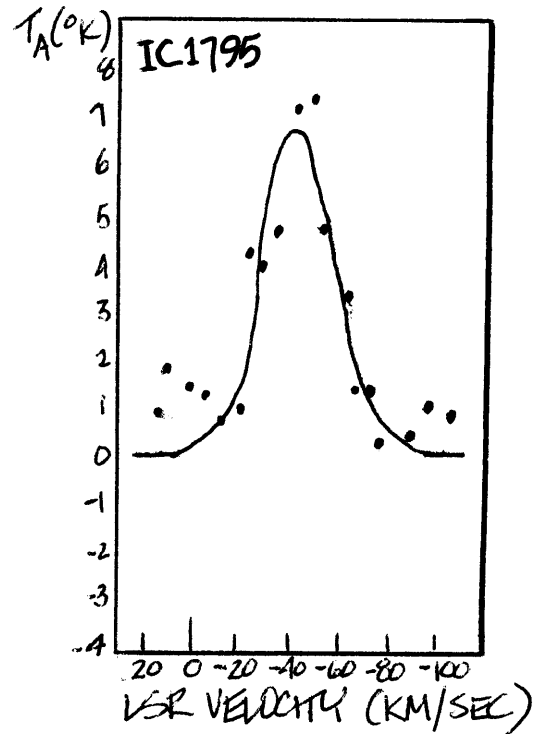
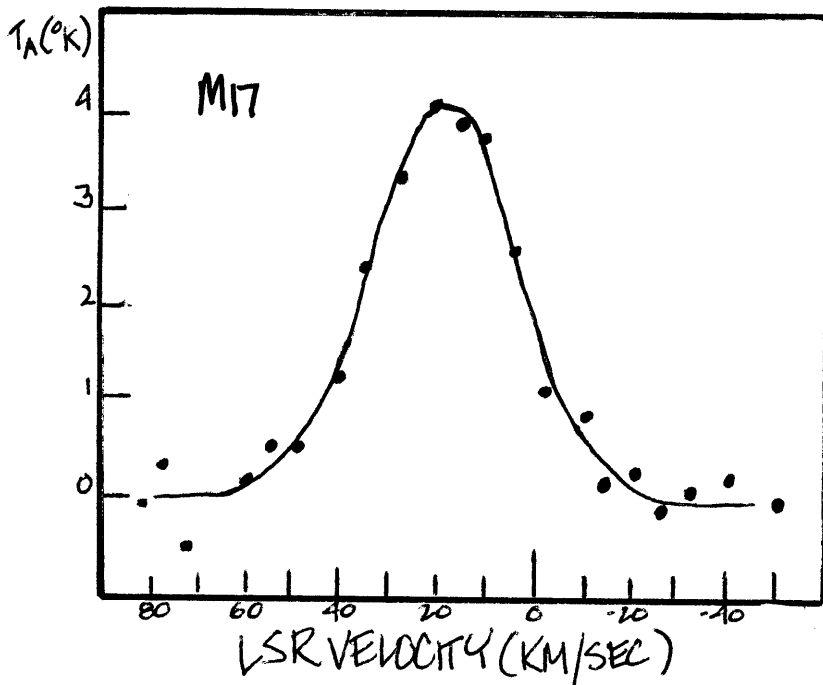
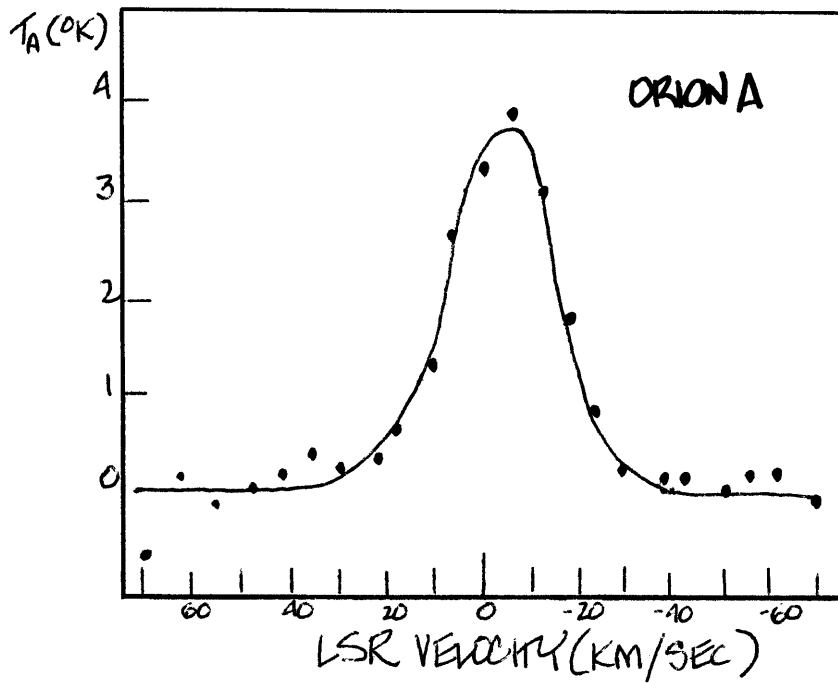


Figure 3.13 Hydrogen recombination line ($n_{110} \rightarrow n_{109}$; 5.009 GHz) observations of M 42, M 17, and IC 1795. From Höglund and Mezger (1965) and Mezger and Höglund (1967). Velocity shown is with respect to the local standard of rest (LSR).

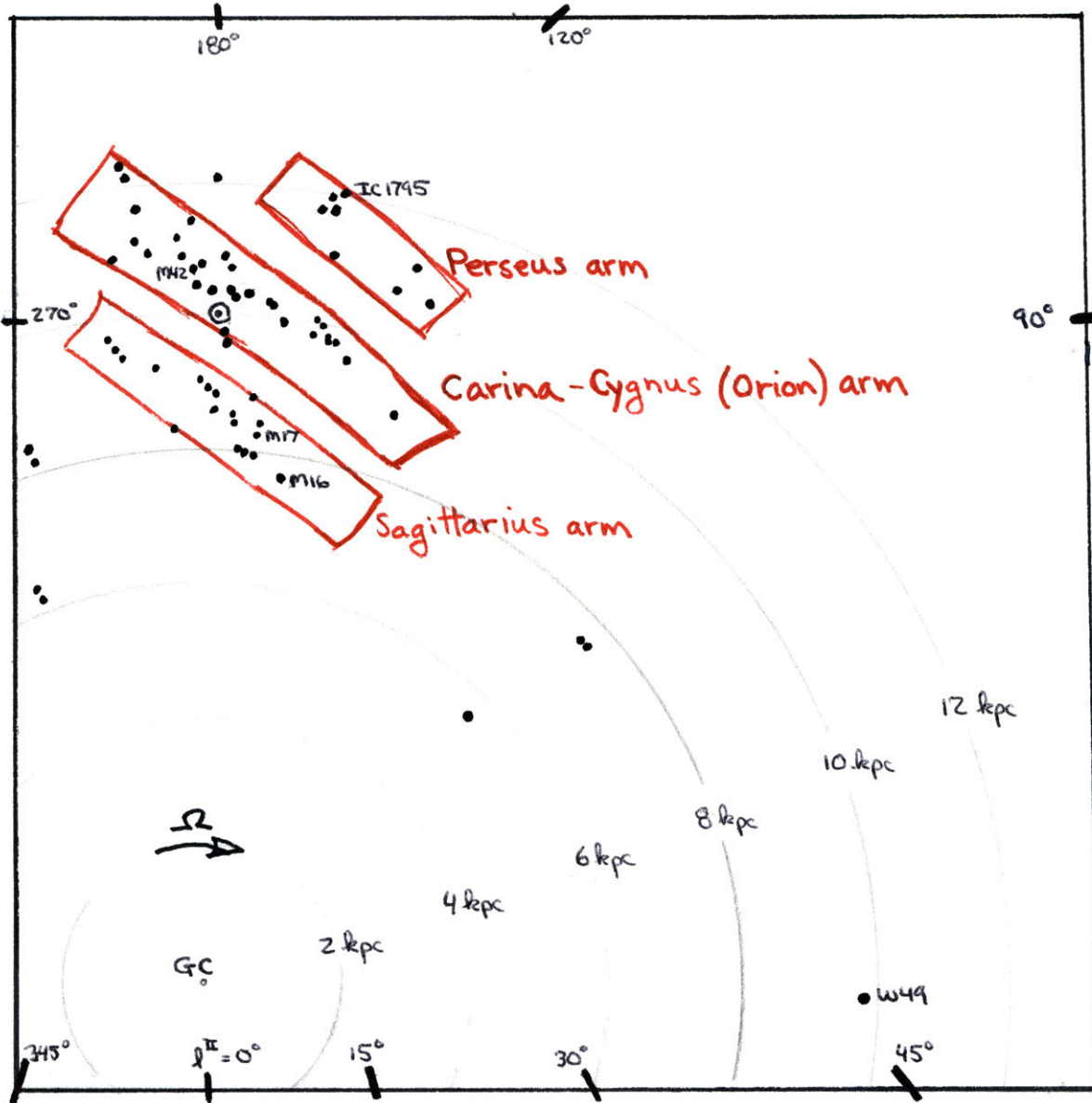


Figure 3.14 Distribution of radio H_{II} regions in the Galactic plane. Reproduced from Mezger and Höglund (1967). The local spiral arms are indicated. (Note that the current best estimate of Galactic distances places the sun about 15% closer to the Galactic center.)

which the local spiral arms are well defined.

Also evident in Figure 3.12 is the presence of an intense source in the infrared. This association with IR sources is representative of the regions of continuum radio emission associated with the young Galactic H_{II} regions. In the Orion Nebula (M42) the well known Becklin-Neugebauer infrared source was discovered in 1967; a succession of similar objects has been detected more recently (Wynn-Williams, Becklin, and Neugebauer, 1972). Larson (1972) feels the characteristics of these objects are indicative of $\sim 5M_{\odot}$ protostars. Mapping observations indicate the point sources of infrared emission are interior to H_I molecular clouds such as the Kleinmann-Low nebula in Orion. A wealth of molecules (over 26 to date) have been observed at radio frequencies in the excited H_I clouds associated with young Galactic H_{II} regions. Observations of these molecules lead to estimates of H_I temperature and density. We adopt $T \sim 10^{\circ}K$ and $\rho_{H_2} \sim 10^{11} m^{-3}$ as representative (e.g., Snyder and Buhl, 1971; Thaddeus et al., 1971).

As a summary of our preceding examination of Galactic H_{II} regions, we present in Figure 3.15 a schematic representation of a young Galactic H_{II} region with associated ionizing star and H_I cloud. In the region comprising the H_{II} - H_I transition zone, the H_I region is being compressed and heated. The H_{II} - H_I interface appears attractive as a primary stellar womb.

Remote investigation of the physical conditions existing in the H_{II} - H_I transition zones is facilitated by the presence of molecular masers emitting at radio frequencies. In Chapter 4 we consider these molecular masers further.

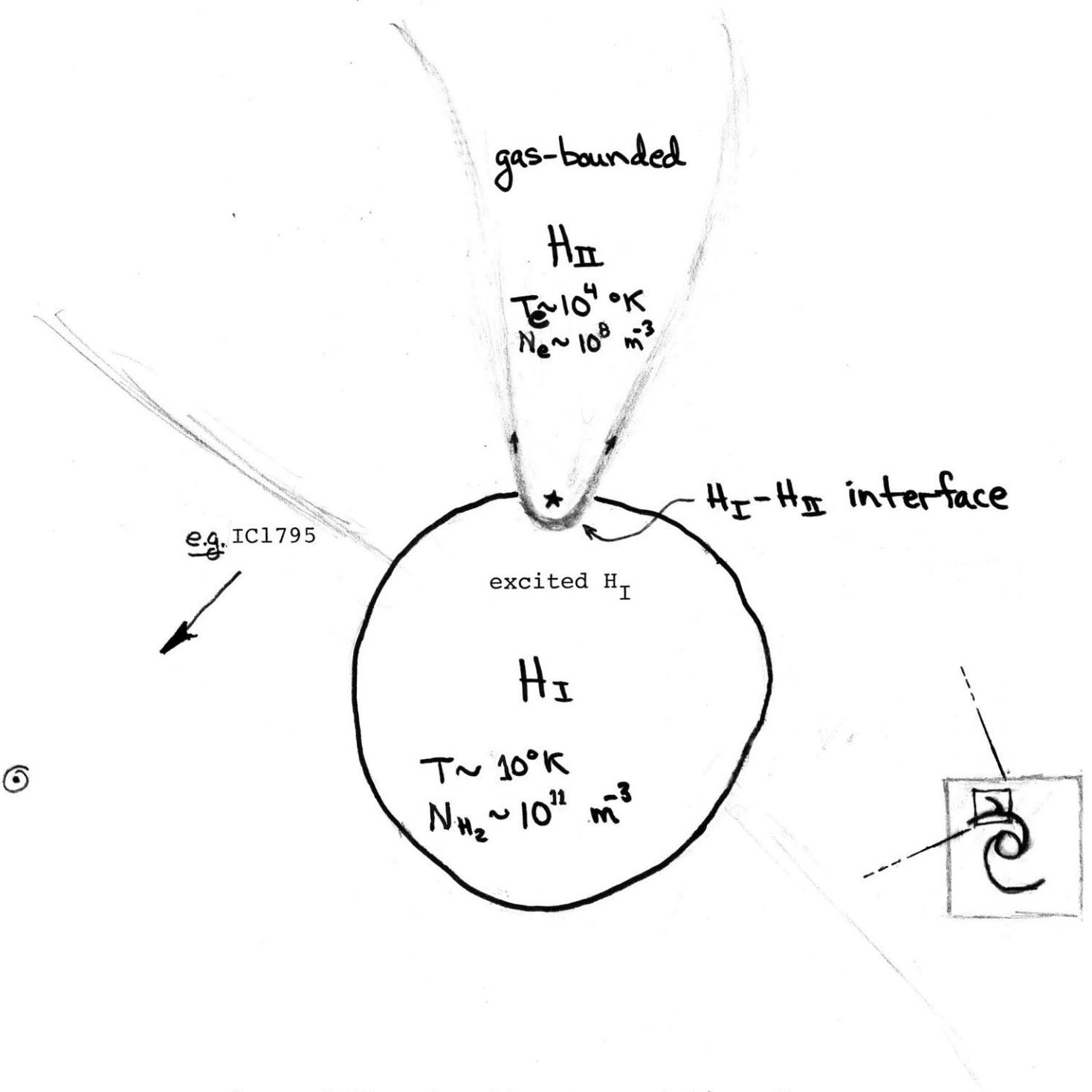


Figure 3.15 Schematic representation of a young Galactic H_{II} region, its ionizing O star, and associated H_I cloud.

CHAPTER 4

HIGH RESOLUTION RADIO OBSERVATIONS OF H₂O MASERS
AS A MEANS OF PROBING REGIONS OF STELLAR FORMATION

4.1 Introduction

We wish to examine those regions in ~~our~~ Galaxy associated with current stellar production at a sufficiently high resolution to enable physical conditions and dynamics associated with stellar formation to be deduced. To succeed in such an endeavor two primary requirements must be satisfied: (1) the technological ability to examine appropriate regions, at typical distances of $\sim 10^3$ parsecs, with sufficient angular resolution to discern spatial scales of ~ 1 A.U. at the radio sources (since 1 A.U. at 1 parsec is equivalent to 1 arc second, the required angular resolution is 10^{-3} arc second); and (2) the presence of suitable microwave sources.

The technique of very long baseline radio interferometry (VLBI) is capable of providing the specified angular resolution. By combining simultaneous observations recorded at widely separated radio telescopes, VLBI provides angular resolution approximately equivalent to that of a single radio telescope with diameter equal to the separation between observatories (the length of the "baseline"). A brief mathematical introduction to VLBI follows in Section 4.2.

The potential ability of the known molecular masers (OH, H₂O, SiO) to provide suitable radio sources for our purposes is

considered in the succeeding section (Section 4.3), and the selection of H_2O masers for further detailed examination in this investigation is justified. The thrust of this investigation is directed toward extracting the existent dynamics and physical conditions in the regions of interest from radio observations of H_2O masers. In the final section of this chapter (Section 4.4), we begin this endeavor by describing the H_2O $6_{16} \rightarrow 5_{23}$ maser transition in greater detail.

4.2 Very Long Baseline Radio Interferometry

In very long baseline interferometry (VLBI) the emission of a radio source in a frequency band referenced to the local standard of rest is simultaneously recorded at two radio observatories. If $X_1(t)$ is the signal in this frequency band that is arriving at the first telescope from an infinitely distant source at time t , then the corresponding signal arriving at the second telescope is $X_2(t + \tau) = X_1(t)$. If atmospheric and ionospheric effects are neglected, the delay, τ , equals $\underline{\underline{B}} \cdot \hat{s}/c$, where $\underline{\underline{B}}$ is the baseline vector from telescope 2 at time $t + \tau$ to telescope 1 at time t , \hat{s} is the unit vector in the direction of the source, and c is the speed of light. The delay may equivalently be expressed in terms of a phase as $\phi = 2\pi\nu\tau$, where ν is the microwave observing frequency, and undergoes a sinusoidal variation due to the sidereal rotation of the earth.

The variation of the delay with \hat{s} provides the angular resolution of the interferometer. If the baseline vector is projected onto the plane perpendicular to \hat{s} (the "celes-

tial sphere") in the direction of \hat{s} , it will describe a diurnal ellipse. At any given time, the delay will be constant along lines on the celestial sphere that are perpendicular to the projected baseline. The use of additional observatories and the rotation of the earth permit many independent determinations of delay over a sidereal day. In this manner information may be compiled about the angular distribution of radio emission in right ascension (α) and declination (δ). When the radio source is composed of unresolved point components, compilation of a data set which yields unique determinations of position is relatively straightforward, as will be demonstrated in Section 5.1.1.

4.3 Molecular Maser Radio Sources

The first astrophysical molecular maser source detected was OH ($\lambda = 18$ cm; $\nu_0 = 1.6$ GHz) in 1965 (Weaver, Williams, Dieter, and Lum, 1965), followed by H₂O ($\lambda = 1.35$ cm; $\nu_0 = 22$ GHz) in 1968 (Cheung et al., 1969), and by SiO ($\lambda = 0.34$ cm; $\nu_0 = 86$ GHz) in 1973 (Snyder and Buhl, 1974). Astrophysical conditions required to produce these molecular masers are apparently so selective that the sources of the maser radio emission require the angular accuracy provided by VLBI to resolve. Although the physical extent of the "masing" regions is small, the maser amplification mechanism provides sufficient photon output to allow their detection on earth. The small size of these regions first began to be appreciated when the initial radio astronomical ob-

servations utilizing interferometry determined that the radiation from OH sources originated from as yet unresolved, spatially separate, Doppler shifted emission features (Moran, 1968).

Since their initial discoveries, numerous Galactic* OH, H₂O and SiO masers have been located. OH, H₂O, and SiO masers have been found associated with infrared stars, while OH (Type I) and intense H₂O masers are found associated with H_{II} regions. The high dissociation energy of SiO permits the molecule to remain intact at the higher thermal temperatures in the infrared star environment which are responsible for population of the first and second vibrational states from which the rotational maser transitions originate. A more complete discussion of the SiO maser transitions is contained in Snyder and Buhl (1975). As yet no VLBI observations of SiO have been successful.

For the purposes of this investigation we will consider further only the intense OH and H₂O masers associated with Galactic H_{II} regions. The Doppler shifts of OH and H₂O masers are found to fall well within the turbulence broadened continuum envelopes of the associated H_{II} regions (see Figure 3.13). The radial velocities of the OH and H₂O sources often overlap but no correlation is apparent. As the technological state of the radio interferometer observations improved, it has been possible to

* An unsuccessful attempt to detect H₂O masers in M31 (Andromeda) was made by the author at Haystack Observatory. In the observing program, designated Reisz-1, ~25 bright H_{II} regions identified by Baade and Arp (1964) were searched.

determine accurately the relative angular distribution of emission features, and their apparent transverse extents. OH and H₂O masers are found to be distributed over regions which are spatially coincident to within the absolute accuracy of the separate observations (a few arc seconds). Typical OH emission features appear to be $\sim 10^2$ A.U. in transverse extent, while those H₂O features resolved are typically ~ 1 A.U. The maximum observed radio flux density ($10^{-26} \text{ Wm}^{-2} \text{ Hz}^{-1} = \text{Jy}$) from H₂O masers is often an order of magnitude larger than that observed from the associated OH sources.

The OH spectra result from Λ doubled transitions in the $^2\Pi_{3/2}$, $J=3/2$ rotational state. Λ doubling arises due to the interaction between the unpaired electron and the molecular rotation in which two electronic configurations are possible -- a higher energy orientation in which the electron distribution is along the molecular rotation axis, and a lower state in which it is in the plane of rotation. Each Λ doublet is further hyperfine split into two ($2I+1$; $I = 1/2$) F levels, where $\tilde{F} = \tilde{J} + \tilde{I}$, due to the interaction between the nuclear magnetic moment of the hydrogen and the molecular magnetic moment (resulting, primarily, from the unpaired electron). In Type I OH sources the $\Delta F=0$ Λ doublet transitions at 1665 MHz and 1667 MHz are observed to be the most intense.

In a manner similar to the case of OH, the H₂O $J=5,6$ molecular rotational levels are each hyperfine split into three ($2I+1$; $I=1/2 + 1/2 = 1$) F levels. The magnitude of the hyper-

fine frequency splitting in the case of H_2O , however, is approximately a factor of $\frac{\mu_{nuc}}{\mu_{Bohr}} = \frac{m_{electron}}{m_{proton}} = \frac{1}{1836}$ less than in the case of OH, where μ denotes magnetic moment. Thus the frequency separation of hyperfine components in the H_2O maser transition will be $\sim \frac{(1720-1665)}{1836}$ MHz = 30 KHz, and the susceptibility of H_2O molecules to the presence of weak magnetic fields ($\sim 5 \times 10^{-3}$ gauss; Beichman and Chaisson, 1975) in the sources would be about $\frac{1}{1836}$ less severe than for OH.

Calculations of molecular abundances based upon chemical equilibrium in a solar composition gas are shown in Figures 4.1, 4.2, and 4.3 for a range of temperature and density relevant to a protoplanetary nebula*. It is evident from these figures that in the low temperature, high pressure regime (below the T-P contour of the H-H₂ boundary indicated in the figures) in which molecules primarily exist, the H_2O molecule is the most abundant of the masing molecules.

In several ways thus far we have found that the H_2O molecule offers us the best potential probe of those regions along the spiral arms of the Milky Way associated with current stellar formation. There remains little further impediment to an observational continuation to this investigation since additionally: (1) low noise receivers and spectral correlators exist at Ku band; (2) the earth's atmosphere and ionosphere at Ku-band do not corrupt radio interferometric observations significantly, even on the longest of earth-based baselines (Burke et al.,

*The computations from which these figures were prepared were provided by S. Barshay and J. S. Lewis, Department of Earth and Planetary Sciences, M.I.T.

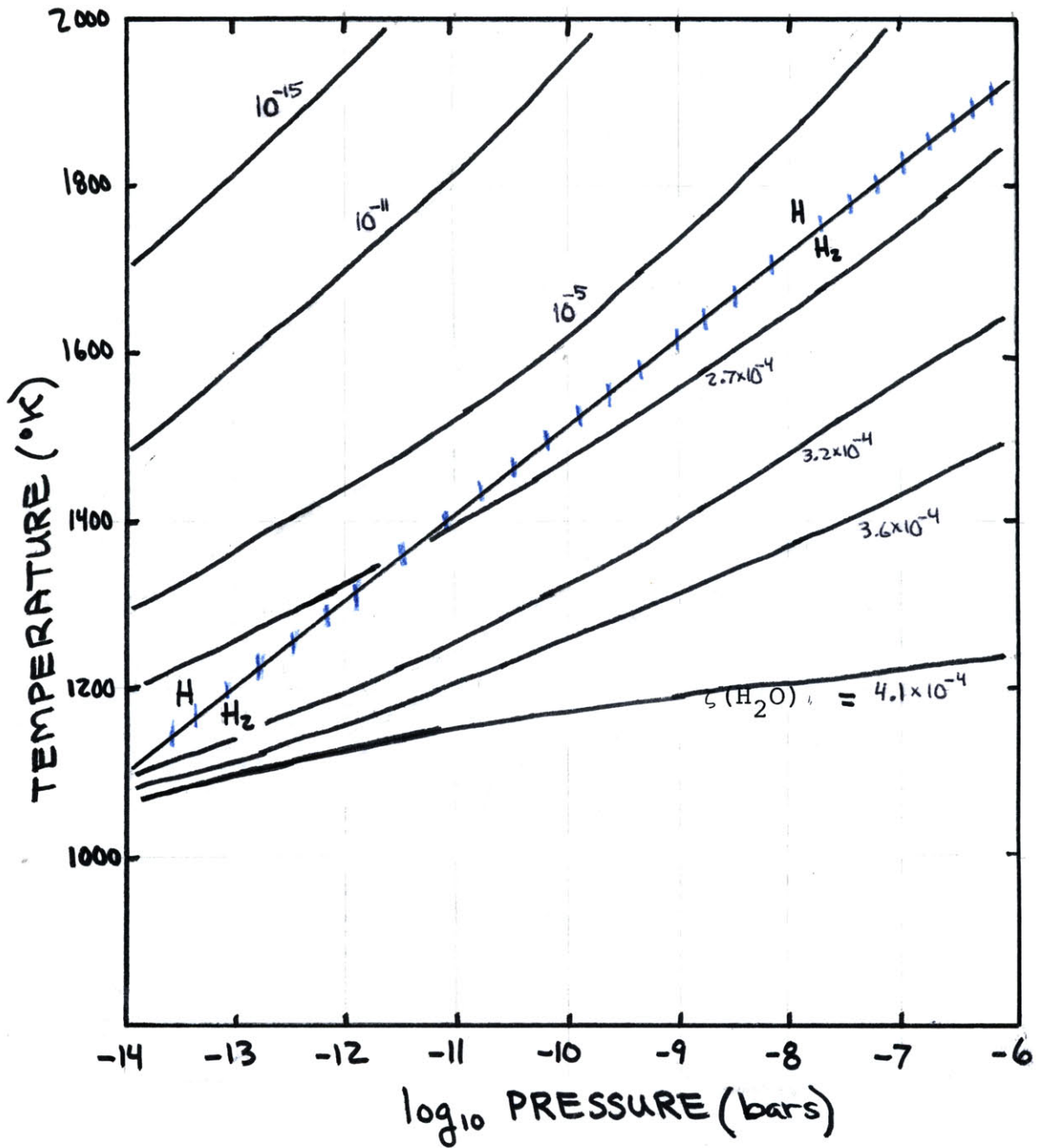


Figure 4.1 T-P contours of $\zeta(\text{H}_2\text{O}) \equiv$ the ratio of the H_2O partial pressure to the total pressure for solar composition gas in chemical equilibrium. Above the H- H_2 T-P boundary marked, H is more prevalent than H_2 . Over the T-P range shown here, $\zeta(\text{H}_2\text{O}) \sim \zeta(\text{CO})$. The computations from which this figure, and Figures 4.2, and 4.3 were prepared were provided by S. Barshay and J. S. Lewis, Dept. of Earth and Planetary Sciences, M.I.T.

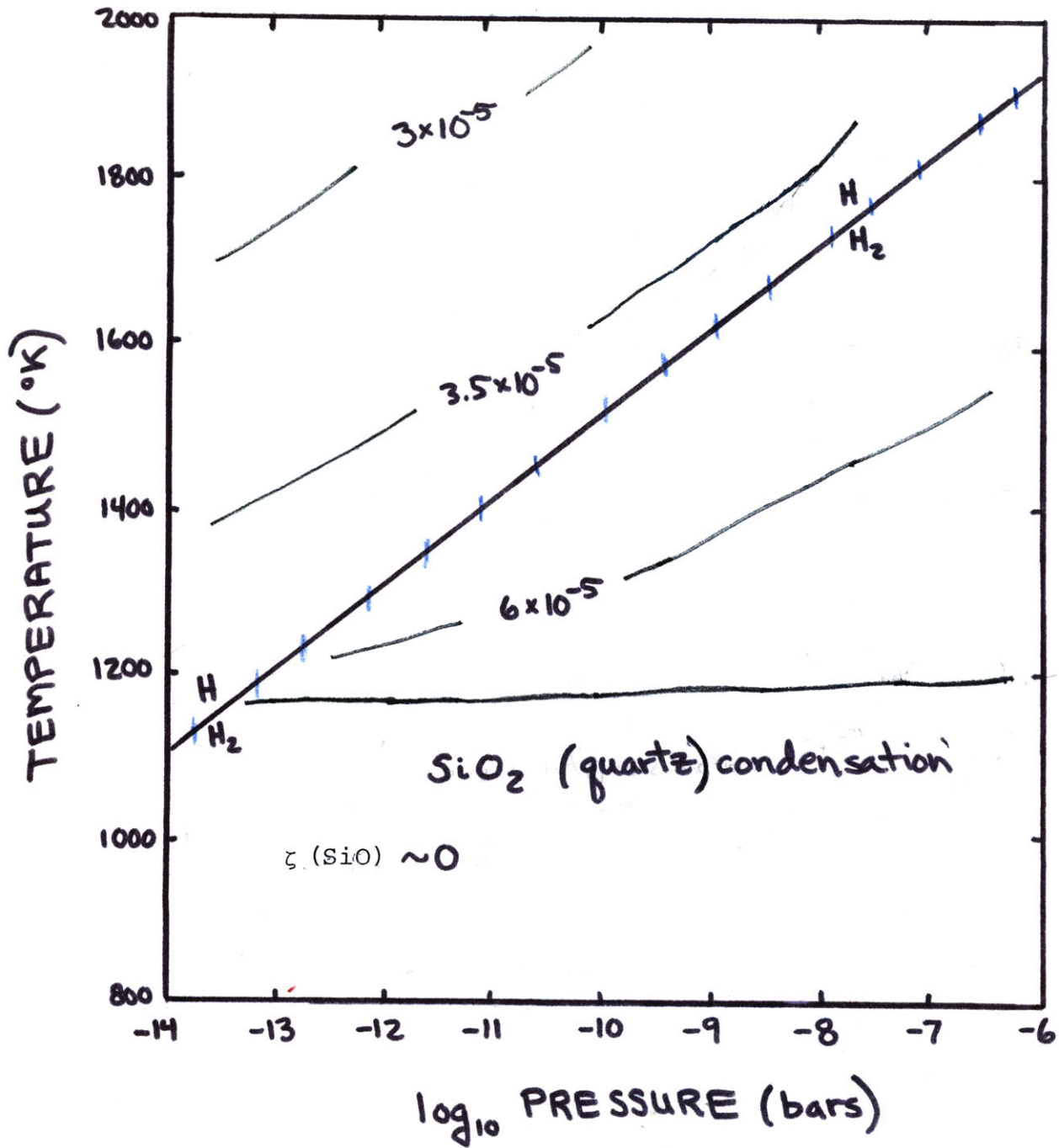


Figure 4.2 As in Figure 4.1, but for SiO instead of H₂O.

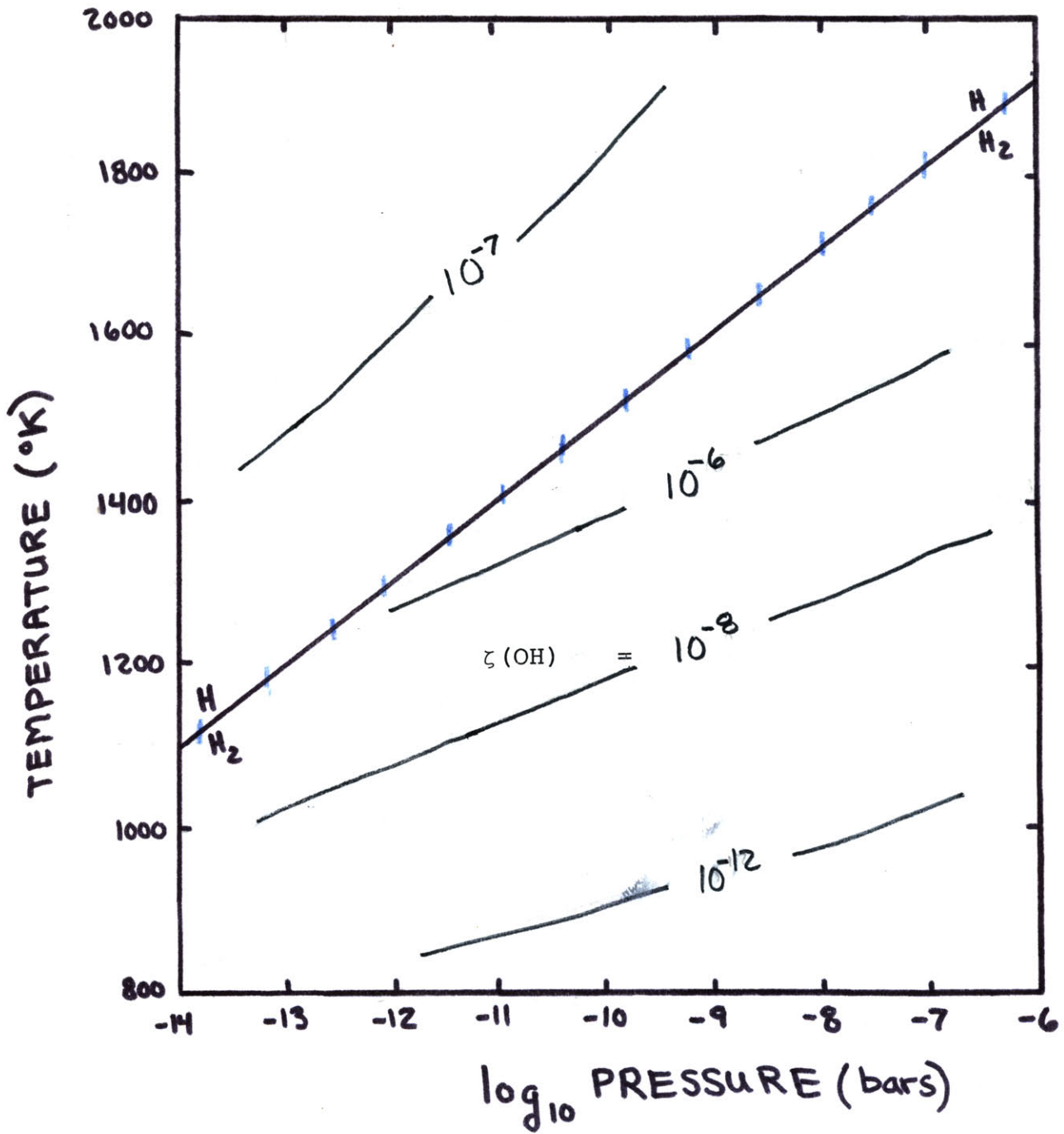


Figure 4.3 As in Figure 4.1, but for OH instead of H₂O.

1972); and (3) the H₂O transition has been well studied in the laboratory (Bluyssen, Dymanus, and Verhoeven, 1967; Kukolich, 1969). Before beginning the description of the experimental observing program in Chapter 5, we will first review the H₂O rotational transition in more detail in the following Section.

4.4 The H₂O 6₁₆ → 5₂₃ Maser Transition*

Due to the interaction between \underline{J} and the total nuclear angular-momentum \underline{I} (for the two hydrogens $I = \frac{1}{2} + \frac{1}{2} = 1$) each H₂O rotational level is hyperfine split into three (2I+1) F levels, where $\underline{F} = \underline{J} + \underline{I}$. The resultant hyperfine structure of the H₂O 6₁₆ → 5₂₃ rotational transition as determined in the laboratory (Kukolich, 1969) is summarized in Table 4.1 and illustrated in Figure 4.4. The spectrum of the spontaneous emission from the transition calculated for conditions of local thermodynamic equilibrium (LTE) for a distant

* In the spectroscopic notation $J_{K_1 K_2}$, designating an asymmetric top rotational level, K_1 and K_2 are the projections of \underline{J} , the total molecular angular momentum, along a symmetry axis of the molecule for the cases of the limiting prolate and the limiting oblate symmetric tops.

Table 4.1
Hyperfine Components of the $6_{16} \rightarrow 5_{23}$
 H_2O Rotational Transition

	<u>F</u>	<u>ν^* (kHz)</u>	<u>Relative Intensity[†]</u>
$\Delta F = -1$	7 \rightarrow 6	- 35.86 \pm .05	.385
	6 \rightarrow 5	- 2.79 \pm .05	.324
	5 \rightarrow 4	40.51 \pm .05	.273
$\Delta F = 0$	6 \rightarrow 6	173.2 \pm 2	.009
	5 \rightarrow 5	217.9 \pm 2	.009
$\Delta F = +1$	5 \rightarrow 6	394	.00006

* Frequency relative to 22.23507985 GHz (frequency of the intensity-weighted mean)

[†] In local thermodynamic equilibrium (LTE) ; values from Townes and Schawlow, 1955.

Values for the $\Delta F = +1$ transition from Sullivan (1971).

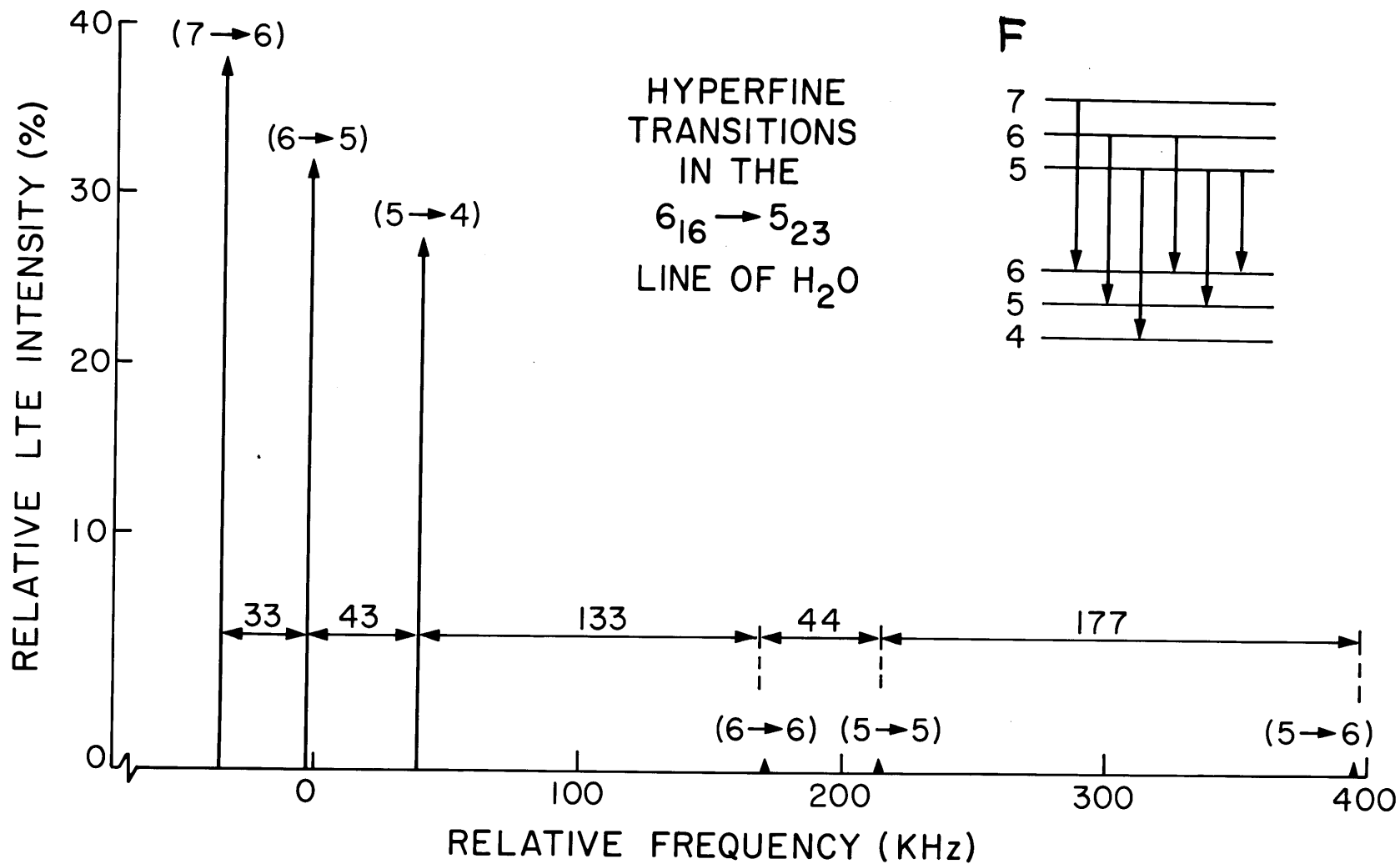


Figure 4.4 The hyperfine components of the $6_{16} \rightarrow 5_{23}$ rotational transition of H_2O . Data from Kukolich (1969).

cloud of H₂O gas at various kinetic temperatures (10, 100, 1000°K) is shown in Figure 4.5. For each hyperfine component j, the molecular thermal velocity distribution in the radial (z) direction is of the form

$$f_j(v_z) = a_j \exp\left[-\frac{m_{\text{H}_2\text{O}} v_z^2}{2kT}\right]$$

The first order Doppler shift $v - v_j \equiv \Delta v = -\frac{v_o v_z}{c}$ may be introduced to determine the corresponding frequency distribution

$$f_j(v) = a_j \exp\left[-\frac{(\Delta v)^2}{2\sigma_j^2}\right]$$

where

$$\sigma_j = \frac{1}{\lambda_o} \sqrt{\frac{kT}{m_{\text{H}_2\text{O}}}}$$

and where v is an observed frequency, v_o is the mean of the hyperfine frequencies, and $\lambda_o \equiv c/v_o$. The full width

at half power (fwhp) of f_j equals $2.3548 \sigma_j$. The spectrum for the transition is obtained here by superposing the individual spectra of the three hyperfine lines for which $\Delta F = -1$. Computational details are contained in Appendix B.

Because the energy spacings between the hyperfine levels in H₂O are so small with respect to the energies of the relevant molecular rotational levels, the assumption of an LTE population distribution appears valid for almost any excitation mechanism. None of the pumping mechanisms yet proposed for the H₂O maser [infrared (Litvak, 1973); ultraviolet (Oka, 1973); collisional (de Jong, 1974)] are capable of selective population of hyperfine levels. This is unlike the case of OH (e.g., Gwinn et al., 1975).

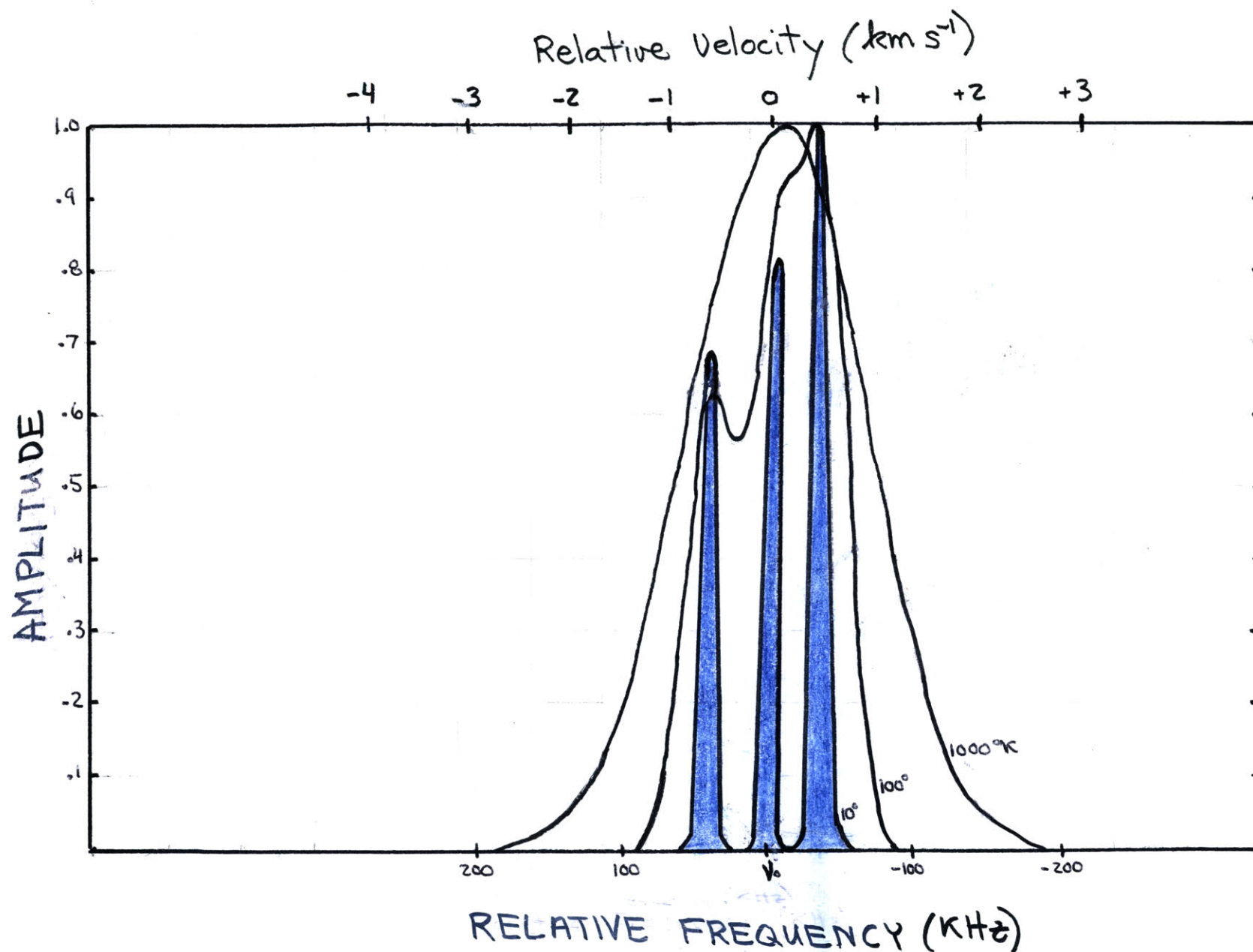


Figure 4.5 The spectral appearance of the spontaneous emission from the $\text{H}_2\text{O } 6_{16} \rightarrow 5_{23}$ rotational transition computed for kinetic temperatures of 10°, 100°, and 1000°K. $\nu_0 = 22.23507985$ GHz. A radial velocity of 1 km s^{-1} corresponds to a frequency shift of -74.1 kHz.

CHAPTER 5

RADIO OBSERVATIONS OF H₂O MASERS

5.1 VLBI Observations and Analysis

The high signal-to-noise ratio that can be obtained in observations of H₂O maser sources may be exploited to make extremely accurate determinations of the relative angular positions of emission features in a given source, and to examine the emission spectra of individual features at high spectral resolution. Measurements of relative angular positions over time will yield the relative transverse velocities of neighboring maser regions. Analysis of the spectra of individual emission features yields information about the physical conditions as well as the radial velocities characteristic of these regions.

With these goals in mind we selectively analyzed some of the VLBI observations made in 1970 June, 1971 February, and 1971 March, with antennas at the following radio observatories: Haystack Observatory, Tyngsboro, Massachusetts; Naval Research Laboratory, Maryland Point, Maryland; and National Radio Astronomy Observatory, Green Bank, West Virginia and Tucson, Arizona (Johnston et al., 1971; Moran et al., 1973; and Reisz et al., 1973). In these observations the incoming signal* at each observatory was mixed with the outputs of stable frequency sources (local oscillators) and the resulting video signal was clipped, sampled, and digitally recorded on magnetic tape, using the Mark I recording system (Bare et al., 1967).

* All observations were conducted with horizontal (E) linear polarization, referenced to Haystack Observatory.

Each VLBI observation consisted of ~150 seconds of data recorded "on source", followed by ~30 seconds of "off source" calibration data. The local oscillators were set such that the total output frequency equalled the minimum frequency in the desired band, ν_{\min} , plus the a priori Doppler shift of ν_{\min} introduced by the sidereal rotation and orbital revolution of the earth at the start time of an observation. In the processing of each tape-pair, the bit strings from two observatories were aligned (geometric delay removed) and cross-correlated; the cross-correlation was then corrected for clipping (Van Vleck and Middleton, 1966), Hanning weighted, and Fourier transformed to yield the complex cross-spectrum in discrete form (e.g. Moran, 1976):

$$S[\nu_{\min} + (k-1)\Delta\nu] = \sum_{m=1}^M \sin\left\{\frac{\pi}{2} \sum_{\ell=1}^L X_1[(\ell-1)\Delta t] X_2[(\ell-1)\Delta t + (m-1)\Delta t] H[(m-1)\Delta t] \right\} \exp[2\pi i (m-1)\Delta t (k-1)\Delta\nu] \quad (5.1)$$

where X_1 and X_2 are the clipped, sampled, and aligned forms of the video signals from two observatories; $\Delta t = (7.2 \times 10^5)^{-1} \text{ s}$ is set by the Mark I system; $2\Delta\nu = 2(M\Delta t)^{-1}$ = spectral resolution; $H[(m-1)\Delta t] = \frac{1}{2}[1 + \cos(m-1)\pi M^{-1}]$ is the Hanning weighting function; L = number of bits in each processed sample = 1.44×10^3 ; M = number of delays in cross-correlation = number of spectral channels in transform; and k , ℓ , and m are the respective indices of frequency, time, and delay. To allow coherent

processing of the cross-spectra over the duration of each observation (~150 s), the fringe phase corresponding to the frequency channel that contained the spectral maximum of the most intense feature was used as a reference for fringe-phase rotation.

5.1.1 Accurate Relative Positions of H₂O Emission Features

To determine accurately the angular position of a particular feature with respect to the reference feature, we must determine both the relative fringe rate and the relative phase for each observation. For these purposes, M in Equation (5.1) was chosen as 36, providing a spectral resolution of about 40 kHz. To determine the fringe rate with respect to that of the reference (first time derivative of the relative fringe phase), the cross-spectra were integrated over the duration of each observation with the relative phase corresponding to each spectral channel counter rotated by $(t-t_{ij})\dot{\Delta\phi}_{\text{trial}}$ where t_{ij} is the start time of the j^{th} observation on the i^{th} baseline and $\dot{\Delta\phi}_{\text{trial}}$ is a trial value for the relative fringe rate. The value of $\dot{\Delta\phi}_{\text{trial}}$ that yielded the maximum fringe amplitude for the feature of interest upon integration was chosen as the relative fringe rate, $\dot{\Delta\phi}(t_{ij})$. The relative phase, $\Delta\phi(t_{ij})$, of the feature referred to t_{ij} , was then taken to be the arithmetic mean of the relative phases determined about once each second over the observation, each counterrotated by the appropriate $(t-t_{ij})\dot{\Delta\phi}(t_{ij})$. Such estimates of relative phase are ambiguous in the sense that they represent the relative phase modulo $2\pi n$ radians (n being some integer). Estimates of relative fringe rates alone, however, may be combined to yield unique maps of the relative positions of emission features (Moran, 1968; Moran et al.,

1973). An example of such a map for H₂O masers in W3(OH), associated with the optical H_{II} nebula IC 1795, is shown in Figure 5.1. The source W3(OH) was selected for our purposes here because all five features were within about 2 arcseconds, and also within the 360 kHz observing bandwidth.

By statistically combining estimates of relative fringe rates and relative fringe phases, unambiguous determinations of relative positions can be made which are about two orders of magnitude more accurate than estimates that may be obtained from the relative fringe rates alone. A method devised for obtaining accurate estimates of relative position may be described as follows (Reisz et al., 1973):

We consider the angular separation of a particular spectral feature at frequency ν from a reference feature at frequency ν_0 in the relative coordinates $\Delta\alpha$ in right ascension and $\Delta\delta$ in declination. Assuming the errors in the relative fringe rates to be independent random variables distributed in a Gaussian manner, we obtain, from these data alone, the joint probability density for the separation:

$$p_0(\Delta\alpha, \Delta\delta) = \frac{1}{2\pi |\underline{\mu}|^{1/2}} \exp\left(-\frac{1}{2} \underline{\chi} \underline{\mu}^{-1} \underline{\chi}^T\right) \quad (5.2)$$

where the row vector $\underline{\chi}$ has the two components $\Delta\alpha - \Delta\alpha^*$, $\Delta\delta - \Delta\delta^*$; $|\underline{\mu}|$ is the determinant of the covariance matrix $\underline{\mu}$; T denotes transpose; and $(\Delta\alpha^*, \Delta\delta^*)$ is the maximum-likelihood estimate of the features' separation obtained from analysis of the relative fringe-rate data. The covariance matrix $\underline{\mu}$ contains the uncertainties in, and the correlation between, the es-

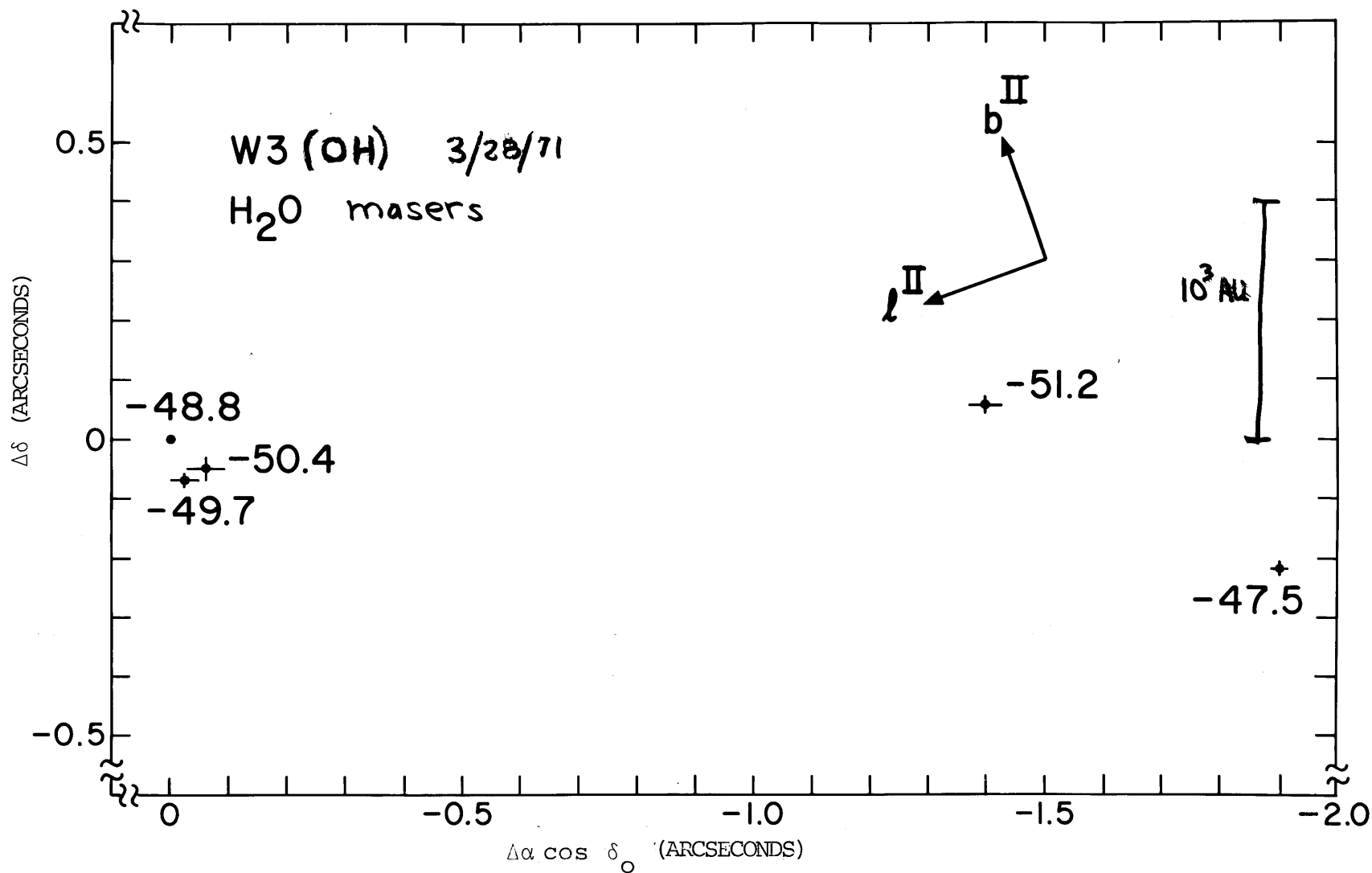


Figure 5.1 Radio interferometer map of H₂O emission features associated with the optical nebula IC 1795. Masers are labeled by their radial velocity (km/sec). l II and b II are Galactic longitude and latitude (IAU 1958). Reproduced from Moran et al. (1973).

estimates $\Delta\alpha^*$ and $\Delta\delta^*$.

The estimates of the relative fringe phases are ambiguous in the sense that they represent the relative phases, modulo $2\pi n$ radians (n some integer). An instantaneous determination of relative fringe phase for a particular baseline and source may be represented as

$$\Delta\phi(t) = \Phi(\Delta\alpha, \Delta\delta; t) + \epsilon + 2\pi n \quad (5.3)$$

in the strong signal case, where ϵ ($\ll 2\pi$) is the error in the (ambiguous) phase determination, and the functional form of Φ is given by

$$\Phi(\Delta\alpha, \Delta\delta; t) \sim \frac{2\pi\nu}{c} [B(t) \cdot \hat{s}(\alpha_0 + \Delta\alpha, \delta_0 + \Delta\delta) - B(t) \cdot \hat{s}(\alpha_0, \delta_0)] \quad (5.4)$$

where α_0, δ_0 are the coordinates of the reference feature. These coordinates and B are generally known well enough to allow us to neglect their uncertainties when estimating relative angular positions. Since clock-synchronization errors and the effects of the propagation medium on the relative fringe phase cancel almost completely, they contribute negligibly to ϵ , leaving (thermal) receiver noise as the primary source of error and justifying our modeling of ϵ as additive Gaussian noise.

If we consider that Equation (5.2) provides the joint a priori probability density of $\Delta\alpha$ and $\Delta\delta$ and that all values of the integer n in Equation (5.3) are equally probable, we may write the conditional probability density for $\Delta\alpha$ and $\Delta\delta$,

given the set of independent relative fringe-phase estimates $\Delta\phi(t_{ij})$, as

$$p(\Delta\alpha, \Delta\delta | \underline{\Delta\phi}) \propto p_0(\Delta\alpha, \Delta\delta) \times \prod_{i=1}^I \prod_{j=1}^{J_i} \sum_{n=-\infty}^{\infty} \frac{1}{\sigma_{ij}} \exp\{-[\Delta\phi(t_{ij}) - 2\pi n - \Phi(\Delta\alpha, \Delta\delta; t_{ij})]^2 / 2\sigma_{ij}^2\} \quad (5.5)$$

where σ_{ij} is the standard deviation of the relative fringe phase from the j^{th} of J_i observations on the i^{th} of I independent baselines.

We take as our final estimate of the relative angular position of the feature the value of $(\Delta\alpha, \Delta\delta)$ for which the conditional probability is a maximum. This estimate of relative position can be found quickly for "reasonable" data sets by systematic evaluation of p over successively finer two-dimensional grids in the $(\Delta\alpha, \Delta\delta)$ -plane. Because of the slow variation of p_0 with a change in either $\Delta\alpha$ or $\Delta\delta$, compared to the corresponding change in the other factors in p , the presence of p_0 serves primarily to delimit the area of search for the maximum of p . By the same token, the estimate determined by the above algorithm will not differ significantly from the maximum-likelihood estimate of the relative position.

The information content of the interferometer observations is illustrated in Figure 5.2 for the location of the -47.5 km s^{-1} feature shown in Figure 5.1, relative to the -48.8 km s^{-1} reference feature.

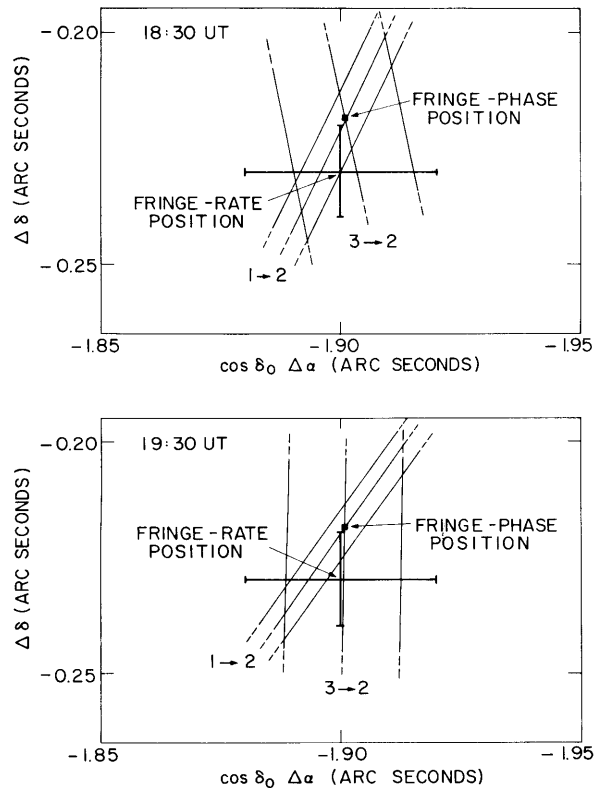


Figure 5.2 Lines of constant relative fringe phase $\Delta\phi(t_{ij}) \pm 2\pi n$ for the -47.5 km s^{-1} feature relative to the -48.8 km s^{-1} reference feature for the Haystack-NRAO (1 → 2) and the NRL-NRAO (3 → 2) baselines at 18:30 and 19:30 UT on 1971 March 28. Lines are shown for each baseline for three consecutive values of n (see text) in the vicinity of the feature position determined from analysis of relative fringe-phase and fringe-rate data. Also shown is the feature position determined from analysis of relative fringe-rate data alone.

Combination of the information from eleven* observations of W3(OH) on three interferometer baselines (Table 5.1) yields the relative positions presented in Table 5.2. Figure 5.3 illustrates the accuracy of these determinations by displaying the contours of constant probability density for the relative location of the -47.5 km s^{-1} feature.

Observations using cryogenic (low system temperature) receivers on the longest earth-based interferometer baselines should allow the accuracy of such determinations to be improved to $\sim 10^{-5}$ arc second, sufficient to determine within one year transverse velocities of 1 km s^{-1} between features at the 2.5 kpc distance of W3(OH).

5.1.2 Spectra of Individual H₂O Emission Features

Selected interferometer observations were also processed to examine the spectra of individual H₂O emission features. For this purpose, M in Equation (5.1) was chosen as 360, equivalent to a frequency resolution of about 4 kHz, and the most intense features were examined. This value of M, and hence the frequency resolution, was selected to ensure that individual H₂O hyperfine components would be fully resolved. Because features that are spatially removed from the feature of interest appear at different fringe rates, integration of the cross-spectra over an observation allows the effects of these spatially distinct features to be removed. The spatial discrimination provided by interferometric observations is an important advantage of such observations over those conducted using a single radio

* Eight of the eleven observations are statistically independent. The information gained from the required phase closure on three baselines simultaneously is equivalent to that from the observation on the third baseline, but contains statistically dependent noise.

Table 5.1

Fringe Phases and Rates of H₂O Emission Features in W3(OH) on 1971 March 28
Relative to -48.8 km s⁻¹ Reference Feature

Start Time of Observation (UT)	Baseline*	-47.5 km s ⁻¹	Feature†	-50.4 km s ⁻¹	Feature†	-51.2 km s ⁻¹	Feature†
		Fringe Phase (deg)	Fringe Rate (mHz)	Fringe Phase (deg)	Fringe Rate (mHz)	Fringe Phase (deg)	Fringe Rate (mHz)
18:00	1 → 2	-129± 5	- 0.9 ±.2	110± 8	0.2 ± .2	170± 5	- 4.4 ±.2
18:30		- 17±12	- 5.8	81±10	-0.2	51± 6	- 8.0
19:00		67± 5	- 10.6	53±10	0.0	- 132± 6	- 11.3
19:30		- 78± 5	- 15.4	48± 7	0.2	127± 5	- 14.4
18:30	1 → 3	- 67± 7	- 9.5	- 25± 7	0.0	- 170± 7	- 9.5
19:00		- 50±10	- 12.2	- 94±10	0.1	- 170±10	- 12.0
19:30		- 14± 7	- 16.5	-130± 6	-0.1	- 140± 7	- 13.5
20:00		123± 7	- 19.0	170±12	0.0	75± 7	- 15.2
18:30	3 → 2	23± 6	3.7	87± 7	0.0	- 145± 5	1.9
19:00		92±11	2.2	120± 7	0.1	30± 7	0.3
19:30		- 54± 5	0.7	175± 7	0.2	- 95± 6	- 1.1

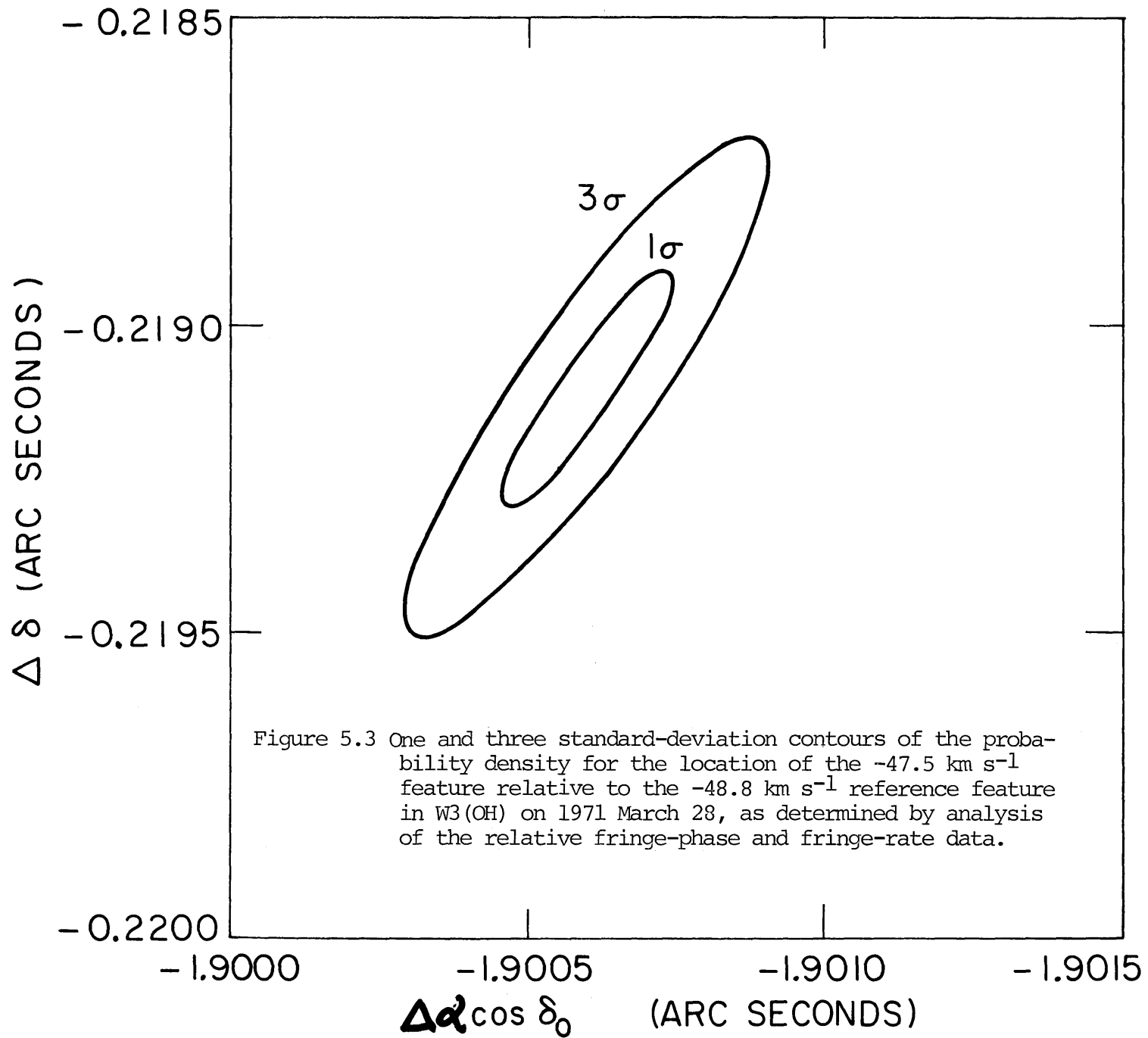
* Station 1 was the Haystack Observatory's 120-foot-diameter antenna, Tyngsboro, Massachusetts; Station 2, the National Radio Astronomy Observatory's 140-foot-diameter antenna, Green Bank, West Virginia; and Station 3, the Naval Research Laboratory's 85-foot-diameter antenna, Maryland Point, Maryland.

† Features are labeled by their radial velocity relative to the local standard of rest. The -49.7 km s⁻¹ feature shown in Figure 5.1 has been omitted, as its relative phase could not be reliably determined. This resulted because the spectrum of this feature was overlapped by that of the -48.8 reference, the effects of which could not be removed due to their near spatial coincidence.

Table 5.2
Relative Positions of H₂O Emission Features
in W3(OH) on 1971 March 28

<u>Feature* (km s⁻¹)</u>	<u>$\Delta\delta$ (arcsec)</u>	<u>$\Delta\alpha \cos\delta$ (arcsec)</u>	<u>arc length (arcsec)</u>
-47.5	-0.2191±0.0003	-1.9006±0.0002	1.9132
-48.8	0.0	0.0	
-50.4	-0.0050±0.0003	-0.0174±0.0002	0.0181
-51.2	0.0731±0.0003	-1.3563±0.0002	1.3583

* Denoted by radial velocity of feature relative to the local standard of rest (LSR).



antenna. Spectra of the -1.8 km s^{-1} feature in W49 N obtained in this way are shown in Figures 5.4 and 5.5. In these figures, the lack of variation of the fringe phase across the spectrum of the feature is indicative of spatial coincidence to within 0.0001 arc seconds, and the maximum fringe amplitude (which, as shown, has been normalized to unity) is equivalent to reception of $S(\nu) \sim 4 \times 10^4 \text{ Jy}$ ($1 \text{ Jy} \equiv 10^{-26} \text{ Wm}^{-2} \text{ Hz}^{-1}$). In Figure 5.6 the spectrum of the 9.5 km s^{-1} feature in Orion A is shown, normalized to $6 \times 10^3 \text{ Jy}$.

The spectra shown in Figures 5.4, 5.5, and 5.6 have been fitted with model profiles consisting of multiple, complex, Gaussian components by minimizing the sum of the squares of the amplitudes of the residuals over the spectra. The iterative minimization technique used is described by Fletcher and Powell (1963) and is based upon a method devised by Davidon (1959)*.

For the H_2O spectral features examined, a two-component model was found to be required because of asymmetries in the spectral profiles, and to be sufficient to reduce the residuals to almost the noise level. When all eight parameters (amplitude, center frequency, width, and phase of each component) were allowed to vary, the frequency separations obtained were within a few kilohertz of the 33.07 kHz spacing between the $F = 7 \rightarrow 6$ and

* See Appendix A .

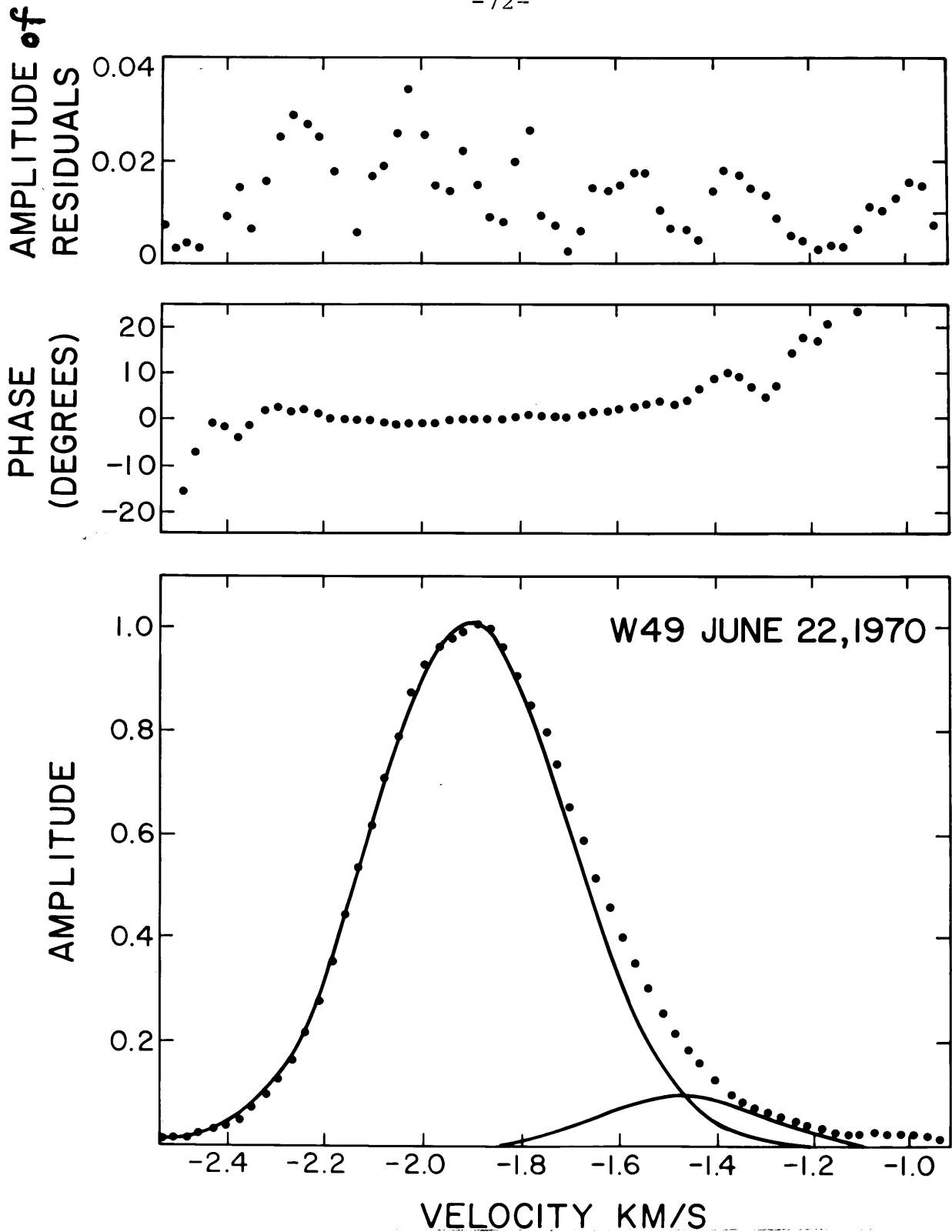


Figure 5.4 Radio interferometric spectrum of the -1.8 km s^{-1} H_2O feature in W 49 (optically obscured). The peak amplitude, shown normalized to unity, is equivalent to $\sim 4 \times 10^4 \text{ Jy}$. Velocity is with respect to the local standard of rest.

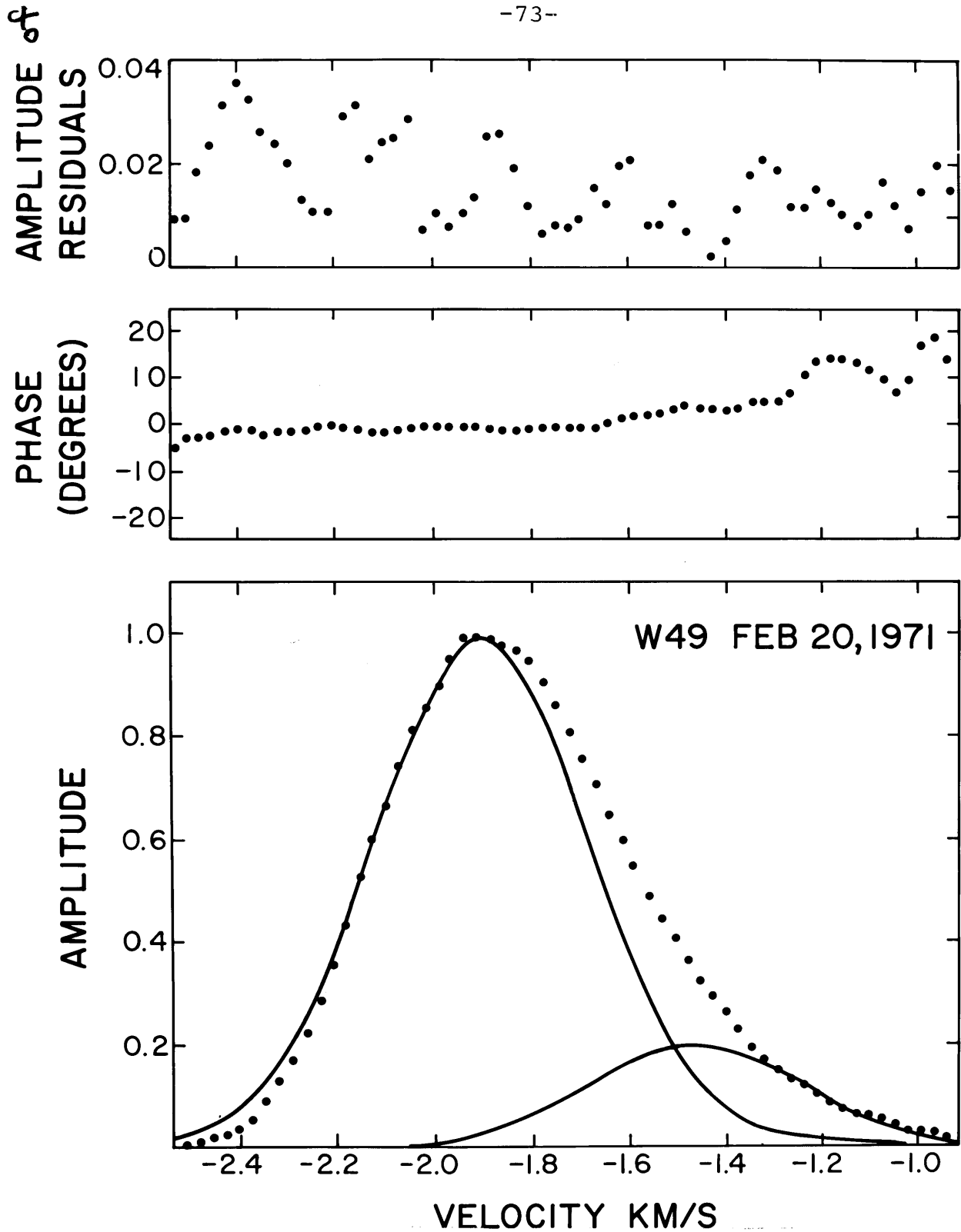


Figure 5.5 Radio interferometric spectrum of the -1.8 km s^{-1} H_2O feature in W 49 (optically obscured). The peak amplitude, shown normalized to unity, is equivalent to $\sim 4 \times 10^4 \text{ Jy}$. Velocity shown is relative to the local standard of rest.

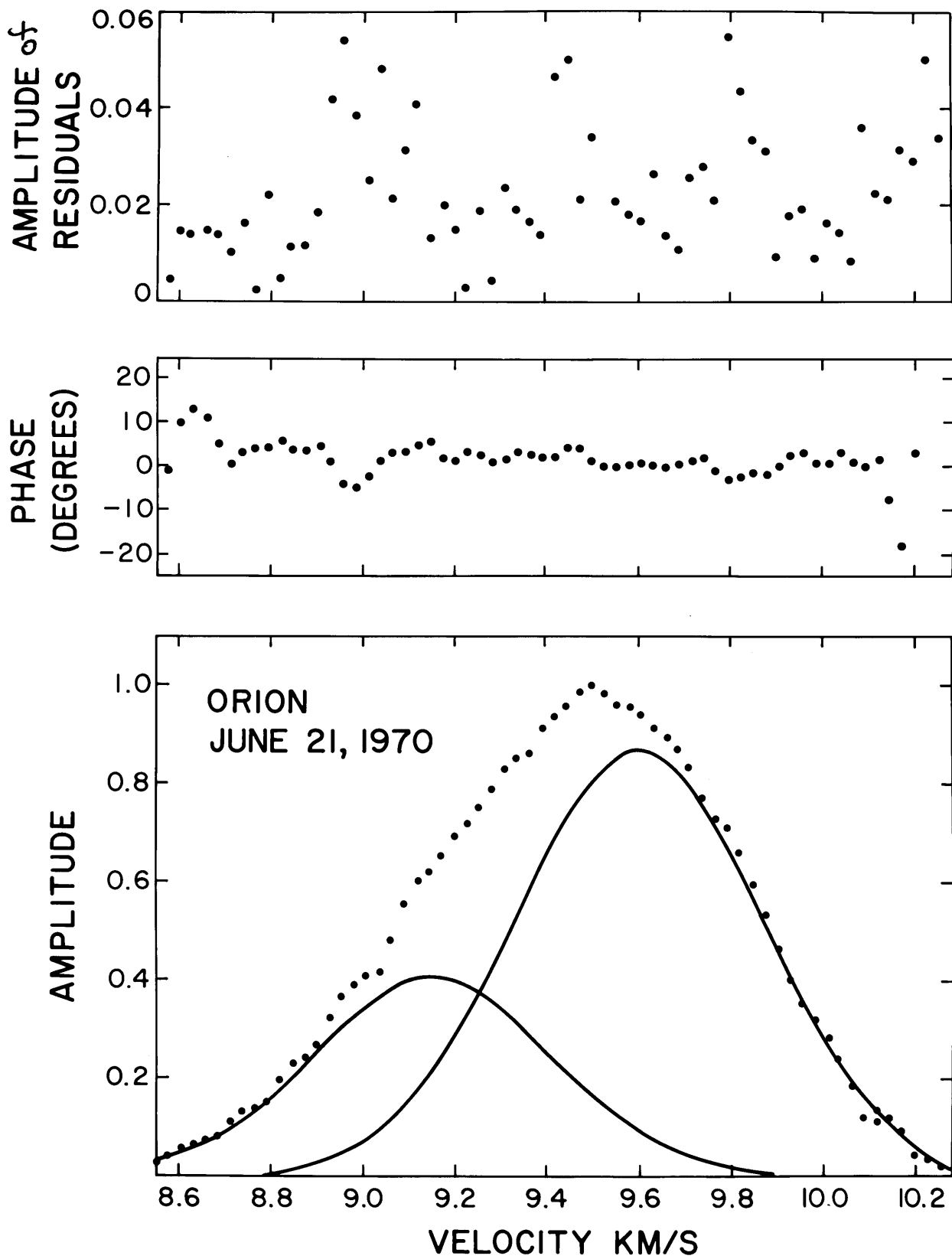


Figure 5.6 Radio interferometric spectrum of the 9.5 km s^{-1} H_2O feature in Orion A. Amplitude has been normalized to $\sim 6 \times 10^3 \text{ Jy}$. Velocity is with respect to the local standard of rest.

$F = 6 \rightarrow 5$ hyperfine components. The differences were not significant in view of the comparably large uncertainties in the estimates of the separations. For the solutions shown in the figures, the separation of components was constrained to equal this hyperfine separation. The results of Gaussian decompositions of H_2O maser spectra carried out in this manner are given in Table 5.3.

From this table and the preceding figures it is evident that the spectra exhibited by the H_2O maser emission features examined thus far are much narrower than those of an LTE spectrum (see Figure 4.5). We also note that the change in radial velocity (-0.04 km s^{-1}) which this model yields for the -1.8 km s^{-1} feature in W49 N from 1970 June to 1971 February is significantly less than the $\sim 1 \text{ km s}^{-1}$ velocity variations over comparable time periods previously attributed to H_2O features (e.g., Sullivan, 1971). The large velocity variations obtained in such previous studies are dynamically unrealistic, and likely resulted from the inability to resolve individual maser features which appeared spectrally superposed (Sullivan, 1973).

5.2 Single Antenna Observations Using a Cryogenic Receiver

As it became evident that the spectra exhibited by H_2O masers departed significantly from an LTE appearance, interest grew in systematically studying these spectra at increased resolution. The observational portion of such a study was facilitated in 1973 September when the Haystack Observatory began operating at Ku-Band using a liquid helium-cooled maser receiver (Yngvesson et al., 1975). Use of this cryogenic

Table 5.3

Double Gaussian Decomposition of Selected H₂O Spectra

Source Feature Date	Amplitudes*	ν_j (kHz) [†]	σ_j (kHz) [§]	Phase Differ. (degrees)	rms scatter of Ampl. about mean	LTE Ampl. Ratio//	Obs. Ampl. Ratio //
W49 N, -1.8 km s ⁻¹ 1970 June	0.09 ±0.01 1.013±0.001	103.76 136.83±0.02	12.3±.4 14.8±.1	10±8	0.016	1.19	0.09 ±
W49 N, -1.8 km s ⁻¹ 1971 February	0.20 ±0.01 0.988±0.001	106.75 139.82±0.04	16.2±.2 16.3±.1	8±6	0.019	1.19	0.20 ±
Orion A, 9.5 km s ⁻¹ 1970 June	0.87 ±0.01 0.41 ±0.01	-691.57 -668.50±0.03	19.8±.1 19.3±.3	3±1	0.026	1.19	2.1 ±

* Peak observed amplitude is set equal to 1.

† With respect to $\nu=22.23507985$ GHz; velocity with respect to local standard of rest = 0. The difference in center frequencies is constrained to be 33.07 kHz. The absolute frequency accuracy of these observations is ~1 Hz.

§ Full width at half power (fwhp) $\equiv 2.3548 \sigma_j$. In terms of an "equivalent temperature",

$$T_j = \frac{\sigma_j^2 \lambda^2 m_{\text{H}_2\text{O}}}{k} \sim 160^\circ\text{K for } \sigma_j = 20 \text{ kHz.}$$

// Ratio of the amplitude of the F = 7→6 to that of the F = 6→5 hyperfine component.

receiver resulted in a decrease in the system temperature of almost an order of magnitude, compared to that available during the VLBI observations discussed in the previous section (Section 5.1).

Beginning in 1973 September and continuing at a bimonthly average rate for about one year, systematic observations of H_2O sources associated with Galactic H_{II} regions were conducted at Haystack utilizing the cryogenic receiver* under the cooperative observing program designated Moran-3 by the Haystack Observatory. In similar fashion to the VLBI observations discussed in Section 5.1, each single antenna observation consists of recording alternate segments of "on source" and "off source" data. A set of ~2500 observations, which were initiated at Haystack upon the discovery of interstellar H_2O masers in 1969 and which continued through March 1970, was made available to the author by the experimenter, M. L. Meeks, prior to the Moran-3 observations. At the time of the Meeks observations the system temperature achievable at Haystack Observatory was an order of magnitude higher than that during the VLBI observations discussed in Section 5.1. The Meeks observations proved of great assistance in planning the Moran-3 observations, and in expediting their initial computer processing.

For each source on each observing session in the Moran-3 program, a series of observations was conducted consisting of both "wide" bandwidth (6.67 MHz, or 2.0 MHz) and "narrow" bandwidth

* A series of such receivers was actually required because of unexpected design problems. Redesign and construction of additional cryogenic receivers at the Haystack Observatory was directed by S. Zisk.

(667 kHz, and/or 200 kHz) recordings covering the emission spectra of all major features. Here we use "wide" and "narrow" to distinguish respectively bandwidths for which individual H₂O maser "features" are unresolved, or are fully resolved. Table 5.4 contains the primary sources observed during the Moran-3 program, whereas Table 5.5 contains the observing dates of the program. A portion of the computer-generated reference log for the observations is reproduced in Table 5.6, illustrating a typical sequence of observations. As in the VLBI observations, the Moran-3 observations used horizontal linear polarization. When scheduled observing time was sufficient, observations with orthogonal polarization were also obtained; at regular intervals, calibrating observations of standard continuum sources (Jupiter, Venus) were also conducted.

In these single antenna observations, the incoming radio signal is mixed down to a video band, clipped, and sampled, as in the case of the interferometer observations discussed in Section 5.1. In the single antenna case, however, the resultant bit string is auto-correlated using a one hundred channel digital correlator (Weinreb, 1963), and the results of "on-source" and "off-source" auto-correlations are recorded on magnetic tape (Conant and Meeks, 1968). The recording requirements of this process in terms of magnetic tape are about one thousand times less than that of Mark I interferometer observations. Thus, the more than one thousand separate single antenna observations conducted under the Moran-3 program could be condensed onto a single magnetic tape. The compressed observations of the Meeks and Moran-3 programs reside in archival storage at the Haystack Observatory.

Table 5.4

H₂O Sources Associated with Galactic H_{II} Regions

<u>Source</u>	<u>Kinematic Distance*</u>	<u>Velocity (LSR)</u>	<u>α(1950.0)</u>	<u>δ(1950.0)</u>
1) Orion A	0.5 kpc	8±20 km s ⁻¹	5 ^h 32 ^m 46 ^s .8	- 5° 24' 18"
2) W3 (OH)	2.5	-49±15	2 23 16.8	61 38 54
3) W3C	2.5	-40±15	2 21 55.	61 51 59
4) W49N	15	2±100	19 07 49.9	9 1 18
5) M17	2.1	12±15	18 17 28.8	-16 15 52

* From Mezger and Höglund (1967).

Table 5.5

Moran-3 Observing Schedule (Haystack Observatory)

<u>Dates</u>	<u>Sources Observed*</u>
4, 5, 6 June 1973 [†]	1, 2, 4
7, 8, 9 September 1973	1, 2, 4
18, 19 November 1973	1, 2, 4, 5
4, 5 December 1973	2, 4, 5
22 December 1973	1, 2
14, 15, 16 March 1974	1, 2, 3, 4, 5
3, 4 July 1974	1, 2, 3, 4

* Numbers refer to those assigned in Table 5.4.

[†] Cryogenic receiver not yet operable.

Table 5.6

Reference Log of Moran-3 Observations

<u>STARTSIG</u> UT Time	<u>MODE</u>	<u>DURATION</u> (MIN)	<u>BW (KHz)</u>	<u>FLSR</u> (kHz)	<u>LORF*</u> (kHz)	<u>T ANT</u> (°K)	<u>DEL TANT</u> (°K)	<u>TSYS</u> (°K)	<u>TRES</u> (°K)	<u>IOBS †</u>
7 ^h 49 ^m 54 ^s	OFF/ON	3.05/ 3.05	6667.	0	41916.09440	18.4	2.4	137.6	0	2924
7 59 32	OFF/ON	3.05/ 3.05	667.	0	41916.09440	28.9	2.4	135.7	.125	2925
8 8 18	OFF/ON	3.05/ 3.05	667.	667.0	41917.36490	13.3	2.4	135.7	.125	2926
8 18 6	OFF/ON	3.05/ 3.05	667.	- 667.0	41914.82390	115.2	2.8	135.7	.250	2927
8 28 18	OFF/ON	3.05/ 3.05	667.	- 1334.0	41913.55340	17.5	2.5	135.7	.125	2928
8 38 26	OFF/ON	3.05/ 3.05	6667.	0	41916.09440	17.0	2.5	135.7	0	2929

MORAN-3

12/22/1973 (356) ORION-A

* Local oscillator frequency setting. $LORF = \frac{\nu_{sky} - 22750.}{525}$ kHz.

† Sequential numbering of observations. IOBS = 2927 corresponds to the observation shown in Figure 5.8.

During the compression (recopying) process, the CDC-3300 computer at the Haystack Observatory was induced to read tapes originally written on the Observatory's U-490 computer, to code and reference them for convenient access, and to record the stacked observations in IBM compatible format for eventual processing by IBM 360 and IBM 370 computers at M.I.T.

The initial processing of observations at M.I.T. included converting the auto-correlations to power spectra*, and computing the velocity (frequency) axis of the observed spectra referenced to the solar system barycenter at the mid time of the "on source" segment of each observation (Ash, 1972), with an instantaneous accuracy of about 1 cm s^{-1} (1 Hz) . Performing these calculations at M.I.T. avoided the effects of several "bugs" in the Haystack software, and permitted increased accuracy in the computations of spectral profiles and their associated frequency axes. Approximately 15% of the Moran-3 observations were processed at M.I.T. during the course of this investigation. Prior to processing observations at M.I.T., the entire Moran-3 program was reviewed on the CRT display at Haystack. This review confirmed the time variability of H_2O spectra, and the usually $\lesssim 10\%$ polarization which had been noted by investigators dating from the initial discovery of H_2O masers.

Selected examples of H_2O spectra obtained during the series of single antenna observations at Haystack[†] utilizing the

* Because of the symmetric nature of auto-correlation, the use of one hundred delays is equivalent to $M = 200$ in Equation (5.1) with $X_2 = X_1$, and Δt determined by the choice of bandwidth.

† We also include one from the Reisz-1 program conducted at the Haystack Observatory following the Moran-3 observations described in Table 5.5.

cryogenic receiver are presented in Figures 5.7, 5.8, 5.9a, 5.10, and 5.11. As in our previous analysis of VLBI spectra in Section 5.1, parameters describing (the least possible) multiple Gaussian components were estimated from least squares fits to spectra.* Results from the decompositions of the single antenna spectra presented in Figures 5.8 to 5.11 are displayed in Figure 5.12. From this figure we note that about 50% of the individual H₂O spectra exhibit widths ($\sigma_j \sim 20$ KHz) comparable to those of the VLBI spectra presented in Section 5.1. There is evidence from time variations that at least some of the "features" which are apparently broader may actually be composed of spectra from several superposed individual features. In no case where distinct spectral features could be definitively identified from one observing session to the next (e.g., feature 6 in Figures 5.8 and 5.9a) could any variation greater than $\sim 0.1 \text{ km s}^{-1}$ in apparent radial velocity be attributed. The velocity resolution here has been found limited to $\sim 0.05 \text{ km s}^{-1}$ by the spectral superposition inherent to the single antenna observations. The time variations observed for H₂O spectra are due primarily to amplitude variations of individual features which appear superposed.

From the residuals displayed in Figure 5.9b, it is evident that we can discern systematic departures of H₂O maser spectral profiles from those of superposed Gaussians. Because of insufficient signal to noise ratio, a similar decomposition of OH single antenna spectra by Rönnäng (1972) was unable to uncover

* See Appendix A.

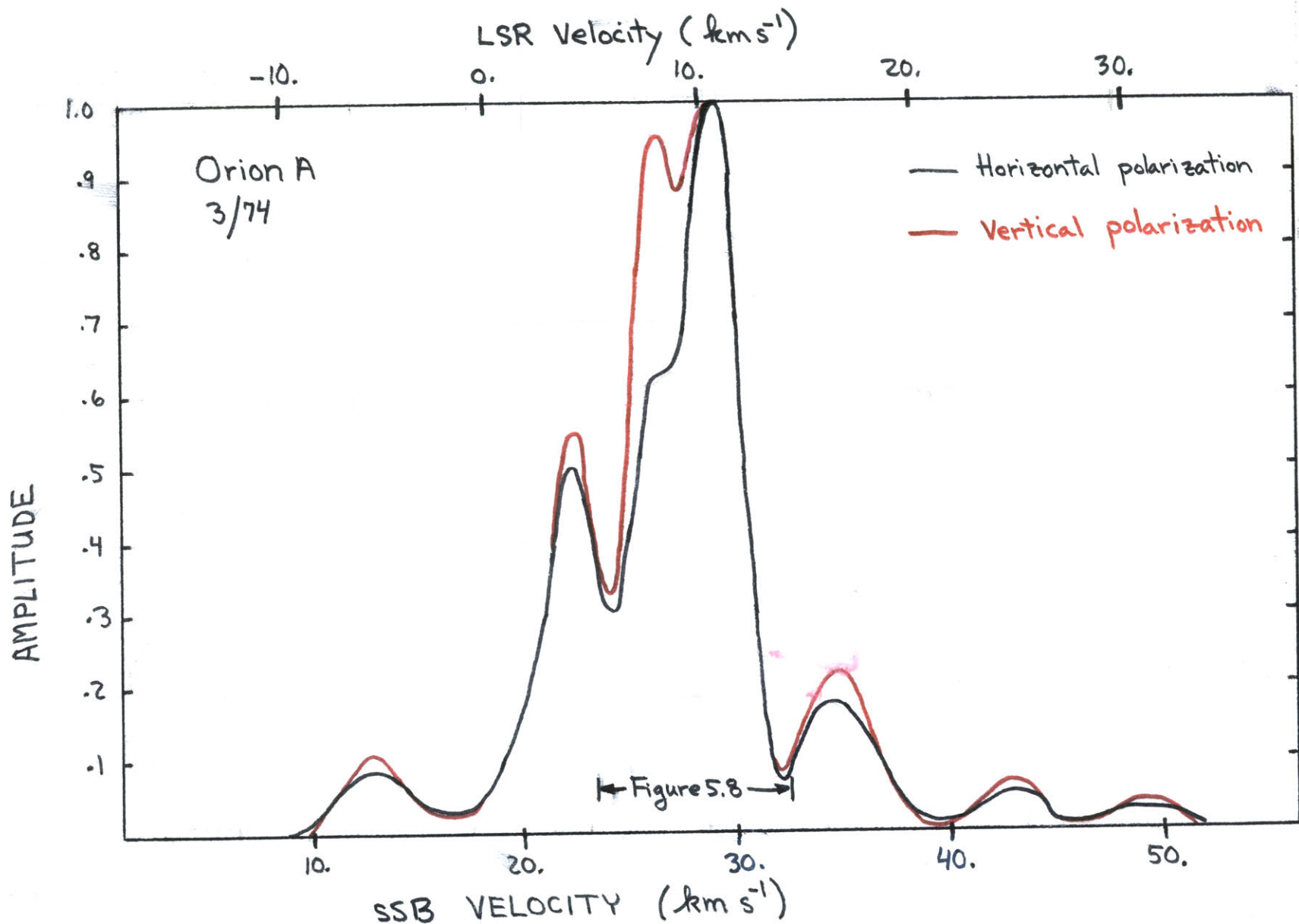


Figure 5.7 The entire H_2O (22.235 GHz) spectrum of Orion A at horizontal, and vertical, linear polarization. The lower velocity scale shown is with respect to the solar system barycenter (SSB); the upper velocity scale is with respect to the local standard of rest (LSR), and has been obtained by subtracting 18.16 km s^{-1} from the lower scale. Unit amplitude corresponds to $\sim 2 \times 10^3 \text{ Jy}$. The portion of this spectrum around 8 km s^{-1} (LSR) exhibits the greatest polarization observed for any source during any of the observing sessions.

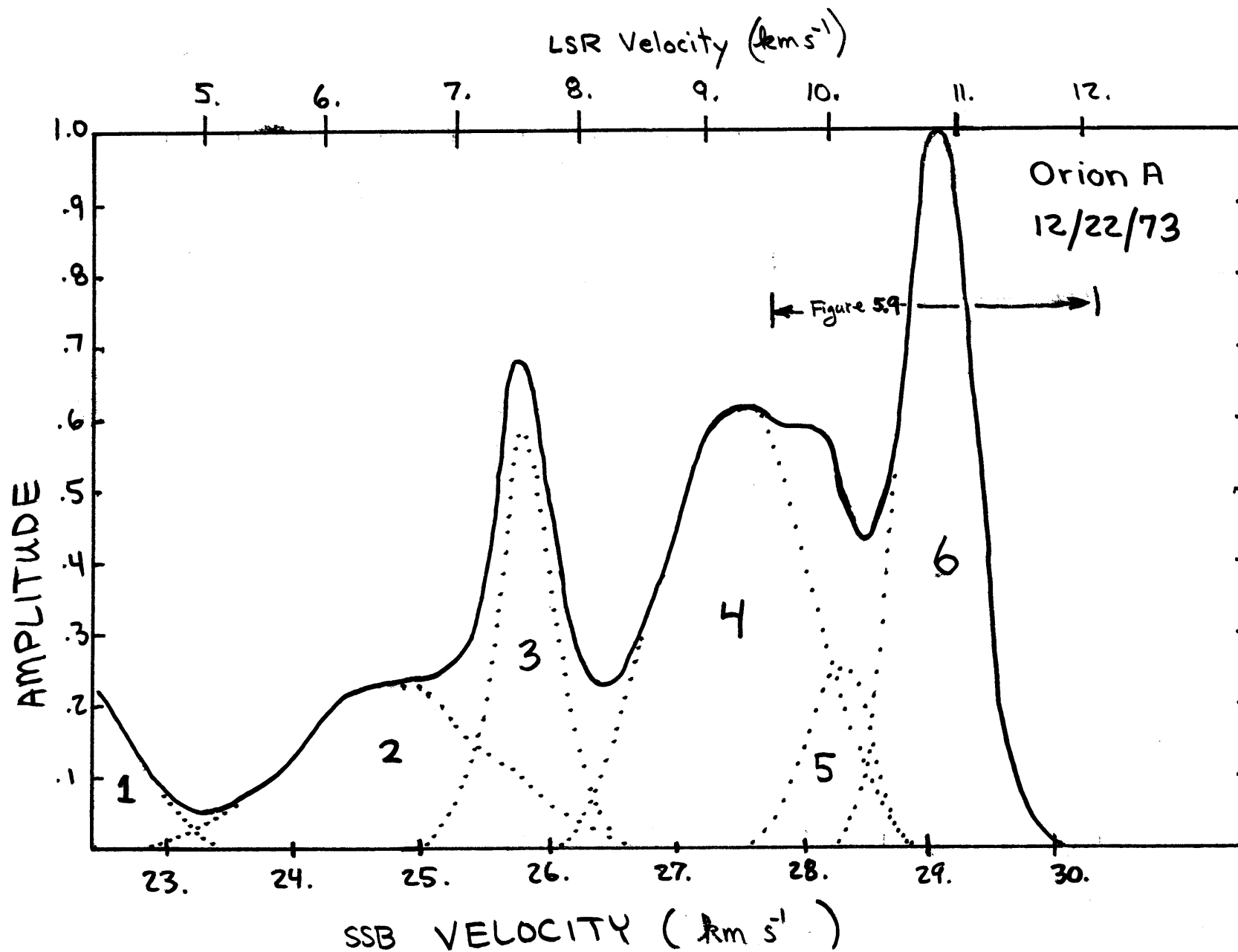


Figure 5.8 667 kHz bandwidth spectrum of Orion A. Lower velocity scale is with respect to SSB, upper with respect to LSR. Unit amplitude corresponds to $\sim 2 \times 10^3$ Jy. Numbers refer to Gaussian components (indicated by dots) of model spectrum (solid) which is indistinguishable from observed spectrum.

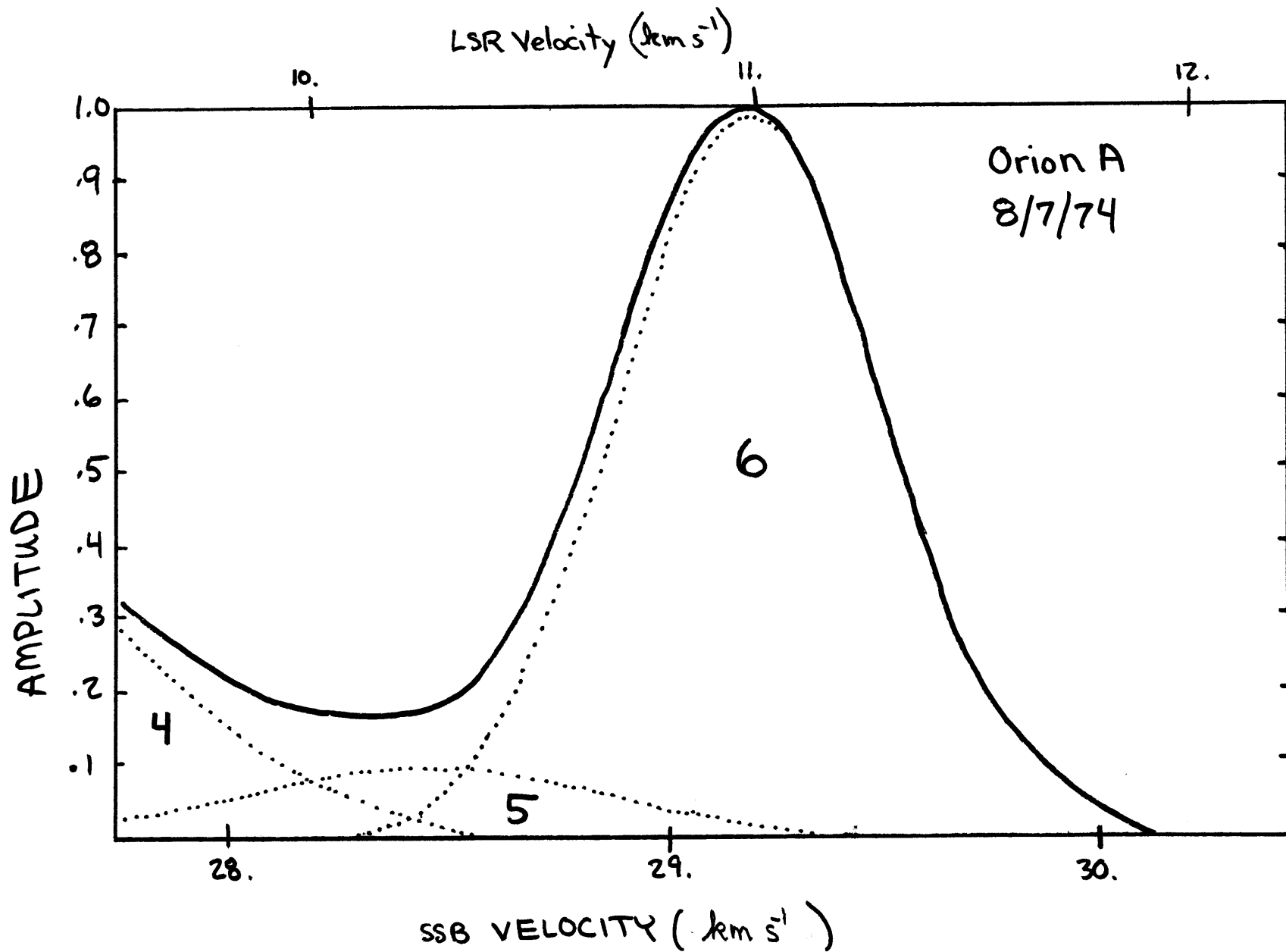


Figure 5.9a 200 kHz bandwidth spectrum of Orion A. Numbering of Gaussian model components corresponds to Figure 5.8. Unit amplitude corresponds to 2×10^3 Jy. This observation was conducted during the Reisz-1 program at the Haystack Observatory.

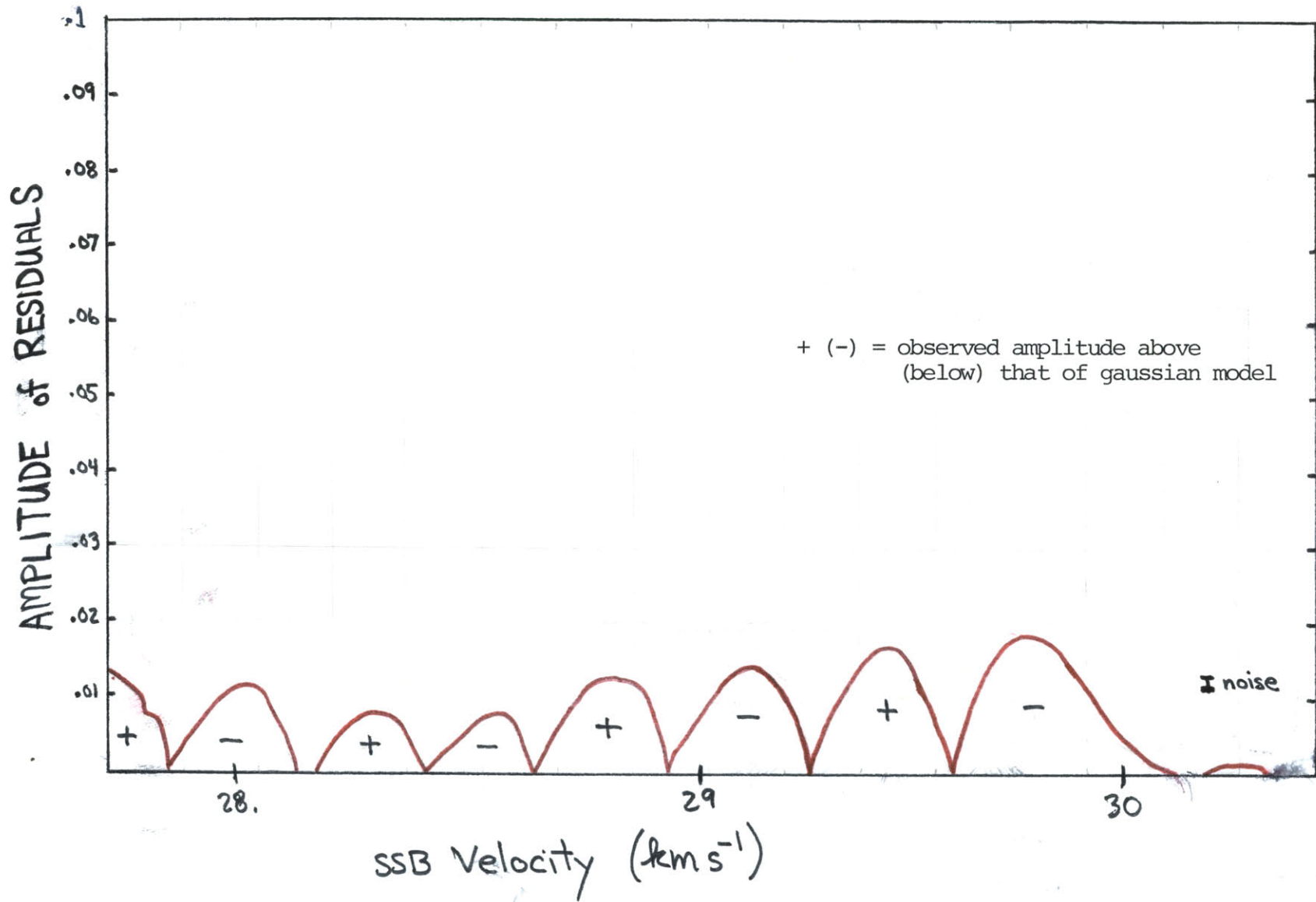


Figure 5.9 b Magnitudes of the differences between the observed spectrum shown in Figure 5.9a and the superposition of the Gaussian model components.

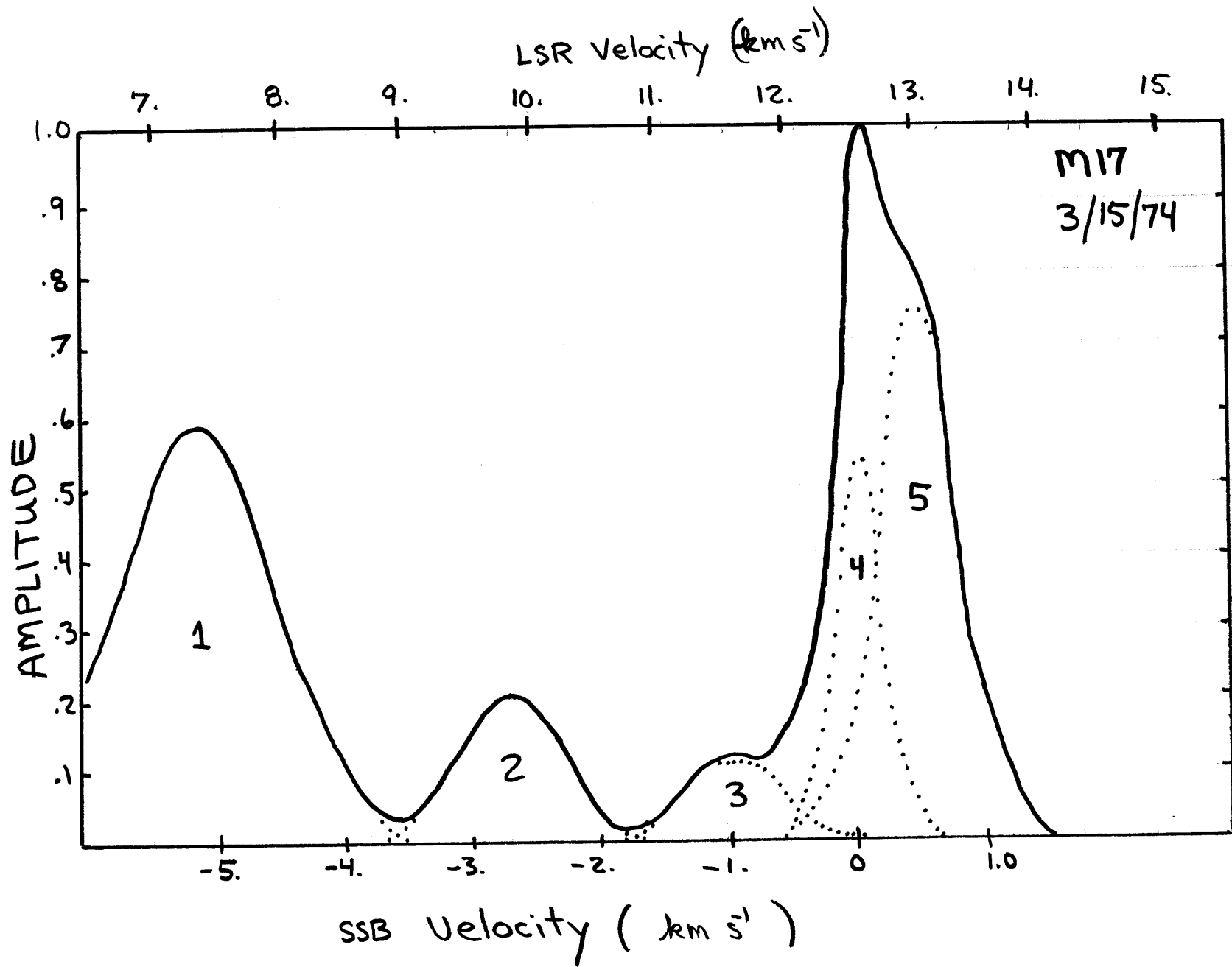


Figure 5.10 667 kHz spectrum of M17. Unit amplitude corresponds to $\sim 2 \times 10^2$ Jy. The upper velocity scale is with respect to LSR, and has been obtained from the lower scale by adding 13.52 km s^{-1} .

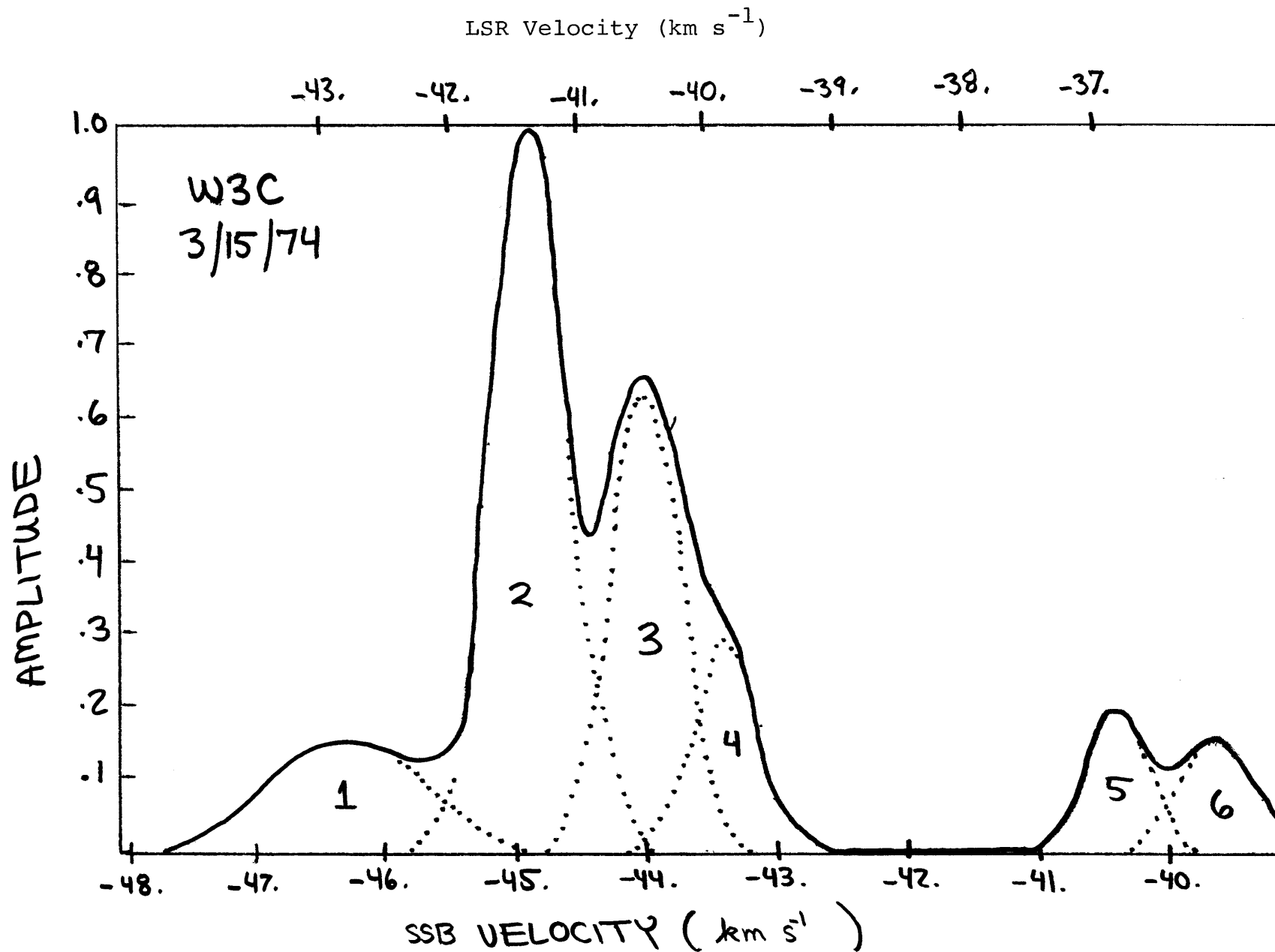


Figure 5.11 667 kHz spectrum of W3C. Unit amplitude corresponds to 1×10^3 Jy. The upper (LSR) velocity scale was obtained by adding 3.62 km s^{-1} to the lower (SSB) velocity scale.

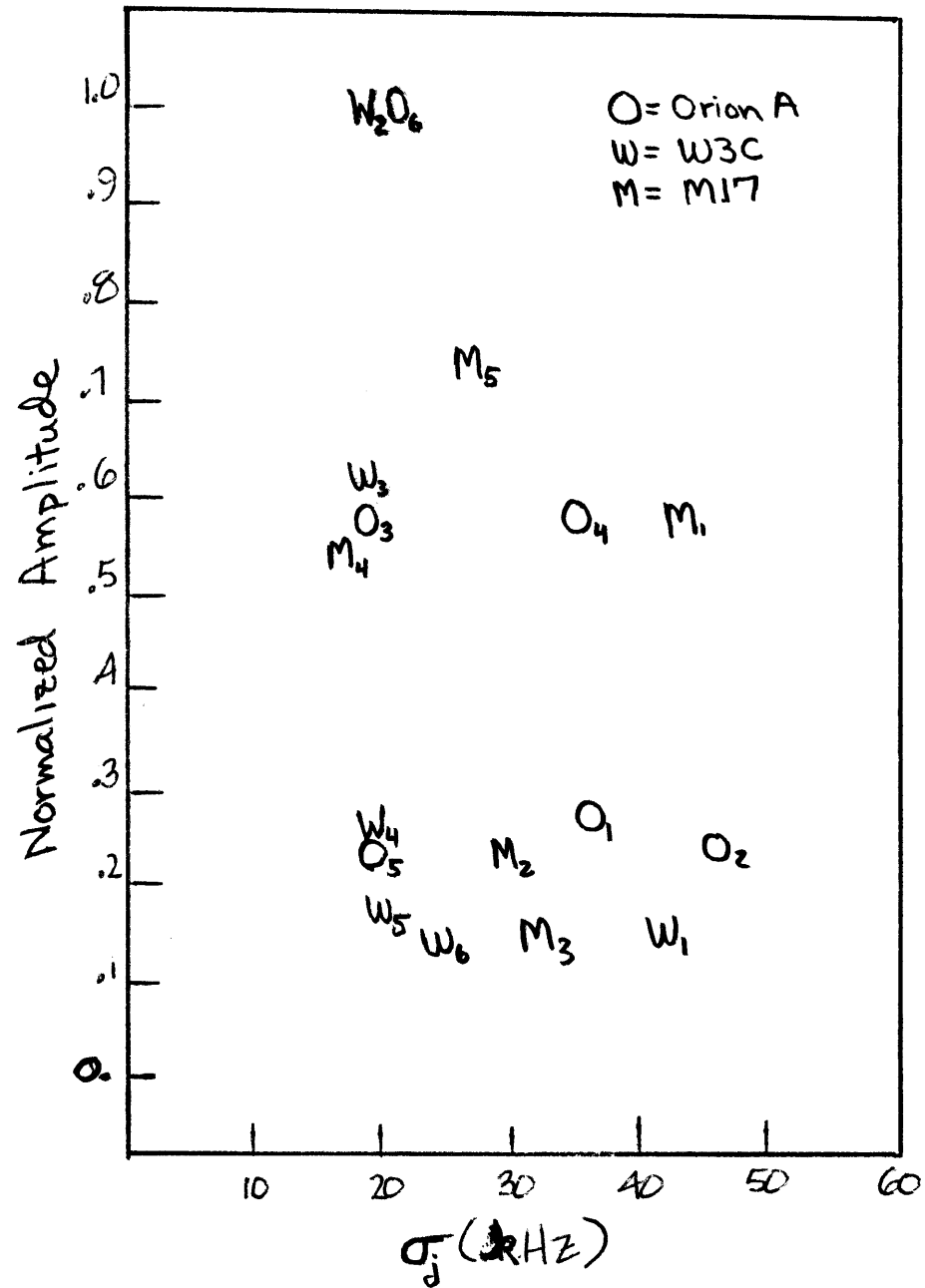


Figure 5.12 Results of the Gaussian decompositions of the H₂O spectra shown in Figures 5.8 to 5.11. The subscripted numbering of individual spectral features corresponds to that in the respective figures.

any deviation of the observed spectra from model spectra consisting of superposed Gaussian emission features.

To interpret the individual H₂O maser spectral profiles further, we next inquire into the radiative processes in the "masing" regions.

CHAPTER 6

MODELING AN ASTROPHYSICAL MASER

6.1 The Equations of Radiative Transfer

Just prior to the turn of this century Max Planck, by theoretically equating the electromagnetic emission and absorption of slightly damped linear oscillators, had determined the equilibrium energy density in a cavity at temperature T to be

$$u(\nu, T) = \frac{8\pi\nu^2}{c^3} U(\nu, T) \quad \text{J m}^{-3} \text{Hz}^{-1} \quad (6.1)$$

where $U(\nu, T)$ represented the mean energy of the oscillators.

In June 1900 Lord Rayleigh, making use of the equipartition theorem, replaced U in Planck's formula with kT (k now being Boltzmann's constant). Because of a correction Jeans made to Rayleigh's derivation, the classical equation for the electromagnetic radiation intensity inside a cavity

$$I(\nu) = c u(\nu, T) = \frac{8\pi kT}{\lambda^2} \quad \text{Wm}^{-2} \text{Hz}^{-1} \quad (6.2)$$

is generally known as the Rayleigh-Jeans radiation law. It was the inability of this classical radiation equation to explain experimental results at high frequencies (e.g. the absence of an "ultraviolet catastrophe") which led to the original postulates of quanta.

By considering an ensemble of oscillators which could assume only integer multiples of the energy unit $h\nu$ (h now being

Planck's constant) and by assuming the probability of an oscillator being in a given energy level $E = nh\nu$ to be proportional to the Boltzmann factor $\exp[-nh\nu/kT]$, Planck found that kT should be replaced by $\frac{h\nu}{e^{h\nu/kT} - 1}$ and thus the quantum formula for the intensity of cavity radiation became

$$I(\nu) = \frac{8\pi h\nu}{\lambda^2 [e^{h\nu/kT} - 1]} \quad \text{Wm}^{-2} \text{Hz}^{-1} \quad (6.3)$$

which reduces to the classical Rayleigh-Jeans result [Equation (6.2)] for $kT \gg h\nu$. Equation (6.3) is derived in statistical mechanics (e.g., Morse, 1965) by treating photons as bosons with zero rest mass. Equation (6.3) may further be integrated over frequency as

$$\int I(\nu) d\nu = \frac{8\pi h}{c^2} \int_0^\infty \frac{\nu^3 d\nu}{e^{h\nu/kT} - 1} = \frac{8\pi h}{c^2} \left(\frac{kT}{h}\right)^4 \cdot \frac{\pi^4}{15} \quad (6.4)$$

since

$$\int_0^\infty \frac{x^3 dx}{e^x - 1} = \frac{\pi^4}{15}$$

Further consideration of the distribution of such radiation in direction (e.g., Dufay, 1964) shows that a puncture in the cavity surface would allow $\sigma T^4 \text{ Wm}^{-2}$ of power to escape, where $\sigma = 5.67 \times 10^{-8} \text{ Wm}^{-2} \text{ }^\circ\text{K}^{-4}$ is the Stefan-Boltzmann constant. The luminosity of a spherical black body of radius R is thus given simply by $L = 4\pi R^2 \sigma T^4 \text{ W}$.

In 1917 Einstein postulated that the rate equations governing the populations of two (non degenerate) energy levels would be

$$\begin{aligned} R_{u\ell} &\equiv R_{u \rightarrow \ell} = N_u A_{u\ell} + N_u I(\nu) B_{u\ell} \\ R_{\ell u} &\equiv R_{\ell \rightarrow u} = N_\ell B_{\ell u} I(\nu) \end{aligned} \quad (6.5)$$

where N_u and N_ℓ are the number densities in the upper (higher

energy) and lower levels, $A_{u\ell}$ is the probability per second that a molecule (or atom) in the upper level will spontaneously emit a photon and go to the lower level, $I(\nu)B_{u\ell}$ is the corresponding probability per second of stimulated emission for a molecule in the upper level exposed to radiation of intensity $I(\nu)$, and $I(\nu)B_{\ell u}$ is the corresponding probability per second of absorption for a molecule in the lower state exposed to radiation of intensity $I(\nu)$. For thermal equilibrium $\frac{N_u}{N_\ell} = e^{-\frac{h\nu}{kT}}$, where $h\nu = E_u - E_\ell$. Since the principle of detailed balancing states that $R_{u\ell} = R_{\ell u}$, it follows that

$$\frac{N_u}{N_\ell} [A_{u\ell} + I(\nu)B_{u\ell}] = B_{\ell u}I(\nu)$$

which leads to

$$I(\nu) = \frac{A_{u\ell}}{B_{\ell u}e^{h\nu/kT} - B_{u\ell}} \quad \text{Wm}^{-2} \text{ Hz}^{-1} \quad (6.6)$$

By comparing Equation (6.6) with Planck's equation [Equation (6.3)], Einstein deduced that

$$B_{\ell u} = B_{u\ell}$$

and

$$\frac{A_{u\ell}}{B_{u\ell}} = \frac{8\pi h\nu}{\lambda^2} \quad \text{Wm}^{-2} \text{ Hz}^{-1}$$

For energy levels which are degenerate, the relation between the stimulated emission and absorption coefficients must be modified as (e.g., Chandrasekhar,

1960): $B_{\ell u} = \left(\frac{g_u}{g_\ell}\right)B_{u\ell}$, where g denotes degeneracy.

Since our interests in this investigation concern conditions existing in astrophysical molecular masers, we must consider departures from the

equilibrium values of N_u and N_ℓ , and the distribution of velocities of the molecules that occupy these levels. From the rate equations [Equations (6.5)], we can construct the equation of radiative transfer in a maser medium (e.g., Goldreich and Keeley, 1972):

$$\begin{aligned} \frac{dI_\nu}{dz} &= \frac{h\nu}{4\pi} \phi(\nu) [R_{u\ell} - R_{\ell u}] \\ &= \frac{h\nu}{4\pi} \phi(\nu) [N_u A_{u\ell} + (N_u - \frac{g_u}{g_\ell} N_\ell) B_{u\ell} I(\nu)] \end{aligned} \quad (6.7)$$

where z is the coordinate in the direction toward the observer, where the specific intensity, I_ν ($\text{Wm}^{-2} \text{Hz}^{-1} \text{ster}^{-1}$), is assumed isotropic for simplicity and is therefore related to $I(\nu)$ by

$$I(\nu) = \int I_\nu d\Omega = 4\pi I_\nu$$

and where the quantity $\phi(\nu)$ is the probability per Hertz that a molecule undergoing a transition emits (or absorbs) a photon whose frequency is ν in the observer's frame. We assume that this probability is independent of whether the transition is from the upper level to the lower level (emission) or vice versa (absorption). We further assume that $\phi(\nu)$ is proportional to the power spectrum for the thermally broadened microwave line produced by the $6_{16} \rightarrow 5_{23}$ rotational transition in H_2O molecules. We include the effects of hyperfine splitting in this spectrum as in Figure 4.5, since we also assume that

the factor following $\phi(v)$ in Equation 6.7 is independent of hyperfine level. To account for a possible "bias" velocity of the H_2O molecules with respect to the observer's frame, and to allow this velocity to depend on the coordinate z , we replace $\phi(v)$ in Equation (6.7) by

$$\phi(v, z) = \phi\left(v - \frac{v_z(z)}{c} v\right)$$

where $v_z(z)$ is the radial component of the velocity as a function of z and introduces the indicated first order Doppler shift.

Since the rate equations [Equations (6.5)], and thus the level populations N_u and N_ℓ as discussed above, are valid only in thermodynamic equilibrium, we now modify these equations by including in a schematic, macroscopic manner, the additional effects of (i) a pumping mechanism* which effectively transfers molecules from the lower level to the upper level (or vice versa) with a probability $W_{\ell u}^P s^{-1}$ (or $W_{u\ell}^D s^{-1}$); (ii) a collisional mechanism which causes transitions between the levels with probabilities $W_{\ell u}^C s^{-1}$ and $W_{u\ell}^C s^{-1}$; and (iii) the microwave transition probabilities $W_{\ell u}^m s^{-1}$ for absorption and $W_{u\ell}^m s^{-1}$ for emission. Since the difference in energy between the upper (6_{16}) and lower (5_{23}) H_2O energy levels is extremely small compared to the energy of either level, we may make the approxi-

* For our purposes the details of this mechanism are unimportant; the interested reader is referred to Litvak (1973), de Jong (1974), and Oka (1973) for discussions of possible pump mechanisms.

mation $W_{u\ell}^C \approx W_{\ell u}^C \equiv W^C$. For I_ν isotropic, $W_{u\ell}^m = B_{u\ell} I(\nu)$. Further, since the difference between the level degeneracies of the 6_{16} and 5_{23} levels ($g_u = 39$; $g_\ell = 33$) will not play an essential role in our analysis, we set $g_u = g_\ell$ for simplicity, and thus $W_{u\ell}^m \approx W_{\ell u}^m \equiv W^m$. In terms of this model and the stated assumptions, the rate equations for a steady state may be written as (e.g., Goldreich and Keeley, 1972):

$$\begin{aligned} R_{u\ell} &= R_{\ell u} \\ [W_{u\ell}^p + W^C + W^m]N_u &= [W_{\ell u}^p + W^C + W^m]N_\ell \end{aligned} \quad (6.8)$$

Let us consider qualitatively the solution to Equation (6.7) under conditions in which W^p is independent of z , and W^C is negligible. If, in the region near the "start" of the maser at $z=z_0$, $W_{\ell u}^p - W_{u\ell}^p$ is large compared with W^m , then the pump will be able to maintain a constant differential population density between the upper and lower levels (we assume, tacitly, that the total number density of molecules in the two states, $N_u + N_\ell$, remains approximately constant -- independent of the values of W^p or W^m ; collisions would tend to maintain this quasi-constancy, although they also tend to reduce the effectiveness of the pump). If we further neglect the (small) contribution of spontaneous emission to the radiation intensity, we can approximate Equation (6.7) by

$$\begin{aligned} \frac{dI_\nu}{dz} &\approx \frac{h\nu}{4\pi} \phi(\nu, z) [N_u - N_\ell] B_{u\ell} I_\nu \\ &= \frac{c^2}{32\pi^2} \phi(\nu, z) \Delta n A_{u\ell} I_\nu \end{aligned} \quad (6.9)$$

where $\Delta n \equiv N_u - N_\ell$ is approximately constant, independent of z . The solution to Equation (6.9) is clearly an exponential: the gain of the maser, defined as $G(z) = I_\nu(z)/I_\nu(z_0)$, increases exponentially with z . In this region the maser is said to be "unsaturated".

As $I_\nu(z)$, and thus W^m , increase exponentially with z , we would expect, if the maser path is sufficiently long, to reach a situation ("saturation") in which the stimulated emissions tend to overwhelm the pump in the sense that they prevent the latter from maintaining the constant value of Δn . For this case, Equation (6.8) can be rewritten as

$$R^m = R^p$$

$$W^m [N_u - N_\ell] \approx W_{\ell u}^p N_\ell - W_{u\ell}^p N_u \approx (W_{\ell u}^p - W_{u\ell}^p) \frac{N_t}{2} \equiv R^p$$

since Δn is very small ($N_u \approx N_\ell \approx N_t/2$) and can be set to zero on (only!) the right side under these conditions. In the region of saturated maser gain, then, we may approximate Equation (6.7) by:

$$\frac{dI_\nu}{dz} \approx \frac{h\nu}{4\pi} \phi(\nu, z) (W_{\ell u}^p - W_{u\ell}^p) \frac{N_t}{2} = \frac{h\nu}{4\pi} \phi(\nu, z) R^p \quad (6.10)$$

where we again neglect the (small) contribution of spontaneous emission, and where $N_t \equiv N_u + N_\ell$ remains approximately constant -- independent of I_ν and W^p . Since the right side of Equation (6.10) is independent of I_ν , the increase in gain in this portion of the maser is approximately linear with z (provided the z dependence of ϕ , W^p , and N_t are "mild" enough).

After the increase in gain with z ceases to be exponential, as here, the maser is described as "saturated". The maser is "partially saturated" when the gain ceases to be exponential for some, but not all, frequencies.

Equations (6.7) and (6.8) can be combined with the assumption that N_t is approximately constant to yield a general equation for the z dependence of I_ν (e.g., Sullivan, 1973), valid for ϕ independent of z . In order to retain the z dependence of radial velocity, and to avoid unnecessary computation time, here we will use Equations (6.9) and (6.10), in finite difference form, to determine $I_\nu(z-z_0)$. The crossover point from unsaturated exponential growth to saturated linear growth is taken to be that value of $(z-z_0)$ for which $R^m = W^m \Delta n$, for the assumed initially constant value of Δn , first equals $(W_{lu}^p - W_{ul}^p) N_t / 2 = R^p$.

In the following section (Section 6.2) we examine numerically the emission spectra, I_ν vs. ν , for various values of $(z-z_0)$ and other parameters of model H_2O masers, using the finite difference formulations of Equations (6.9) and (6.10). To our knowledge, this represents the first effort to determine lineshape (I_ν vs. ν). Previous investigators have integrated over an assumed lineshape. The differences in the resultant values of $I_\nu(z)$, between use of these equations with $v_z(z) = 0$ and the more general one, are of no significance for our purpose. This conclusion is based on the fact that numerical experiments (see Section 6.2) show the exponential growth to be so rapid near the crossover point that conversion from exponential to linear growth would occur over a segment of the maser path length on the order of the discrete stepsize used in the numerical integrations of Equations (6.9) and (6.10).

6.2 Numerical Examination of the Spectral Emission from Model H₂O Masers

In this section we evaluate numerically the spectral emission of model astrophysical masers, using parameter values applicable to the H₂O 6₁₆ → 5₂₃ maser. In the following section (Section 6.3) such numerical models of H₂O masers are compared with the radio observations of H₂O maser spectra presented in Chapter 5.

To determine the spectral emission from a model astrophysical maser, we compute the specific intensity I_ν for a set of discrete frequencies ν_k at successive discrete steps Δz along the maser pathlength, making use of Equations (6.9) and (6.10) in finite difference form*. $\phi(\nu)$, as stated in Section 6.1, is scaled from an LTE profile consisting of the three $\Delta F = -1$ hyperfine components of the H₂O 6₁₆ → 5₂₃ rotational transition (see Figure 4.5), with its integral normalized to unity. The Einstein A coefficient appropriate to the transition is $2 \times 10^{-9} \text{ s}^{-1}$ (Townes and Schawlow, 1955). To initialize our computations we need $I_\nu(z_0)$, the specific intensity at the maser input. Because of the apparent association in location between intense H₂O masers and young H_{II} radio continuum emission regions (see Figures 3.9a to 3.11c), we assume that $I_\nu(z_0)$ is due to continuum radiation. A typical H_{II} continuum

* See Appendix B.

radio source at a typical distance of 2 kpc is observed to produce a flux density at earth of $S(\nu) \sim 5 \times 10^{-24} \text{ Wm}^{-2} \text{ Hz}^{-1}$ (500 Jy) near 22 GHz (see, for example, Figure 3.12). For a uniformly radiating sphere, the diameter of which subtends an angle of β ($\ll 1$) radians, we find (e.g., Dufay, 1964)

$$I_{\nu}(z_0) = \frac{4S(\nu)}{\pi\beta^2} \text{ Wm}^{-2} \text{ Hz}^{-1} \text{ str}^{-1}$$

For a typical compact H_{II} region at this typical distance of 2 kpc, $\beta \sim 10^2$ arcsecond (5×10^{-4} radians), and thus

$$I_{\nu}(z_0) \sim 3 \times 10^{-17} \text{ Wm}^{-2} \text{ Hz}^{-1} \text{ str}^{-1} \quad (3 \times 10^9 \text{ Jy str}^{-1})$$

This high value of specific intensity has led us to neglect the contribution of the spontaneous emission in this investigation. Because H_2O masers at this typical distance are observed interferometrically to typically subtend angles of $\sim 10^{-3}$ arcseconds, and because these masers produce a flux density at earth on the order of that of the associated continuum sources, the maser mechanism must be responsible for a gain of $\sim \left(\frac{10^2}{10^{-3}}\right)^2 = 10^{10}$, with an uncertainty of about ± 2 in the exponent. Thus, given our hypotheses regarding the specific intensity at the maser input, we must account for a gain in this range.

As our first numerical examples, we show the spectral appearance of a model H_2O maser, with $v_z(z) = 0$, in Figure 6.1 at several values of $(z-z_0)$ along the path length direction towards the earth. We note that during unsaturated gain, the spectral width of the emission continuously decreases. This result follows from inspection of Equation (6.9): Since ϕ will clearly

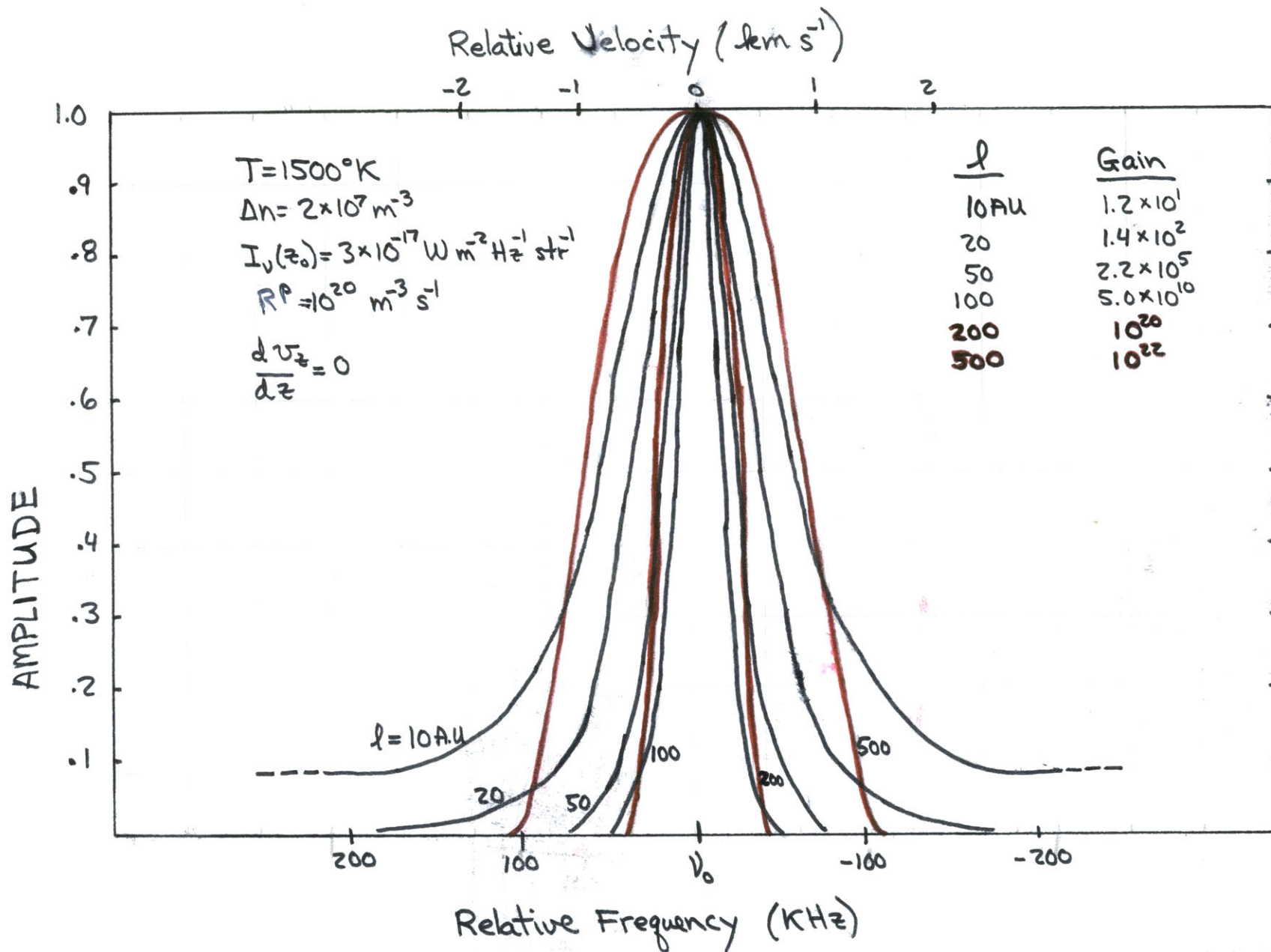


Figure 6.1 The normalized spectrum, I_ν vs. ν , of a model H_2O maser during unsaturated (black) and saturated (red) gain; $v_z(z) = 0$. Values of the parameters of the model maser are shown.

appear in the exponent of the solution, I_ν for a given value of z will be largest for that ν for which ϕ is a maximum and will be progressively much smaller for ν 's for which ϕ is smaller. As the maser begins to saturate (initially at the value of ν for which ϕ , and hence I_ν , is a maximum) the peak of the spectrum begins to flatten and to take on an appearance resembling $\phi(\nu)$ and the "wings" disappear. As we continue along the maser path towards larger values of z , the resemblance to $\phi(\nu)$ becomes closer until (if the maser path is sufficiently long) the entire feature has become fully saturated and has assumed a completely LTE appearance as in $\phi(\nu)$. For the $v_z(z) = \text{constant}$ model we find no variation in frequency of that ν for which I_ν is maximum, during either unsaturated or saturated gain -- contrary to the conjecture of Sullivan (1973). A larger effective inversion (larger Δn) produces an equivalent gain and spectral appearance over a shorter path length. A lower temperature results in a narrower spectral feature and in an increased gain for a given path length since $\phi(\nu)$ will be relatively higher at its maximum than at other values of ν and higher at its maximum than it would be at higher temperatures (see Figure 4.5). Reduced collision rates at lower temperatures would also favor higher gains since collisions would be less of an impediment to the effectiveness of the pump. An increased input intensity or an increased pump rate result in the path length prior to saturation being shorter.

As our second numerical examples, we consider model H₂O masers in which $\frac{dv_z(z)}{dz} \neq 0$. Variations of v_z with z in effect "smear" $\phi(\nu, z)$ in frequency, and therefore lead to broader spectra and reduced gain over a given pathlength. Such effects of $\frac{dv_z(z)}{dz} \neq 0$ on (unsaturated) maser emission spectra are illustrated in Figure 6.2. Linear variations of the radial velocity $v_z(z)$ along the given maser path length are seen to progressively widen the spectrum (with respect to a model in which $\frac{dv_z(z)}{dz} = 0$), to reduce the gain (see, also, Figure 6.3), to shift the frequency at which the maximum intensity of the spectrum occurs, and to introduce a slight asymmetry in the spectrum. Radial velocity variations which would differ by more than a few km s⁻¹ over the path lengths of the observed masers can be excluded, as masers with such velocity variations would not have similar enough coherence properties to produce comparable gains (see Figure 6.3). Smaller variations in $v_z(z)$ over a given maser path length favor higher gains.

6.3 Comparisons with Observed Spectra

We now return to a consideration of the radio observations of H₂O maser spectra presented in Chapter 5. Let us first consider the possibility of explaining these spectra on the basis of a fully saturated maser process with $\frac{dv_z(z)}{dz} = 0$ and with $\phi(\nu)$ having an LTE appearance, as shown in Figure 4.5 for various values of the kinetic temperature. Under such conditions, the spectra of the masers will take on the LTE appearance of $\phi(\nu)$. But, from a comparison of the spectra shown in Figure 4.5 with,

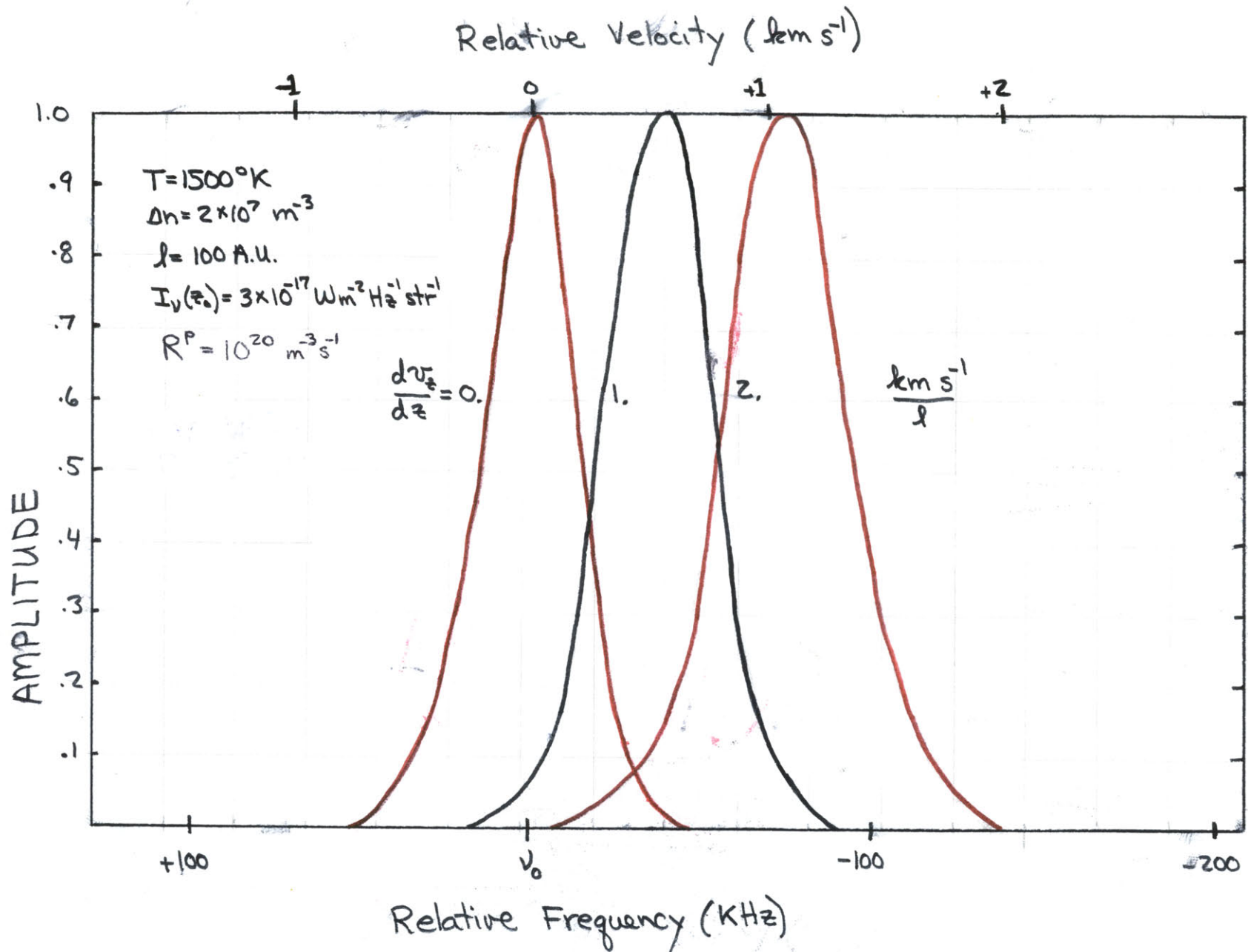


Figure 6.2 The normalized spectrum, I_ν vs ν , of unsaturated model H_2O masers for several linear variations of $v_z(z)$ over the path length l .

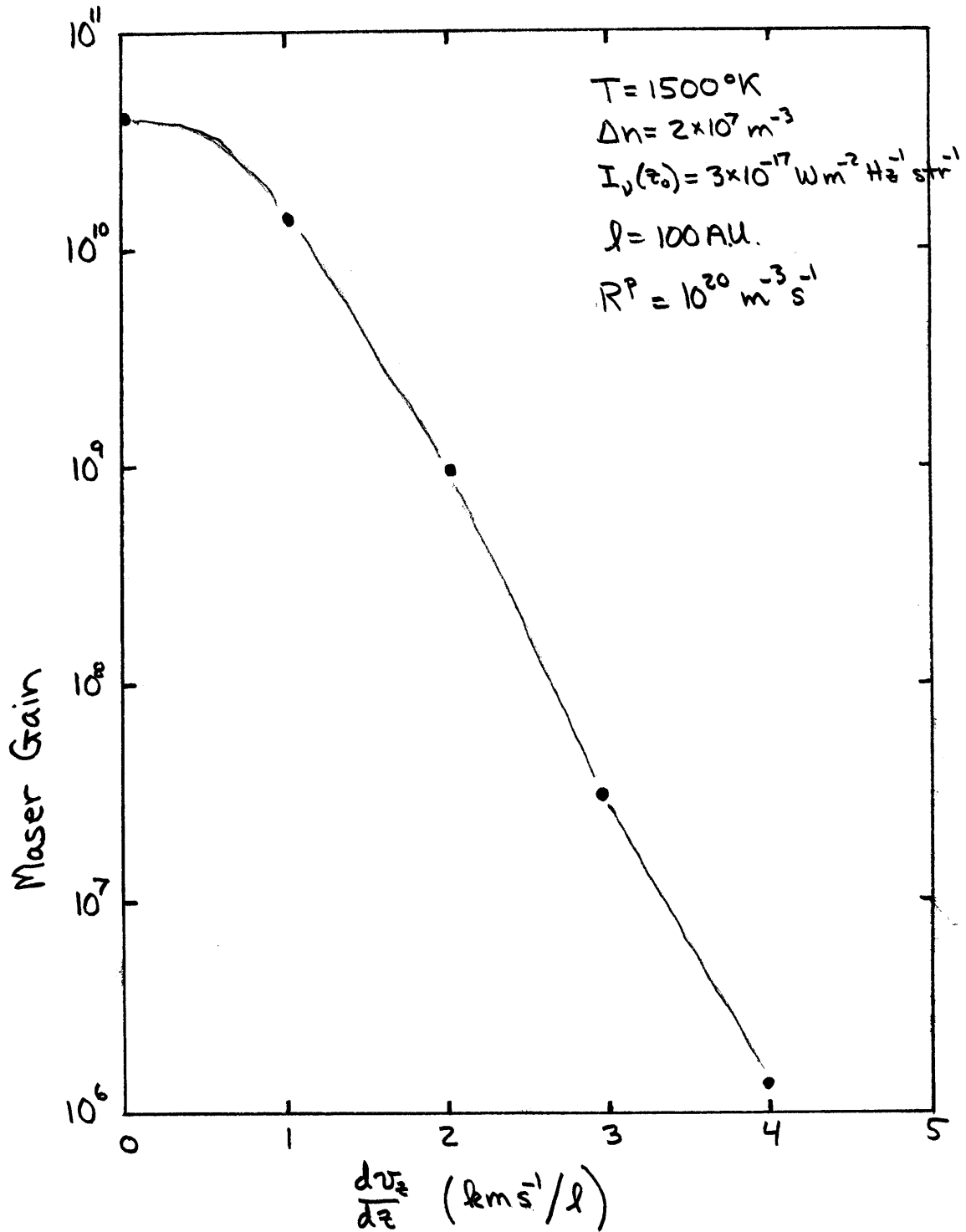


Figure 6.3 The maser gain vs. adopted $\frac{dv_z}{dz}$ values for the linear variation of $v_z(z)$ over a maser path length l .

for example, those shown in Figures 5.4 through 5.6, we see that there is no value of the kinetic temperature for which $\phi(\nu)$ would match the observed spectra. At the sufficiently low temperatures needed to match the narrow widths of the observed spectra, the individual hyperfine components would be clearly distinguishable. At the higher temperatures needed for a "blending" of these components, the resultant LTE profile would be far too broad to match the observed spectra. Therefore, unless changes in the relative populations of the hyperfine levels can be produced through some physical means yet to be established, we can conclude that a model of a fully saturated maser, with $\frac{dv_z(z)}{dz} = 0$ and with $\phi(\nu)$ having an LTE profile, can not match the observed spectra; the latter are too narrow.

Let us next consider comparisons with models of unsaturated masers. The results from such comparisons between computed spectra and the "observed" spectrum of the intense 11 km s^{-1} H_2O feature in Orion A (Feature 6 in Figure 5.9a) are summarized in Figure 6.4. The "observed" spectrum of this feature was obtained by removal of other distinct spectral features from the actual observed spectrum (Figure 5.9a) through subtraction of the Gaussian components which resulted from the spectral decompositions discussed in Chapter 5. The observation of the 11 km s^{-1} feature in Orion A from 7 August 1974 was selected for comparison with computed spectra

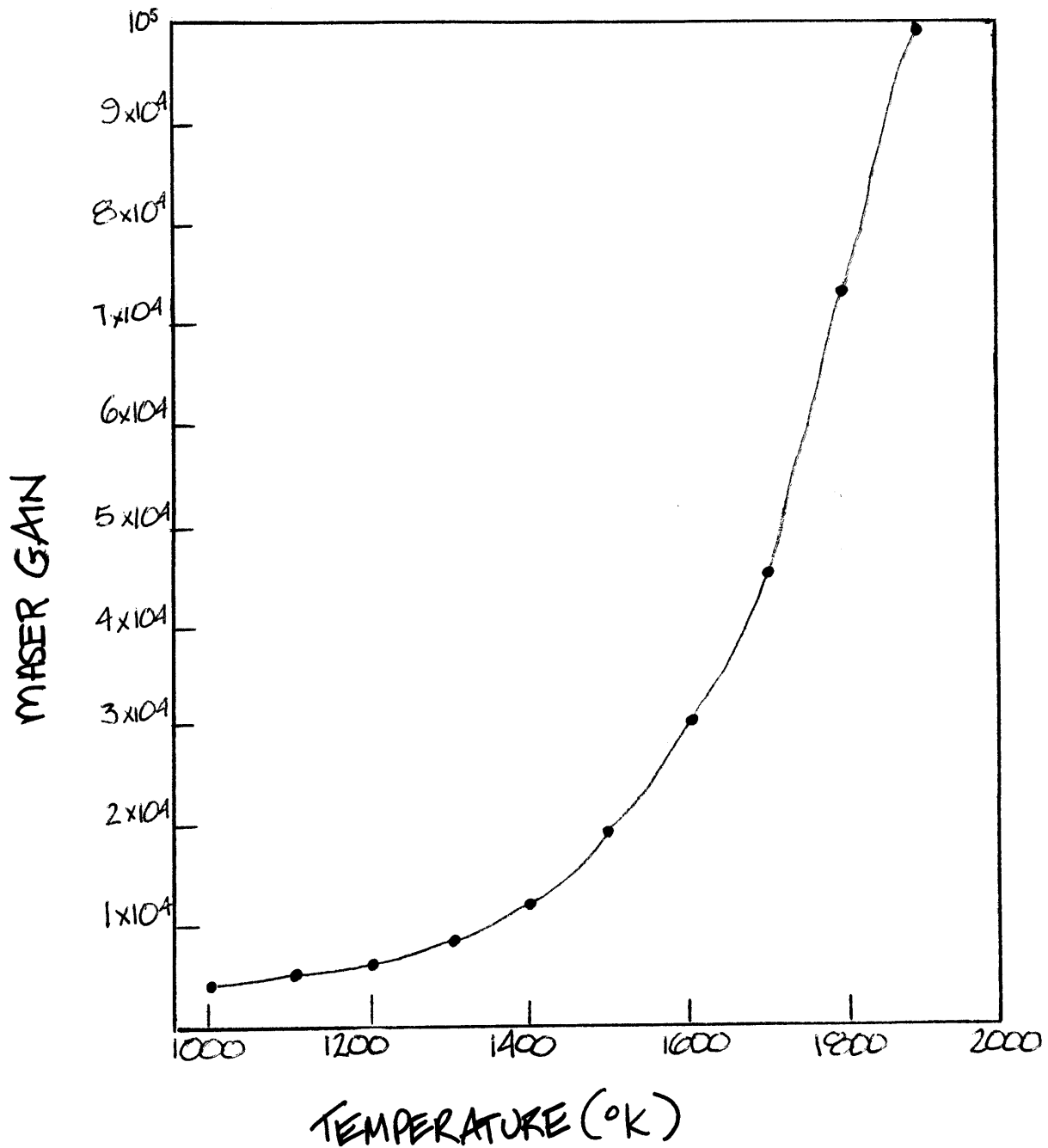


Figure 6.4 The gain of an unsaturated model H_2O maser, with $v_z(z) = \text{constant}$, which results from the least-squares fit to the 11 km s^{-1} H_2O feature spectrum seen in Figure 5.9a, for adopted values of kinetic temperature. Only the path length, ℓ , was varied in the fit.

because: (i) this feature had the highest flux density of any observed, and exhibited the "most common" spectral width associated observationally with H₂O masers (see Figure 5.12); and (ii) other distinct spectral features (Features 4 and 5 in Figures 5.8 and 5.9a), which are partially superposed, were the weakest of those found in any observing session, and thus presumably affect least our study. From Figure 6.4 it is evident that the observed spectrum is too broad to have resulted from an unsaturated maser with the expected gain* of $\sim 10^{10 \pm 2}$. For an unsaturated maser, the spectrum narrows as the gain increases, as described in Section 6.2, thus implying that if the gain were much higher than in Figure 6.4, the corresponding width of the spectrum would have been much narrower than observed.

Having ruled out unsaturated and fully saturated masers with $\frac{dv_z(z)}{dz} = 0$ and with $\phi(\nu)$ having an LTE appearance, we will now consider whether the observed spectra can result from a partially saturated maser or from an unsaturated maser with a non-zero gradient in the radial velocity $v_z(z)$ along the maser path.

* Radio interferometric observations (Moran et al., 1973) indicated that the 11 km s⁻¹ Orion maser was ~ 0.005 arcseconds in apparent diameter (2.5 A.U. at 0.5 kpc) and produced $\sim 2 \times 10^3$ Jy at the earth. If we consider the compact H_{II} region with which the H₂O masers in Orion are apparently associated to be $\sim 10^2$ arcseconds in apparent diameter, and to produce $\sim 5 \times 10^2$ Jy near 22 GHz, we arrive at a gain of $\sim 2 \times 10^9$ for our model of this maser. It is possible, although unlikely, that the apparent transverse extent of the maser emission measured interferometrically may be enlarged because of scintillation effects (Moran et al., 1973). If this were indeed the case, the estimated gain above would need to be increased.

We first consider the possibility that the broadening of the observed spectra is due to partial saturation, with $v_z(z) = \text{constant}$. As seen in Figure 6.1, when the maser is partially saturated the spectrum has visibly lost the "wings". Thus maser models which have partially saturated, with $v_z(z) \neq 0$, would not produce the observed spectra.

We next consider the possibility that the broadening is due to the variation of radial velocity $v_z(z)$ along the path length ℓ of an (unsaturated) maser. As seen in Figure 6.2, a linear variation $\sim 2 \text{ km s}^{-1}/\ell$ in $v_z(z)$ would produce sufficient broadening to explain the observed spectral widths, and the features retain the "wings" which disappear under partially saturated conditions. If the broadening of each spectrum is due primarily to the variation of radial velocity along the maser path, a noticeably narrower spectral feature would be expected to exhibit significantly higher gain. That is, if the variation of $v_z(z)$ over the path length of one unsaturated maser were less than that over the path of a second, otherwise identical maser, then the first spectrum would be expected to be narrower and more intense than the second. The most intense H_2O maser yet observed, the -1.8 km s^{-1} feature of W49 (see Figures 5.4 and 5.5) was also the narrowest found during this investigation.

The non-LTE ratios of the amplitudes of the hyperfine components seen in the interferometric spectra (Figures 5.4 through 5.6) may also be explained as the result of velocity gradients (of, say, differing sign for the W 49 and Orion

features) along the maser paths. Thus, if the frequency corresponding to the peak of $\phi(\nu, z)$ as a function of z , moves closer to that of one or another of the hyperfine lines (as measured, say, in the rest frame at z_0), then the gain associated with that hyperfine component will be relatively larger. In other words, the extra "degree of freedom" afforded by the possibility of a varying v_z can lead to non-LTE ratios of the observed amplitudes of the hyperfine components. Here, however, we found that a linear variation of v_z with z (Figure 6.2) was sufficient to yield agreement between the computed and observed spectra of individual features.

We have found that at 1500°K a maser gain of $\sim 10^{10}$ is produced over a path length ℓ of $\sim 10^2$ A.U. with $\Delta n \sim 2. \times 10^7 \text{ m}^{-3}$; at 500°K, $\Delta n \approx 1.4 \times 10^7 \text{ m}^{-3}$ for the same gain and ℓ . Because the exponent in the expression for unsaturated gain is proportional to $\ell \Delta n$, an otherwise identical maser whose path length was equal to its transverse dimension of, say, ~ 2.5 A.U., would require an effective inversion of $\Delta n \sim 8 \times 10^8 \text{ m}^{-3}$ to achieve the same gain of $\sim 10^{10}$.

The lower-bound gain of 10^8 associated with H_2O masers may be coupled with the conclusion above that the observed spectra do not result from partial saturation to estimate a lower bound for

$$(W_{\ell u}^P - W_{u\ell}^P) N_t / 2 = R^P.$$

As seen in Figure 6.1, at 1500°K an H_2O maser would be partially saturated at a gain of $\sim 10^{20}$ for $(W_{\ell u}^P - W_{u\ell}^P) N_t / 2 = R^P \sim 10^{20} \text{ m}^{-3} \text{ s}^{-1}$ and the adopted value of $I_\nu(z_0)$.

Thus, to avoid this degree of partial

saturation at a gain of $\sim 10^8$ would require $R^P > 10^8 \text{ m}^{-3} \text{ s}^{-1}$.

In this section, we did not, of course, examine all possible variations of masers. In particular, functions $\phi(\nu)$ different in shape from the LTE appearance of the spectra in Figure 4.5 were not considered. Clearly, with complete freedom to vary $\phi(\nu)$ all manner of spectra could be created. But in the absence of a cogent argument to consider conditions varying greatly from LTE for the populations of the hyperfine levels, we considered it properly conservative to restrict our exploration of maser models to those for which ϕ had an LTE appearance.

In the following chapter, we use results from the above analysis to estimate the values of the total molecular mass density ρ , and the kinetic temperature T , which characterize H_2O masers. We then consider some of the implications of this investigation for interpreting conditions of stellar formation.

CHAPTER 7

INTERPRETATIONS IN TERMS OF STELLAR FORMATION

7.1 Physical Conditions Associated with H₂O Masers

From comparisons between theory and radio observations we have estimated a consistent set of values for several parameters (e.g. Δn , R^P) characterizing regions of H₂O maser emission. In this section we use these values, and other evidence, to estimate in addition the kinetic temperature T and the total molecular mass density ρ (approximated here as $\rho = m_{H_2} N_{H_2}$). T and ρ are parameters of primary importance to the stellar formation process. We also consider further the physical origins of the values of T and ρ associated with H₂O masers.

First we consider the kinetic temperature T . In Sections 6.2 and 6.3 we found that under the combined conditions of a small gradient in radial velocity ($\sim 2 \text{ km s}^{-1}$ over the maser path length) and a high ($\sim 10^3 \text{ }^\circ\text{K}$) kinetic temperature, a model of an astrophysical H₂O maser would yield agreement with the observed radio emission properties. The H₂O 6_{16} rotational level is 0.055 eV ($8.8 \times 10^{-21} \text{ J}$) above the ground state, and thus a significant thermal (collisional) population implies $kT \gtrsim 0.055 \text{ eV}$, or $T \gtrsim 640^\circ\text{K}$. Were T less than $\sim 500^\circ\text{K}$, a noticeable (but unobserved) asymmetry would have been introduced into spectra broadened by an approximately linear variation in radial velocity along a maser path length. It is evident (see Figure 4.1) that we may place an upper limit of $\sim 2000^\circ\text{K}$ on T , since at this

temperature, or above, collisional dissociation effectively eliminates the presence of H₂O over the appropriate density range. Because of the above considerations, we have adopted here $T \sim 1200 \pm 300^\circ\text{K}$ as representative of the kinetic temperature and one standard deviation error limits in an astrophysical H₂O maser. Clearly the mere presence of H₂O molecules in a region also indicates that it is somehow insulated from the intense ultraviolet in the optically emitting H_{II} plasma (e.g. Stief, 1972).

Next we consider the total molecular mass density ρ , approximated here as $\rho = m_{\text{H}_2} N_{\text{H}_2}$. In Section 6.3 we estimated the population density of the effective inversion $10^9 \geq \Delta n \geq 10^7 \text{ m}^{-3}$, and the effective pump rate $R^P \geq 10^8 \text{ m}^{-3} \text{ s}^{-1}$. Figure 7.1 illustrates the physical relationships between the various population densities in the unsaturated portion of a maser. The relationship between the population density of the effective inversion, Δn , and that of the pump inversion ΔN is

$$\begin{aligned} \Delta n &\equiv N_u - N_l \\ &= \Delta N - [N_l(\text{LTE}) - N_u(\text{LTE})] \\ &= \Delta N - N_{\text{H}_2\text{O}} [f_{5_{23}} - f_{6_{16}}] \end{aligned} \quad (7.1)$$

where $\Delta N \equiv N_u - N_u(\text{LTE}) - [N_l - N_l(\text{LTE})]$, and where $f_* = N_*/N_{\text{H}_2\text{O}}$ is the appropriate rotational partition function (the fraction of H₂O molecules which reside in the * level in LTE. Numerical evaluation[†] of the rotational partition functions for H₂O yields

[†]See Appendix C.

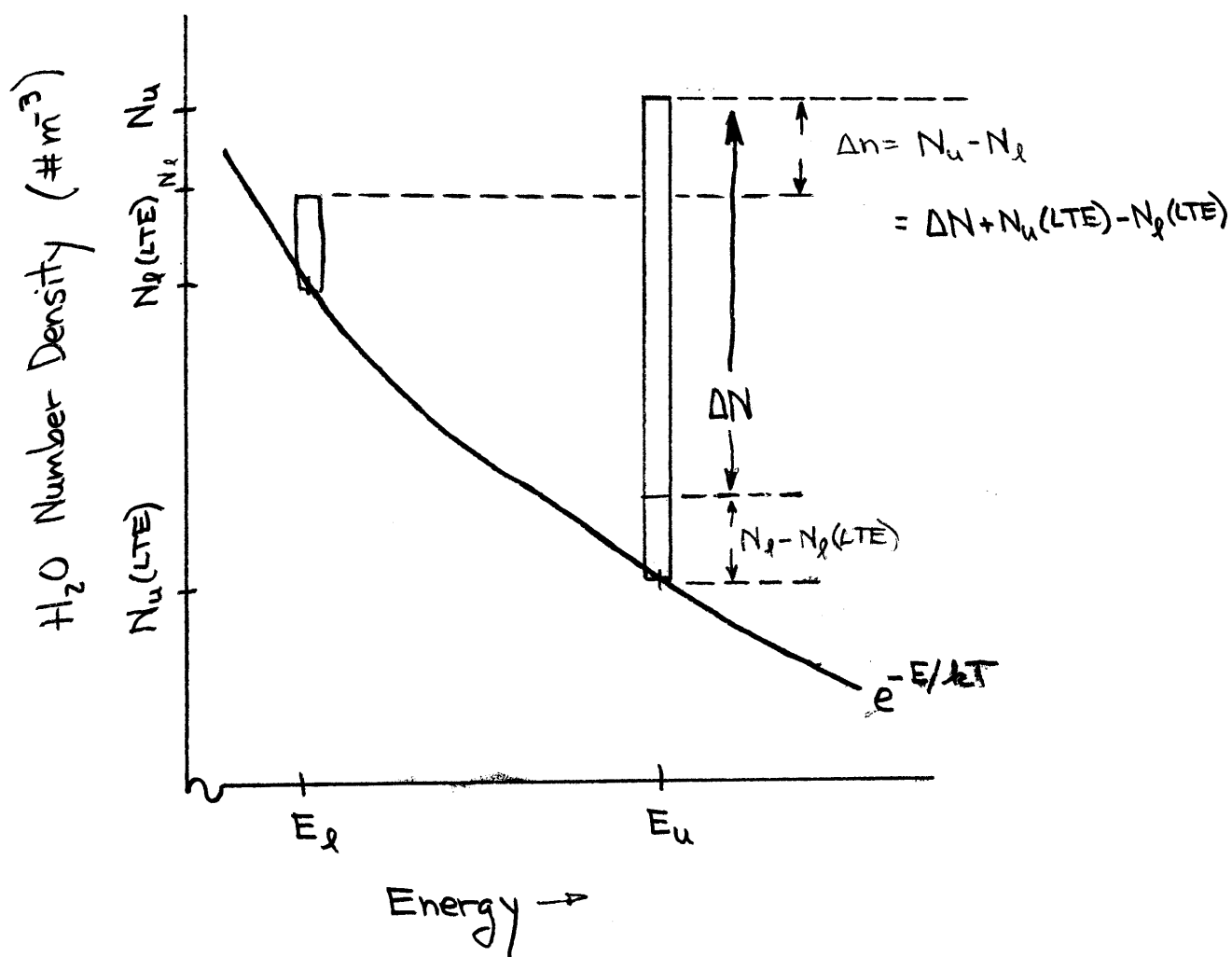


Figure 7.1 Schematic representation of the H_2O population densities in the unsaturated portion of a maser. Clearly

$$\int NdE = N_{H_2O}$$

$$[f_{5_{23}} - f_{6_{16}}] \sim \begin{cases} 10^{-5} & \text{at } T = 1500^\circ\text{K} \\ 10^{-4} & \text{at } T = 500^\circ\text{K} \end{cases} .$$

In order to place bounds on N_{H_2} we will consider the rate equations (see Section 6.1) under the two physical limits of Equation (7.1), with the additional assumption that in the unsaturated portion of the maser R^{P} is balanced by collisions. Under these conditions the rate equations yield

$$W^{\text{C}} \Delta N = R^{\text{P}}$$

where $W^{\text{C}} = 1/\tau$ is the probability per second that an H_2O molecule in the maser levels suffers a collision. τ is a crude estimate of the time required for collisions to reestablish an LTE distribution of H_2O rotational levels. We will consider $\text{H}_2\text{O} - \text{H}_2$ collisions to predominate in estimating W^{C} , although (as seen in Figure 4.1) $\text{H}_2\text{O} - \text{H}$ collisions also become important under high temperature/low pressure conditions. The collision probability W^{C} , assuming hard sphere collisions, is then

$$W^{\text{C}} = \frac{1}{\tau} \sim \pi \left[\frac{d_{\text{H}_2\text{O}} + d_{\text{H}_2}}{2} \right]^2 \bar{v} N_{\text{H}_2} \quad (7.2)$$

where \bar{v} is the average relative speed between the H_2O and H_2 molecules, and d is the molecular diameter. Numerical evaluation* of Equation (7.2) yields

*See Appendix D.

$$\tau(1500^\circ\text{K}) \sim \left[\frac{10^{15} \text{m}^{-3}}{N_{\text{H}_2}} \right] \text{ s}$$

where $\tau \propto T^{-\frac{1}{2}}$.

A lower bound estimate for N_{H_2} can now be obtained by considering the limiting case of a strong pump, limited by collisions, for which the difference in equilibrium populations $|N_{\text{u}}(\text{LTE}) - N_{\text{l}}(\text{LTE})|$ is negligible with respect to the difference which results from the pump mechanism. In this case

$$\Delta n \sim \Delta N = R^{\text{P}} \tau .$$

Since

$$R^{\text{P}} \tau \sim \Delta n \leq 10^9 \text{ m}^{-3}$$

and

$$R^{\text{P}} \gtrsim 10^8 \text{ m}^{-3} \text{ s}^{-1}$$

then

$$\tau \leq 10 \text{ s}; \text{ or } N_{\text{H}_2} \gtrsim 10^{14} \text{ m}^{-3} .$$

For the second limiting case, that of a weak pump barely sufficient to maintain Δn positive against the effect of collisions, we find $\Delta N \sim N_{\text{l}}(\text{LTE}) - N_{\text{u}}(\text{LTE}) \gg \Delta n$. Then in this case

$$R^{\text{P}} \tau = \Delta N \gtrsim N_{\text{H}_2\text{O}} [10^{-5}] \text{ m}^{-3} .$$

The probability for infrared cascade between H_2O rotational levels of $\sim 1 \text{ s}^{-1}$ (de Jong, 1974) would be expected to limit the pump supply rate to $R^{\text{P}} < N_{\text{H}_2\text{O}} \text{ m}^{-3} \text{ s}^{-1}$, and thus $\tau > 10^{-5} \text{ s}$; or $N_{\text{H}_2} < 10^{20} \text{ m}^{-3}$. Because of the above considerations we adopt $N_{\text{H}_2} \sim 10^{16+2} \text{ m}^{-3}$ as adequately representative of the H_2 number density and one standard deviation error limits in an astrophysical H_2O maser.

We now consider briefly possible physical origins of the kinetic temperature T and the molecular mass density ρ as stated above to be representative of H_2O maser regions. We have previously suggested that the H_2O masers associated with Galactic H_{II} regions are located in the H_I - H_{II} transition region (see Figures 3.15 and 7.2). Other investigators (e.g. Vandervoort, 1963; Lasker, 1966) have attempted to determine conditions expected in this transition region as part of their efforts to model the formation and evolution of H_{II} regions. The values of temperature and density they calculate for the transition region are highly dependent upon the adopted initial H_I density and temperature, and upon the radiative processes in the transition region. Several qualitative results from their investigations are schematically presented in Figure 7.2.

As one possible means of producing the physical conditions associated with H_2O masers, we consider the adiabatic compression of a dense H_I region from initial conditions of $T_1 \sim 10^\circ K$ and $N_{H_2} \sim 10^{11} m^{-3}$, to a final density of $N_{H_2} \sim 10^{16} m^{-3}$. Such a process would result in the kinetic temperature

$$T_2 = \left(\frac{\rho_1}{\rho_2}\right)^{1-\gamma} T_1, \text{ where } \gamma \text{ is the ratio of specific heats,}$$

since for an adiabatic process in an ideal gas $PV^\gamma = \frac{\rho}{\mu} RTV^\gamma =$ constant. For $\gamma = \frac{7}{5}$ (diatomic), $T_2 \sim 10^3 K$. This temperature is approximately that which we have associated with H_2O masers.

Thus adiabatic compression of a dense H_I region could result in the values of T and ρ we have associated with H_2O masers.

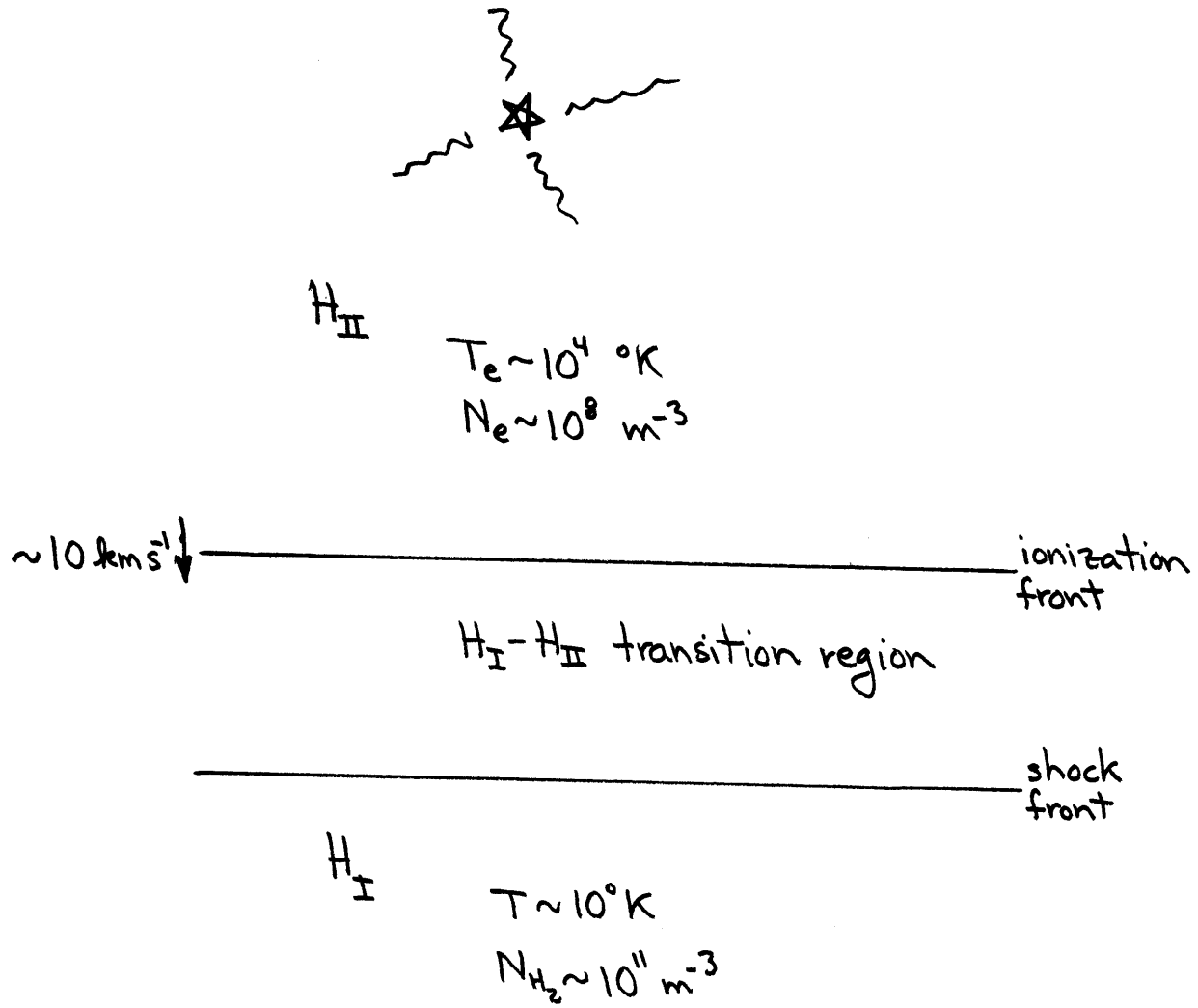


Figure 7.2 Schematic representation of an ionization front moving at $\sim v_{\text{sound}}(H_{II}) \sim v_{\text{thermal}}(H_{II}) \sim 10 \text{ km s}^{-1}$ into a dense H_{II} region, preceded by a shock front. The ionization and shock fronts bound the $H_{II} - H_I$ transition region. The kinetic pressure in the H_I region balances that in the H_{II} plasma for the values of temperature and density shown here. The ionization front is being driven as a result of the intense ultraviolet radiation from the young O-class star which is responsible for the ionization of the H_{II} region.

From Figure 2.1 it is seen that $N_{\text{H}_2} \sim 10^{16} \text{ m}^{-3}$ and $T \sim 10^3 \text{ }^\circ\text{K}$ could alternatively be produced in the envelope of an accreting protostar, at a radial distance of $\sim 1 \text{ A.U.}$ The high value of the infall velocity ($\sim 30 \text{ km s}^{-1}$) at 1 A.U. , however, leads to an order of magnitude larger gradient in radial velocity than that which we found could be attributed to an observed H_2O maser. We will present additional evidence in the next section supporting this conclusion that the Jeans collapse of an H_I region is not the mechanism for producing the physical conditions we have associated with H_2O masers.

The values of the molecular mass density and kinetic temperature we have adopted as representative of H_2O masers have implications concerning stellar formation processes. Such implications are considered further in the following section.

7.2 Implications of Physical Conditions for Stellar Formation Processes

In the preceding section we adopted $T \sim 1200 \pm 300^\circ\text{K}$ and $N_{\text{H}_2} \sim 10^{16 \pm 2} \text{ m}^{-3}$ as representative of the regions occupied by H_2O masers associated with young Galactic H_{II} regions. In this section we consider the implications of such physical conditions for processes involving stellar formation.

When gravitational forces are included in the equations governing the propagation of compressional waves (sound) in an ideal gas, an instability (collapse) results for wave numbers k such that (e.g. Chandrasekhar, 1961)

$$k \equiv \frac{2\pi}{\lambda} < \frac{\sqrt{4\pi G\rho}}{v_{\text{sound}}} \quad (7.3)$$

This instability criterion was first obtained by Jeans (1902), and now bears his name. For an ideal gas, $v_{\text{sound}} = \sqrt{\gamma RT/\mu}$, where γ is the ratio of specific heats, μ is the molecular weight, and $R = 8.32 \times 10^3 \text{ J (kg mole } ^\circ\text{K)}^{-1}$ is the universal gas constant. Then, given the Jeans (wave)length, λ_{J} , collapse would be expected for

$$\lambda > \lambda_{\text{J}} \equiv \sqrt{\frac{\gamma RT\pi/\mu}{G\rho}} \quad (7.4)$$

The mass of a star resulting from such a collapse would be

$$M_* = \frac{4}{3} \pi r^3 \rho \quad (7.5)$$

where $r = \alpha \lambda_{\text{J}}$ with $\alpha < 1$. Through numerical experiments with $\rho \approx \text{constant}$, Larson (1969) has found $\alpha \sim 0.4$. The initial radius of the gas cloud may be obtained from Equations (7.4)

and (7.5) as

$$r = \frac{r^3}{r^2} \leq \frac{3M_*}{4\pi^2} \frac{G}{\alpha^2 (\gamma/\mu) RT} \sim 0.5 \frac{GM_*}{(\gamma/\mu) RT}$$

Thus for a star of $1M_{\odot}$ (the example of Larson's computations shown in Figure 2.1), an assumed initial temperature of 10°K fixes the maximum radius and minimum density for an H_2 cloud ($\gamma = 7/5$; $\mu = 2 \text{ gm mole}^{-1}$) at $r \sim 10^4 \text{ A.U.}$, $\rho \sim 1.1 \times 10^{-16} \text{ kg m}^{-3} \sim 3.3 \times 10^{10} m_{\text{H}_2} \text{ m}^{-3}$. These values of initial temperature and density adopted by Larson are similar to those attributed to dense H_2 clouds (H_I regions) along the Galactic spiral arms (e.g. Thaddeus et al., 1971).

In a medium with the conditions we have adopted as representative of H_2O masers ($N_{\text{H}_2} \sim 10^{16} \text{ m}^{-3}$; $T \sim 1200^{\circ}\text{K}$) the Jeans wavelength would be changed by a factor of

$$\sqrt{\frac{1.2 \times 10^2}{3. \times 10^5}} \sim \frac{1}{50} \text{ from that evaluated above, i.e. would be}$$

$\sim 200 \text{ A.U.}$, and would result in the formation of a star with mass $\sim 2M_{\odot}$ (in a time reduced by a factor $\sim 1/550$). The Jeans length under these physical conditions is thus found to be roughly comparable to the observed transverse separations between individual H_2O masers (see, e.g., Figure 5.1). It is evident, however, that the H_2O masers themselves are indicative of nonhomogeneous conditions on this length scale. Inhomogeneities on the scale of a Jeans length or smaller are required in order to allow

formation of planets and multiple star systems, as distinct from single stars. Since about 50% of the classified Population I stars are multiple (e.g., Schwarzschild, 1958), such inhomogeneities must be commonplace during stellar formation. The possibility (demonstrated to be unlikely in the preceding section) that the neighborhoods of individual H₂O masers are associated with protostars which have resulted from the gravitational collapse of regions initially $\sim 10^4$ A.U. in radius and $\sim 10^\circ\text{K}$ in kinetic temperature is additionally inconsistent with the apparent close "packing" observed (at least in the transverse components) for the various H₂O masers in a given source.

At $N_{\text{H}_2} \sim 10^{16} \text{ m}^{-3}$, the mass contained within various representative volumes would be

$V = 1 \text{ AU}^3$	$M \sim M_{\text{J}}$
$V = 10^3 \text{ AU}^3$	$\sim 15 M_{\oplus}$
most common (Class M) stars $\rightarrow V = 10^6 \text{ AU}^3$	$\sim 50 M_{\text{J}} \sim 0.05 M_{\odot}$
$V = 10^9 \text{ AU}^3$	$\sim 50 M_{\odot}$

We thus expect individual H₂O masers to represent masses between $\sim M_{\oplus}$ and $\sim M_{\odot}$. We conclude that an accurate knowledge of the complete dynamics of individual H₂O masers might yield a much improved understanding of the process of planetary and stellar formation. Some initial considerations in this vein are contained in the following section.

7.3 Dynamics Associated with Stellar Formation

From our comparisons of calculated and observed spectra for individual H₂O maser features in a given source, we may conclude that the differences in the radial velocities deduced for the various features represent the actual differences in radial velocities for such regions to within a few kilometers per second. Here we will examine the consequences resulting from the assumption that the spreads in radial velocities observed for H₂O masers are characteristic of regions associated with stellar formation.

We consider first the possibility that the formation of most Population I field stars accompanied the formation of galactic clusters, the field stars having escaped soon after formation due to their large velocities with respect to escape velocity. The argument can be presented as follows. In Chapter 3 we noted the chronological progression from old galactic clusters, such as M67, through intermediate age galactic clusters, such as the Pleiades, to young galactic clusters, such as Orion, with their associated H_{II} regions. Dynamical consideration of the typical numbers of stars (and their associated masses) in these clusters, as a function of time, leads to the conclusion that in perhaps 10⁷ years (Chandrasekhar, 1942) regions of current stellar formation, such as Orion, M17, and IC 1795 will typically each result in an intermediate-aged dynamically-relaxed galactic cluster of total mass ~300 M_☉, with a dispersion in the speeds of the stellar members of $\sigma_v \sim 0.5 \text{ km s}^{-1}$ and a mean radius of $\bar{r} \sim 3 \text{ pc}$ (Chandrasekhar,

1942). Our point is that the initial period of stellar formation may lead to a far larger number of stars than remain as a bound cluster, since the mass of the region during stellar formation is typically far larger than that of the resultant cluster. Let us examine semi-quantitatively the evidence that supports such a contention. Figure 5.6, for Orion, shows that the distinct H₂O features have radial velocities with a dispersion of about 10 km s⁻¹. Therefore, the dispersion in speeds would be expected to be $\sigma_v \sim 10\sqrt{3}$ km s⁻¹. If the escape velocity from the cluster were $v_e \sim 1$ km s⁻¹ (as deduced from the Virial theorem and the above-quoted dispersion of 0.5 km s⁻¹), then, of all stars formed, only the fraction given by

$$\frac{4\pi^{3/2}}{(\sqrt{2\pi}\sigma_v)^3} \int_0^{v_e} \left[\exp\left(-\frac{3v^2}{2\sigma_v^2}\right) \right] v^2 dv \sim 3 \times 10^{-4}$$

would be gravitationally bound and retained as a galactic cluster. Formation of a typical galactic cluster of $\sim 300 M_\odot$ may thus also result in the production of $\sim 10^6 M_\odot$ (we assume for simplicity that $\bar{M}_* \sim M_\odot$) of Population I field stars. It appears reasonable to postulate that the preponderance of Population I stars are formed in this manner. One might also expect under such circumstances that the current velocity dispersion of ~ 15 km s⁻¹ observed among Population I field stars 'resulted' primarily as a consequence of the dispersion in velocities associated with

their formation. We also note that the dynamical dissolution of (relaxed) clusters (Chandrasekhar, 1942) does not appear capable of providing more than ~2% of the Population I field stars. This upper limit on the number of stars that might once have been members of now-dissolved galactic clusters was deduced by Wielen (1971) using statistics based on the catalogues of Lindoff (1968) and of Becker and Fenkart (1971).

In the radio galaxy M82 (e.g. Sandage, 1964) ionization fronts are apparently being driven into H_I clouds by clusters of O stars, rather than by a single O star as is characteristic of Population I stellar formation along galactic spiral arms. The greater the intensity of the radio H_{II} region in our Galaxy, the higher the velocity dispersion we would associate with stellar formation (e.g. $\sigma_{\text{Orion}} \sim 10 \text{ km s}^{-1}$; $\sigma_{\text{W49}} \sim 50 \text{ km s}^{-1}$). The large velocity dispersion implied for M82 suggests in that galaxy we are witness to a brief period of extremely rapid stellar formation. The formation of the Population II stars and globular clusters could have occurred under similar conditions early in the history of our Galaxy.

We now turn to a consideration of a possible example of the dynamics associated with the formation of individual multiple-star systems of a few members each, as distinguished from the preceding consideration of dynamics associated with the formation of large clusters of stars. In the preceding section we noted that multiple-star systems represent about 50% of classified Population I stars. If we assume the estimated transverse

separations between the -48.8 and -50.4 km s^{-1} H_2O masers in W3(OH) and the observed spread in their radial velocities to be representative of all of the components of their relative positions and velocities, then, in crude approximation, these two masers represent a gravitationally bound system if

$$(3 \text{ km s}^{-1})^2 < \frac{2G[M_1+M_2]}{r}$$

where 3 km s^{-1} , the assumed difference in speed, is approximately $\sqrt{3}$ greater than the deduced difference in radial velocity, and where $r \sim 50$ A.U. (see Table 5.2); i.e. if

$$\bar{M} = \frac{M_1+M_2}{2} > 2 \times 10^{29} \text{ kg} \sim 0.1 M_{\odot} .$$

We conclude, in light of the values deduced in Section 7.2 for the masses associated with H_2O masers, that the two masers considered may indeed represent a gravitationally bound system.

7.4 Future Investigation

Several technological advances slated for implementation in the near future will significantly improve the spectral resolution of radio observations of H_2O masers over that achieved during this investigation. For example, the resolution of spectra from single-antenna observations, such as those presented here, will be substantially improved following installation of 1024-channel digital correlators presently under development (e.g., at Haystack Observatory). When a sufficient number of cryogenic receivers and wide bandwidth recorders are available,

wide bandwidth VLBI observations on the longest available interferometer baselines will enable not only high resolution individual H_2O maser spectra to be obtained, but will also allow accurate determinations of the relative angular positions of the individual masers in a given source, and of the three components of their relative velocities if the observations are repeated over a sufficiently long time period. Such observations might be expected to yield significant information on the detailed dynamics of stellar and planetary formation.

Application of the techniques developed for the computation of maser spectra in this investigation, and specifically applied here to the examination of the spectra of H_2O masers associated with Galactic H_{II} regions, may also prove useful in the study of H_2O , SiO , and OH maser spectra associated with infrared stars. The statistical method (Reisz et al., 1973), by means of which the inherent position accuracy of VLBI observations can be extracted, has general application in the analysis of all similar VLBI data.

It is evident that a current in-depth theoretical-numerical investigation of the physical conditions in H_I - H_{II} transition regions would be of great interest. Such a study should make use of the vast observational information base recently compiled on these regions through radio observations, such as those discussed and presented here.

References

- Allis, W. P., Buchsbaum, S. J., Bers, A. 1963. Waves in Anisotropic Plasmas (Cambridge: M.I.T. Press).
- Ash, M. E. 1972. "Determination of Earth Satellite Orbits", Technical Note 1972-5, Lincoln Laboratory.
- Bare, C. C., Clark, B. G., Kellermann, K. I., Cohen, M. H., and Jauncey, D. L. 1967. Science 157, 189.
- Barshay, S. S. and Lewis, J. S. 1976. "Chemistry of Solar Material", The Dusty Universe, G. B. Field, A. G. W. Cameron, eds., (New York: Neale Watson Academic Publications).
- Becklin, E. E. and Neugebauer, G. 1967. Ap. J. 147, 799.
- Bergh, S. van den. 1968. The Galaxies of the Local Group, Communication #195 of the David Dunlap Observatory.
- Bluyssen, H., Dymanus, A., and Verhoeven, J. 1967. Phys. Lett. 24A, 482.
- Bowen, I. S. 1928. Ap. J. 67, 1.
- Brecher, A., Briggs, P. L., and Simmons, G. 1975. E. and Pl. Sci. Lett. 28, 37.
- Burke, B. F. and Strandberg, M. W. P. 1953. Phys. Rev. 90, 303.
- Burke, B. F., Papa, D. C., Papadopoulos, G. D., Schwartz, P. R., Knowles, S. H., Sullivan, W. T., Meeks, M. L., and Moran, J. M. 1970. Ap. J. 160, L63.
- Burke, B. F., Johnston, K. J., Efanov, V. A., Clark, B. G., Logon, L. R., Kostenko, V. I., Lo, K. Y., Matveenko, L. I., Moiseev, I. G., Moran, J. M., Knowles, S. H., Papa, D. C., Papadopoulos, G. D., Rogers, A. E. E., and Schwartz, P. R. 1972. Soviet Astr. AJ 16, 379.
- Chaisson, E. J. and Beichman, C. A. 1975. Ap. J. Lett. 199, L39.
- Chandrasekhar, S. 1939. An Introduction to the Study of Stellar Structure (New York: Dover Publications).
- Chandrasekhar, S. 1942. Principles of Stellar Dynamics (New York: Dover Publications).
- Chandrasekhar, S. 1961. Hydrodynamic and Hydromagnetic Stability (Oxford: Clarendon Press).
- Chapman, C. R. 1975. Scientific American 232, 24.
- Cheung, A. C., Rank, D. M., Townes, C. H., and Welch, W. J. 1969. Nature 221, 917.

- Conant, G. H. and Meeks, M. L. 1968. Technical Note 1968-1, Lincoln Laboratory, Lexington, Mass.
- Curtis, H. D. 1919, J. Wash. Academy Sci. 9, 217.
- Davenport, W. B. and Root, W. L. 1958. Random Signals and Noise (New York: McGraw Hill).
- Davidon, W. C. 1959. A. E. C. Research and Development Report ANL-5990.
- Dufay, J. 1964. Introduction to Astrophysics: The Stars (New York: Dover Publications, Inc.).
- Fletcher, R. and Powell, M.J.D. 1963. Comp. J. 6, 163.
- Gaffey, M. J. 1974. Ph.D. Thesis, M.I.T., Dept. of Earth and Planetary Sciences.
- Gaustad, J. E. 1963. Ap. J. 138, 1050.
- Goldreich, P. and Keeley, D. A. 1972. Ap. J. 174, 517.
- Goldreich, P. and Ward, W. R. 1973. Ap. J. 183, 1051.
- Gordon, M. A. and Snyder, L. E. 1973. Molecules in the Galactic Environment (New York: John Wiley and Sons).
- Gwinn, W. D., Turner, B. E., Goss, W. M. and Blackman, G. L. 1973. Ap. J. 179, 789.
- Harper, D. A. and Low, F. J. 1971. Ap. J. Lett. 165, L9.
- Hayashi, C. 1966. Ann. Rev. Astr. Astrophys. 4, 171.
- Heald, M. A. and Wharton, C. B. 1965. Plasma Diagnostics with Microwaves (New York: John Wiley and Sons).
- Hermann, A. 1971. The Genesis of Quantum Theory (Cambridge: M.I.T. Press).
- Hertzberg, G. 1945. Spectra of Diatomic Molecules (New York: D. Van Nostrand).
- Hertzberg, G. 1944. Atomic Spectra and Atomic Structure (New York: Dover Publications).
- Höglund, B. and Mezger, P. G. 1965. Science 150, 339.
- Hubble, E. 1926. Ap. J. 64, 321.
- International Astronomical Union 1963, IAU Information Bull. No. 11.

- Jahnke, E. and Emde, F. 1945, Tables of Functions (New York: Dover Publications).
- Johnston, K. J. and Hobbs, R. W. 1973. A. J. 78, 235.
- Kleinmann, D. E. and Wright, E. L. 1973. Ap. J. Lett. 185, L131.
- Knowles, S. H., Mayer, C. H., Cheung, A. C., Rank, D. M., Townes, C. H. 1969. Science 163, 1055.
- Kukolich, S. G. 1969. J. Chem. Phys. 50, 3751.
- Larson, R. B. 1969. Mon. Not. R. Astr. Soc. 145, 271.
- Larson, R. B. 1969. Mon. Not. R. Astr. Soc. 145, 297.
- Larson, R. B. 1972. Mon. Not. R. Astr. Soc. 157, 121.
- Lasker, B. M. 1966. Ap. J. 143, 700.
- Lewis, J. L. 1974. Science 186, 440.
- Litvak, M. M. 1969. Science 165, 855.
- Litvak, M. M. 1970. Phys. Rev. A., 2, 2107.
- Litvak, M. M. 1971. Ap. J. 170, 71.
- Litvak, M. M. 1973, "Masers and Optical Pumping:", in Molecules in the Galactic Environment, eds. M. A. Gordon and L. E. Snyder (New York: John Wiley and Sons).
- Meeks, M. L., Carter, J. C., Barrett, A. H., Schwartz, P. R., Waters, J. W., and Brown, W. E. 1969. Science 165, 180.
- Meeks, M. L., ed., Methods of Experimental Physics, Vol 12, Part C. (New York: Academic Press) (in press, 1976).
- Menon, T. K. 1962. Ap. J. 136, 95.
- Mezger, P. G. and Henderson, A. P. 1967. Ap. J. 147, 471.
- Mezger, P. G. and Höglund, B. 1967. Ap. J. 147, 490.
- Miller, J. S. 1974. Scientific American 231, 34.
- Moran, J. M. 1968. Ph.D. Thesis, M.I.T.
- Moran, J. M., Papadopoulos, G. D., Burke, B. F., Lo, K. Y., Schwartz, P. R., Thacker, D. L., Johnston, K. J., Knowles, S. H., Reisz, A. C., and Shapiro, I. I. 1973. Ap. J. 185, 535.

- Moran, J. M. 1976. In Methods of Experimental Physics, Vol. 12, Part C, (New York: Academic Press) (in press, 1976).
- Morse, P. 1965. Thermal Physics (New York: W. A. Benjamin).
- Oka, T. 1973, "Selective Predissociation as a Possible Mechanism for the Population Inversion of Interstellar H₂O", in Molecules in the Galactic Environment, eds. M. A. Gordon and L. E. Snyder (New York: John Wiley and Sons).
- Radford, H. E. 1962. Phys. Rev. 126, 1035.
- Reisz, A. C., Paul, D. L., and Madden, T. R. 1972. The Moon 4, 134.
- Reisz, A. C., Shapiro, I. I., Moran, J. M., Papadopoulos, G. D., Burke, B. F., Lo, K. Y., and Schwartz, P. R. 1973. Ap. J. 186, 537.
- Roberts, M. S. 1974. Science 183, 371.
- Rönnäng, B. O. 1972. R. L. E. Report #101, Chalmers University of Technology, Gothenburg, Sweden.
- Rossi, B. and Olbert, S. 1970. Introduction to the Physics of Space (New York: McGraw-Hill).
- Safronov, V. S. 1969. Evolution of the Protoplanetary Cloud and Formation of the Earth and the Planets, Izdatel'stvo "Nauka", Moskva.
- Sandage, A.R. 1964. Frontiers in Astronomy (San Francisco: W.H. Freeman).
- Schwarzschild, M. 1958. Structure and Evolution of the Stars (New York: Dover Publications).
- Shapley, H. 1919. Publications of the Astronomical Society of the Pacific 31, 261.
- Snyder, L. E. and Buhl, D. 1971. Ap. J. Lett. 163, L47.
- Snyder, L. E. and Buhl, D. 1974. Ap. J. Lett. 189, L31.
- Snyder, L. E. and Buhl, D. 1975. Ap. J. 197, 329.
- Sonett, C. P., Colburn, D. S., and Schwartz, K. 1968. Nature 219, 924.
- Staff, Smithsonian Astrophysical Observatory. 1966. Smithsonian Astrophysical Observatory Star Catalog (Washington: U. S. Government Printing Office), 3.
- Stief, L. J. 1972. Mol. Photochem. 4(1), 153.
- Sugden, T. M. and Kenney, C. N. 1965. Microwave Spectroscopy of Gases (London: D. Van Nostrand).

- Sullivan, W. T. 1971. Ph. D. Thesis, University of Maryland.
- Sullivan, W. T. 1971. Ap. J. 166, 321.
- Sullivan, W. T. 1973. Ap. J. Supplement Series, No. 222, 25, 393.
- Terzian, Y. 1965. Ap. J. 142, 135.
- Thaddeus, P., Wilson, R. W., Kutner, M., Penzias, A. A., and Jefferts, K. B. 1971. Ap. J. Lett. 168, L59.
- Titus, J. 1938. A. J. 47, 25.
- Toksöz, M. N. and Solomon, S. C. 1973. The Moon 7, 251.
- Townes, C. H. and Schawlow, A. L. 1955. Microwave Spectroscopy (New York: McGraw-Hill Book Co.).
- Vandervoort, P. O. 1963. Ap. J. 138, 426.
- Van Vleck, J. H. and Middleton, D. 1966. Proc. I.E.E.E. 54, 2.
- Wasson, J. T. 1972. Reviews of Geophysics and Space Physics 10, 711.
- Weaver, H., Williams, D. R. W., Dieter, N. H., and Lum, W. T. 1965. Nature 208, 29.
- Weinreb, S. 1963. R.L.E. Technical Report 412, M.I.T.
- Wielen, R. 1971. "The Age Distribution and Total Lifetimes of Galactic Clusters", Astron. and Astrophys. 13, 309.
- Wynn-Williams, C. G., Becklin, E. E. and Neugebauer, G. 1972. Mon. Not. R. Astr. Soc. 160, 1.
- Yngvesson, K. S., Cardiasmenos, A. G., Shanley, J. F., Rydbeck, O. E. H., and Ellder, J. 1975. Ap. J. 195, 91.
- Zuckerman, B. 1973. Ap. J. 183, 863.

APPENDIX A

Numerical Minimization Technique

We have the complex observed spectrum $S(v_k)$, where $v_k = v_{\min} + (k - 1)\Delta v$ and $k = 1 \rightarrow M$. To model $S(v_k)$ in terms of J individual Gaussian components, we form the complex discrete model spectrum

$$S_{\text{model}}(v_k) = \sum_{j=1}^J A_j \exp\left[\frac{-(v_k - v_j)^2}{2\sigma_j^2} + i\phi_j\right] \quad (\text{A.1})$$

and minimize the sum of the squares of the residual magnitudes

$$R = \sum_{k=1}^M [S(v_k) - S_{\text{model}}(v_k)][S(v_k) - S_{\text{model}}(v_k)]^* \quad (\text{A.2})$$

with respect to the $4J$ parameters ($A_j, v_j, \sigma_j, \phi_j; j=1, J$).

The minimization procedure is initialized using "guesstimates" for the initial values of the $4J$ parameters. Upon each succeeding iterative step the values of R and the partial derivatives of R with respect to the $4J$ variables are computed, and the parameter values updated using IBM Scientific Subroutine Package program FMFP (Function Minimization by the method of Fletcher and Powell). The iterative minimization technique of Fletcher and Powell (1963), based on a method proposed by Davidon (1959), makes the approximation that a function (R) is adequately represented near a minimum by the first three terms of the $4J$ dimensional Taylor expansion. The gradient vector is then

$$\frac{\partial R}{\partial \underline{x}} \sim \left(\frac{\partial^2 R}{\partial \underline{x}^2} \right)_{\underline{x}=\underline{x}_{\min}} (\underline{x} - \underline{x}_{\min}) \quad (\text{A.3})$$

where \underline{x} denotes the (column) vector, the components of which comprise the 4J variables.*

* In matrix notation

$$\underline{x} = \begin{bmatrix} A_1 \\ A_2 \\ \vdots \\ A_J \\ v_1 \\ v_2 \\ \vdots \\ v_J \\ \sigma_1 \\ \vdots \\ \sigma_J \\ \phi_1 \\ \vdots \\ \phi_J \end{bmatrix} = \begin{bmatrix} x_1 \\ x_2 \\ \vdots \\ x_{4J} \end{bmatrix} ; \quad \frac{\partial R}{\partial \underline{x}} = \begin{bmatrix} \frac{\partial R}{\partial x_1} \\ \frac{\partial R}{\partial x_2} \\ \vdots \\ \frac{\partial R}{\partial x_{4J}} \end{bmatrix} ;$$

$$\underline{\underline{G}} \equiv \frac{\partial^2 R}{\partial \underline{x}^2} = \begin{bmatrix} \frac{\partial^2 R}{\partial x_1^2} & \frac{\partial^2 R}{\partial x_1 \partial x_2} & \dots & \frac{\partial^2 R}{\partial x_1 \partial x_{4J}} \\ \frac{\partial^2 R}{\partial x_2 \partial x_1} & \frac{\partial^2 R}{\partial x_2^2} & & \\ \vdots & & \ddots & \\ \frac{\partial^2 R}{\partial x_{4J} \partial x_1} & & & \frac{\partial^2 R}{\partial x_{4J}^2} \end{bmatrix}$$

Assuming the symmetric matrix

$$\underline{G}(\underline{x}_{\min}) \equiv \left(\frac{\partial^2 R}{\partial \underline{x}^2} \right)_{\underline{x}=\underline{x}_{\min}} \quad \text{to be non-singular, then}$$

$$(\underline{x} - \underline{x}_{\min}) = \underline{G}^{-1}(\underline{x}_{\min}) \frac{\partial R}{\partial \underline{x}} \quad (\text{A.4})$$

and the minimum could be located directly, if $\underline{G}^{-1}(\underline{x}_{\min})$ were known. $\underline{G}^{-1}(\underline{x}_{\min})$ is approached through a series of linear searches in "G-conjugate" directions. The initial value for $\underline{G}^{-1}(\underline{x}_{\min})$, \underline{G}_0^{-1} , is chosen to be the identity matrix. On the (i+1)st iteration step,

a linear search in direction $\underline{h}_i = -\underline{G}_i^{-1} \frac{\partial R}{\partial \underline{x}_i}$ is conducted to determine that value of s for which $R(\underline{x}_i + s\underline{h}_i)$ is minimized, thereby yielding the updated argument vector $\underline{x}_{i+1} = \underline{x}_i + s_i \underline{h}_i$. The matrix of second order partial derivatives is then updated as (Fletcher and Powell, 1963)

$$\underline{G}_{i+1}^{-1} = \underline{G}_i^{-1} + \frac{(\underline{x}_{i+1} - \underline{x}_i) (\underline{x}_{i+1} - \underline{x}_i)^T}{(\underline{x}_{i+1} - \underline{x}_i)^T \left(\frac{\partial R}{\partial \underline{x}_{i+1}} - \frac{\partial R}{\partial \underline{x}_i} \right)}$$

$$- \frac{\underline{G}_i^{-1} \left(\frac{\partial R}{\partial \underline{x}_{i+1}} - \frac{\partial R}{\partial \underline{x}_i} \right) \left(\frac{\partial R}{\partial \underline{x}_{i+1}} - \frac{\partial R}{\partial \underline{x}_i} \right)^T \underline{G}_i^{-1}}{\left(\frac{\partial R}{\partial \underline{x}_{i+1}} - \frac{\partial R}{\partial \underline{x}_i} \right)^T \underline{G}_i^{-1} \left(\frac{\partial R}{\partial \underline{x}_{i+1}} - \frac{\partial R}{\partial \underline{x}_i} \right)}$$

(A.5)

where T denotes transpose. Equation (A.5) is motivated by the effort to modify \underline{G}_i^{-1} such that \underline{h}_i is an eigenvector, with

eigenvalue 1, of the matrix $\underline{G}_{i+1}^{-1} \underline{G}(\underline{x}_{\min})$. Were R quadratic, this procedure would locate the minimum in $4J$ iterative steps (Fletcher and Powell, 1963).

APPENDIX B

COMPUTATION OF THE SPECIFIC INTENSITY $I_\nu(z)$

The following FORTRAN IV computer program determines the specific intensity $I_\nu(z-z_0)$ $\text{Wm}^{-2}\text{Hz}^{-1}\text{ster}^{-1}$ at the set of M discrete frequencies ν_k , for progressive discrete steps Δz along the H_2O maser path length coordinate z , using the equations of radiative transfer and equilibrium [Equations (6.9) and (6.10)] in finite difference form. The program as specifically listed below was used to generate Figure 6.2, and thus the pump rate was set at $R^P = (W_{lu}^P - W_{ul}^P)N_t/2 = 10^{20}\text{ m}^{-3}\text{ s}^{-1}$ to ensure that the maser models to be examined would not reach partial saturation.

$W^C = \frac{1}{\tau}$ is additionally computed, making use of the formulae in Appendix D.

```
COMMON M,N, JJ, EXAMP(200), EXPH(200), R(200), AN(200), GNUN(200)
REAL*8 PU, PL, BT, EU, EL, DP
DIMENSION AMP(5), GNUM(5), ALPHA(200), A(200), S(200), VAR(200,6)
```

```
C
C COMPUTE LTE INTENSITIES, INTEGRAL OVER FREQUENCY NORMALIZED
C TO UNITY
```

```
C
C CONSTANTS (MKS UNITS)
```

```
H=6.6252E-34
PI=3.14159
C=2.9979E8
GNU0=22.235080E9
BOLTC=1.38044E-23
N=161
H2M=1.67E-27*2.
H2OM=1.67E-27*18.
H2DEN=1.E16
```

```
C H2/H2O RATIO FROM EQUILIBRIUM
```

```
H2ODEN=H2DEN*3.3E-4
EU=H*1.34098E13
EL=EU-H*GNU0
```

```
C VAN DER WAAL B (LITERS/MOLE)
```

```
BH2O=.03049
BH2=.02661
```

```
C MOLECULAR DIAMETERS
```

```
DH2O=(BH2O*3./(PI*2.E3*6.02E23))**(1./3.)
DH2=(BH2*3./(PI*2.E3*6.02E23))**(1./3.)
D=(DH2O+DH2)/2.
```

```
C EINSTEIN A (PROB/SEC OF SPONTANEOUS TRANSITION)
```

```
EA=2.E-9
```

```
C CONVERT EINSTEIN A TO B
```

```
EB=EA*C*C/GNU0/GNU0/2./H/GNU0
```

```
C CONTINUUM SPECIFIC INTENSITY WATTS/M2/HZ/STER
```

```
SO=2.7E-17
```

```
C CONVERT EINSTEIN A TO B, ALSO GEOMETRY
```

```
CONST=C*C/GNU0/GNU0/8./PI
```

```
C LTE HYPERFINE INTENSITIES,  $\Delta F=-1$  TRANSITIONS
```

```
AMP(1)=.385
AMP(2)=.324
AMP(3)=.273
IJ=0
```

```
DO 10 IT=1,5
```

```
FF=0.
```

```
T=1500.
```

```
C BANDWIDTH IN KHZ
```

```
BW=666.67
GRADV=3.-IT
```

```
GAIN=1.
```

```
C REDUCED MASS=0.9 H2 MASS
  VAV=SQRT(8.*BOLTC*T/PI/(H2M*0.9))
C COLLISIONS PER H2O MOLECULE PER SECOND
  GNUC=PI*D*D*VAV*H2DEN
  BT=BOLTC*T
  PU=DSQRT(EU)*DEXP(-EU/BT)
  PROBU=PU*2./(BOLTC*T)/SQRT(BOLTC*T)/SQRT(PI)
C ARTIFICIAL PUMP RATE
  PUMP=1.E20
  PL=DSQRT(EL)*DEXP(-EL/BT)
  DP=PU-PL
  DPROB=DP*2./(BOLTC*T)/SQRT(BOLTC*T)/SQRT(PI)
C ARTIFICIAL INVERSION
  DELN=2.E7
  WRITE(6,99)T,DELN, GNUC,PUMP
99 FORMAT(1X,'T=',E12.4,'DELN=',E12.4,'GNUC=',E12.4,'PUMP=',E12.4)

  IF(DELN .LT. 0.) GO TO 10
  SIG=GNU0/C*SQRT(BOLTC*T/H2OM)
  SIG=.001*SIG/BW*(N-1)

C
C COMPUTE AMPLIFIED INTENSITIES, NORMALIZED TO UNITY
C
  DO 4 I=1,N
C CONTINUUM SPECTRUM
  S(I)=1.
4 CONTINUE
C 1AU=1.5E11M
  ZMAX=1.5E14
  NSTEP=10000
  DZ=ZMAX/NSTEP
C MASE
  GNUM(2)=80.
  DO 9 NN=1,NSTEP
C H2O 6-16 5-23 F=7-6,6-5,5-4 HYPERFINE FREQUENCY SPACINGS
C REFERENCED TO THE F=6-5 FREQUENCY
  GNUM(2)=GNUM(2)-GRADV/C*GNU0/BW*(N-1)/1000.
  GNUM(1)=GNUM(2)+33.07/BW*(N-1)
  GNUM(3)=GNUM(2)-43.3/BW*(N-1)
  ANORM=0.
C COMPUTE FREQUENCY DISTRIBUTION, INTEGRAL NORMALIZED TO UNITY
  DO 2 I=1,N
  A(I)=0.
  DO 1 II=1,3
  DGNU=GNUM(II)-I
  AMPM=AMP(II)*EXP(-DGNU*DGNU/2./SIG/SIG)
  A(I)=A(I)+AMPM
1 CONTINUE
  ANORM=ANORM+A(I)
2 CONTINUE
  AMAX=0.
```

```
DO 3 I=1,N
A(I)=A(I)/ANORM
C GAIN COEFFICIENT
ALPHA(I)=DELN*A(I)*EA*CONST/BW/1000.*(N-1)
IF(A(I) .GT. AMAX)AMAX=A(I)
3 CONTINUE
ANORM=0.
DO 5 I=1,N
AA=S(I)*ALPHA(I)*DZ
C SATURATION CONDITION
IF(DELN*EB*S(I)*S0*GAIN .GT. PUMP) AA=ALPHA(I)*PUMP*DZ/DELN/
$EB/S0/GAIN

S(I)=S(I)+AA
IF(S(I) .GT.ANORM) ANORM=S(I)
5 CONTINUE
GAIN=GAIN*ANORM
F=0.
DO 6 I=1,N
S(I)=S(I)/ANORM
6 CONTINUE
IF(NN .EQ. 1000) GO TO 7
GO TO 9
7 CONTINUE

IJ=IJ+1
WRITE (6,100) T,GAIN
100 FORMAT(1X,'T=',E12.3,'GAIN',E12.3)
DO 8 I=1,N
VAR(I,IJ)=S(I)
8 CONTINUE
GO TO 10
9 CONTINUE
10 CONTINUE

CALL PLOT(VAR,0.,1.,1.,VAR,0.,1.,N,1,IJ)
RETURN
END
```

APPENDIX C

ESTIMATION OF THE H₂O ROTATIONAL PARTITION FUNCTIONS $f_{6_{16}}$ AND $f_{5_{23}}$

We must estimate [$f_{5_{23}} - f_{6_{16}}$], the difference between the rotational partition functions of the lower (5_{23}) and upper (6_{16}) H₂O maser levels. Each maser level is denoted by the spectroscopic notation $J_{K_1 K_2}$; the partition functions f represent the fraction of H₂O molecules in the appropriate states. Making use of the Boltzmann formula (for nondegenerate or equally degenerate states) leads to

$$[f_{5_{23}} - f_{6_{16}}] \sim f_{5_{23}} [1 - e^{-hv_0/kT}] \quad (C.1)$$

where $hv_0 = E_{6_{16}} - E_{5_{23}} = 1.47 \times 10^{-23}$ J.

Since for $T \sim 1200^\circ\text{K}$,

$$\frac{hv_0}{kT} = 8.9 \times 10^{-4} \ll 1,$$

$$[f_{5_{23}} - f_{6_{16}}] \sim f_{5_{23}} \left[\frac{hv_0}{kT} \right]. \quad (C.2)$$

We obtain a crude estimate for $f_{5_{23}}$ as follows:

Under the condition that $\frac{hv_0}{kT} \ll 1$, the rotational partition function f_J for the lower rotational states of a rigid diatomic rotator may be approximated as (e.g., Sugden and Kenny, 1965)

$$f_J \sim \frac{(2J+1)hB}{kT}$$

where the "rotational constant" $B = h/8\pi^2 I$ with I being the molecular moment of inertia. Because each rotational state J is $(2J+1)$ fold degenerate* ($M_J = J, J-1, \dots -J$), and no additional levels are introduced for the case of an asymmetric top rotor such as H_2O (Sugden and Kenny, 1965), to this order of approximation,

$$f_{5_{23}} \sim 10 \frac{hB_{H_2O}}{kT} . \quad (C.3)$$

For B_{H_2O} we adopt $B_{H_2O} \approx \frac{1}{3}[A+B+C]$ as representative, where A , B , and C are the known rotational constants of the asymmetric H_2O molecule (e.g., Townes and Schawlow, 1955). Numerically, $B_{H_2O} \sim 5 \times 10^{11} \text{ Hz}$. Thus

$$\frac{hB_{H_2O}}{kT} \sim 2 \times 10^{-2} \text{ at } T = 1200^\circ\text{K}$$

and

$$[f_{5_{23}} - f_{6_{16}}] \sim \begin{cases} 10^{-5} & \text{at } T = 1500^\circ\text{K} \\ 10^{-4} & \text{at } T = 500^\circ\text{K} \end{cases} .$$

*Transitions between Zeeman split M_J levels have been observed in the presence of a high (10^4 gauss) magnetic field for H_2O (Burke and Strandberg, 1953) and for OH (Radford, 1961). The observed Zeeman splitting may be used to deduce the molecular magnetic moment (Burke and Strandberg, 1953).

APPENDIX D

ESTIMATION OF THE AVERAGE H₂O-H₂ INTERCOLLISION TIME, τ

We must evaluate $W^c = \frac{1}{\tau} \sim \pi \left[\frac{d_{H_2O} + d_{H_2}}{2} \right]^2 \bar{v} N_{H_2}$. The required molecular diameters may be determined from the CRC Handbook values for the Van der Waals b constants of molecular volume ($b_{H_2O} = 0.03049$ liters mole⁻¹; $b_{H_2} = 0.02661$ liters mole⁻¹) since $b = \frac{2}{3} \pi d^3 N_A$ where $N_A = 6.02 \times 10^{23}$ mole⁻¹ is Avogadro's number. To determine \bar{v} we will assume a thermal (Maxwell-Boltzmann) velocity distribution

$$\begin{aligned} f(v) &= f(v_x) f(v_y) f(v_z) \\ &= \left(\frac{m}{2kT} \right)^{3/2} \exp\left[-\frac{mv^2}{2kT}\right] \end{aligned}$$

Since

$$\int_0^{\infty} 4\pi v^2 f(v) v^{\ell} dv = \left(\frac{2kT}{m} \right)^{\ell/2} \frac{\Gamma\left(\frac{3}{2} + \frac{\ell}{2}\right)}{\Gamma\left(\frac{3}{2}\right)}$$

setting $\ell = 1$ yields

$$\bar{v} = \left(\frac{2kT}{m} \right)^{1/2} \frac{\Gamma(2)}{\Gamma\left(\frac{3}{2}\right)} = \left(\frac{2kT}{m} \right)^{1/2} \frac{(2-1)!}{\frac{1}{2} \pi^{1/2}} = \left(\frac{8kT}{\pi m} \right)^{1/2}$$

For a two-component gas m is replaced by the reduced mass

$$\frac{m_{H_2} m_{H_2O}}{m_{H_2} + m_{H_2O}} \approx 0.9 m_{H_2}$$

At $T = 1500^\circ\text{K}$, $\tau \sim \left[\frac{10^{15} \text{ m}^{-3}}{N_{\text{H}_2}} \right] \text{ s}^{-1}$.

Computational details are contained in Appendix B.

ACKNOWLEDGEMENTS

During the term of this investigation the author has been the recipient of much kindness, support, and assistance from friends, family, and associates.

This investigation was initiated and conducted under the supervision of the author's thesis advisor, Professor Irwin Shapiro, who also provided financial support during examination of the radio interferometer observations. Financial support during the later portions of this investigation was provided by the Department of Earth and Planetary Sciences, which throughout has been most supportive and has provided a most hospitable and stimulating environment.

Dr. James Moran (Smithsonian Astrophysical Observatory) was instrumental to the series of single antenna observations conducted at the Haystack Observatory, and his knowledge of radio astronomy and advice were often of great assistance.

Text editing and drafting assistance during preparation of the first draft were provided by Martha. The first draft typescript (and its emergence in May 1975) were due to the effort (and nagging) of Judith Ungermann. The author thanks Drs. B. F. Burke, Moran, and especially Shapiro for comments and suggestions based on the first draft which have led to significant improvements in this more final version of the text. The several typescripts of the final text and intermediate drafts were dispatched by Judith Ungermann. The

Hale Observatories, Yerkes Observatory, and Lick Observatory kindly granted permission to reproduce photographs shown in Chapter 3.

Biographical Note

Albert Colbert Reisz was born the first child of Albert and Alma Ruth Reisz in Baltimore, Maryland, on November 12, 1946. He received his elementary and secondary education in the public school system of Pennsauken, New Jersey. He entered M.I.T. as an undergraduate in 1965, and received an S.B. in Physics and an S.M. in Earth and Planetary Sciences in 1970. During the term of this investigation, he has been supported as a Research Assistant, Teaching Assistant, and by an Alfred P. Sloan Fellowship.

While at M.I.T. the author has been involved in research efforts which have resulted in the following publications:

"Radiation Temperature of Extraordinary Waves", M.I.T. Research Laboratory of Electronics, QPR 94, 1969. A. C. Reisz and B. L. Wright;

"Electromagnetic Probing of the Lunar Interior from One to Ten Kilohertz", S. M. Thesis, M.I.T. Department of Earth and Planetary Sciences, 1970;

"The Effects of Boundary Condition Asymmetries on the Interplanetary Magnetic Field-Moon Interaction", The Moon, Vol. 4, 1972. A. C. Reisz, D. L. Paul, and T. R. Madden;

"Lunar Electrical Conductivity", Nature, Vol. 238, 1972. A. C. Reisz, D. L. Paul, and T. R. Madden;

"Very Long Baseline Interferometric Observations of the H₂O Sources in W49 N, W3(OH), Orion A, and VY Canis Majoris", The Astrophysical Journal, Vol. 185, 1973. J. M. Moran, G. D. Papadopoulos, B. F. Burke, K. Y. Lo, P. R. Schwartz, D. L. Thacker, K. J. Johnston, S. H. Knowles, A. C. Reisz, and I. I. Shapiro;

"W3(OH): Accurate Relative Positions of Water Vapor Emission Features", The Astrophysical Journal, Vol. 186, 1973. A. C. Reisz, I. I. Shapiro, J. M. Moran, G. D. Papadopoulos, B. F. Burke, K. Y. Lo, and P. R. Schwartz.